University of Strathclyde

Department of Mechanical & Aerospace Engineering

Surface Engineering: Advanced Materials for Aggressive Environments

Husayn H. J. Izneen

This thesis is submitted in fulfilment of the requirements for the degree of Doctor Philosophy

2025

Declaration of Authenticity and Author's Rights

This thesis is the result of the author's original research. It has been composed by the author and has not been previously submitted for examination which has led to the award of a degree. The copyright of this thesis belongs to the author under the terms of the United Kingdom Copyright Acts as qualified by University of Strathclyde Regulation 3.50. Due acknowledgement must always be made of the use of any material contained in, or derived from, this thesis.

Singed: 

Date: 12/05/2025

Abstract

Enhancing the wear resistance of engineering components that operate under severe friction and abrasion is vital for extending service life and extending repair and maintenance intervals. This research presents a novel approach using 316L stainless steel tubular (316LSS-T) fillers filled with ceramic reinforcements; silicon carbide (SiC), and tungsten carbide with 10% cobalt (WC-10%Co) for the deposition of metal matrix composite (MMC) via tungsten inert gas (TIG) welding. The performance of these MMC coatings is benchmarked against conventional HF600 hard-facing electrodes on both low carbon steel (LCS-BM) and 316L stainless-steel (316LSS-BM) base metals.

Unlike the widely used preplaced powder method, which suffers from limited bonding strength, inconsistent reinforcement distribution and susceptibility to particle burn-off or dilution during welding, the tubular filler technique developed in this study offers precise control over reinforcement retention and distribution. This research advances the field by overcoming these drawbacks, offering a more robust, reliable, and scalable alternative to conventional MMC deposition methods explored in previous studies.

A deposition process was developed by refining tubular filler geometry (4 mm outer diameter, 3 mm inner diameter) and systematically adjusting the TIG welding parameters to ensure uniform reinforcement distribution, strong metallurgical bonding, and minimal ceramic dissolution. This tailored process enabled consistent microstructures suitable for evaluating wear behaviour. Dry sliding pin-on-disc wear tests assessed the tribological performance of the deposited MMC under varying loads (2–6 kg). Microstructural and surface analyses, including scanning electron microscopy (SEM) and energy-dispersive spectroscopy (EDS), revealed distinct wear mechanisms, material transfer patterns and protective tribo-layer formations.

Results show that WC-10%Co-reinforced MMC's achieved the highest wear resistance, especially on 316SS-BM, while SiC-reinforced deposition outperformed others on LCS-BM. Both significantly reduced material loss and outperformed HF600 coatings. The formation of oxide-rich tribo-layers on LCS-BM under high load conditions was key in suppressing abrasive wear and metal-to-metal contact. This work establishes the effectiveness and versatility of ceramic-filled tubular fillers in producing durable, wear-resistant deposition. The findings underline the industrial potential of this method for applications in aerospace, automotive, and heavy-duty manufacturing applications, offering a superior and innovative alternative to hard-facing electrodes and preplaced powder-based MMC techniques.

Acknowledgement

I would like to express my deepest gratitude to my first supervisor, Professor Alexander Galloway, for his unwavering support and exceptional mentorship. Your passion for research and enthusiasm for materials science have been a constant source of inspiration. Learning from your extensive knowledge and experience over the past three and a half years has been a privilege. Your insight has shaped every research stage, and working under your supervision has been a true honour.

I also thank the Advanced Materials Research Laboratory, Drs. Tiziana Marrocco, Maider Olasolo, and Fiona Sillars. Special thanks go to Mr. James Kelly and Mr. James Gillespie for their skilled assistance and generous knowledge-sharing in the laboratory. I would like to express appreciation to Mr. James Kelly for sharing his exceptional understanding of metallurgical and microstructural analysis. I am also grateful to my colleagues Andrew J. H. Garrick and Jonathan A. L. Draper for their friendship, encouragement, and shared experiences throughout our department. I extend my heartfelt thanks to the Department of Mechanical & Aerospace Engineering, which has provided a stimulating academic environment and a supportive community. I thank the academic staff for their guidance, the administrative staff for their continuous assistance, and the MAE workshop team namely Mr Drew Irvine, Mr Alistair Kerr, Miss Colette Corr, and Mr Derek Roberts for their outstanding technical support. I also thank my sponsor the Libyan Ministry of Higher Education and Scientific Research. Thanks to all my family and friends for their continuous support and encouragement.

Table of contents

List of figures

List of tables

List of symbols and acronyms

Symbol	Description
TIG	Tungsten Inert Gas
MMC	Metal Matrix composite
MCS-T	Medium Carbon Steel Tubular
LCS-T	Low Carbon Steel Tubular
304LSS-T	304L Stainless Steel Tubular
316LSS-T	316L Stainless Steel Tubular
SiC	Silicon Carbide
WC	Tungsten Carbide
LCS-BM	Low Cabon Steel Base Metal
316LSS-BM	316L Stainless Steel Base Metal
WCI	White Cast Iron
CI-P	Cast Iron Pin
SEM	Scanning Electron Microscope
EDS	Energy Dispersive Microscopy
XRD	X-Ray Diffreaction

Chapter 1 Thesis introduction and structure

1.1 Introduction

Due to its exceptional mechanical and physical properties, steel is a fundamental material in industrial applications, particularly in heavy industries. Its performance is primarily governed by its chemical composition, with carbon being the most influential element in determining the mechanical characteristics of steel alloys. Additionally, alloying elements such as chromium, molybdenum, and nickel are commonly incorporated to enhance strength, toughness, and corrosion resistance, tailoring the material to demanding operational environments. From a microstructural perspective, low-carbon steels predominantly consist of ferrite and pearlite phases, whereas stainless steels can exhibit austenitic, ferritic, or martensitic structures depending on composition and processing conditions. These microstructural variations significantly influence mechanical properties such as strength, ductility, toughness, weldability, and wear resistance, making steel a highly versatile engineering material [1.1,1.2]. However, concerns over the wear resistance of certain steel alloys can affect their in-service performance and, therefore, their lifespan when used in aggressive conditions [1.3-1.9]. The result being that premature degradation due to erosive or frictional wear often results in expensive replacement costs due to the component being withdrawn from service [1.9-1.13].

It is important to note that erosive and frictional wear are commonly observed in specific areas of a component. For example, in gear systems, material wear predominantly occurs at the gear teeth' rolling and sliding contact regions [1.14]. In rotating machinery components, such as rotors and shafts, material wear typically occurs in specific contact areas, including bearings, seal locations, blades, and casings [1.15]. This highlights that localised wear in specific areas can significantly reduce the lifespan of engineering components. Therefore, developing a process that enhances wear resistance through in-situ and highly localised hard surface

deposition applied either before or after wear occurs can substantially extend component longevity. Repairing or replacing these components is a significant concern for many industries, as replacements are often expensive and can lead to economic losses and material wastage. In many cases, entire components are substituted due to minor localised defects or cracks, making efficient wear-resistant solutions crucial for cost-effective maintenance and sustainability [1.16]. In-situ repair, which involves repairing the component where the initial wear occurred, is the optimal solution for reducing maintenance and replacement costs [1.17]. Additionally, localised in-situ surface modification or repair presents significant advantages over the complete replacement of worn components. The effectiveness of localised remelting and depositing of Metal Matrix Composite's (MMC's) lies in its ability to form a strong metallurgical bond between the deposited layer and the substrate upon solidification, ensuring enhanced adhesion and long-term performance [1.18-1.22].

Metal degradation due to wear, and the assessment of a component's expected operational lifespan are critical considerations in various engineering applications [1.23-1.26]. For instance, when metals are in contact with a moist environment, engineers encounter difficulties in estimating the expected durability of components [1.27-1.30]. Furthermore, due to that, the wear of materials is not just a material property but involves all materials, and conditions in the system [1.31, 1.32], Engineers, Researchers, and Designers could not fully predict the product life with confidence [1.33, 1.34]. Surface engineering techniques are employed to tailor the surface characteristics of components [1.35-1.40]. These techniques include, but are not limited to, thermal spraying, laser beam, electron beam, cold spraying, and arc welding. Each of these methods brings its advantages and challenges, allowing Engineers and researchers to tailor the surface properties of materials to meet specific industrial requirements.

Metal Matrix Composites consist of two primary components: a metal matrix and dispersed hard particles. They are currently the subject of ongoing research as a solution to mitigate

material degradation caused by wear and friction. MMC's have gained significant attention in recent decades due to their ability to provide superior mechanical and tribological properties compared to unreinforced alloys [1.41-1.47]. MMC's, as advanced materials, have demonstrated outstanding resistance to erosion and corrosion, possess superior sliding wear performance, and high hardness, along with electrical and thermal properties [1.43-1.50].

Developing a process for localised in-situ surface modification or repair is a significant and potentially transformative research challenge and remains a focus of investigation. The deposition of MMC's using the TIG welding method is a complex area of study, particularly due to the inherent difficulties in joining two dissimilar materials: metals and ceramics. The primary challenge of the dissolution of hard particles in the molten pool and their interaction with the substrate during solidification, can affect the overall coating integrity.

Coating failures such as delamination, high thermal residual stress, weak interfacial bonding, cracking, void formation, segregation, non-uniform deposition, and evaporation often arise due to the mismatch in physical properties between the coating and the substrate. Addressing these challenges is not only crucial for ensuring the reliability and effectiveness of MMC-based coatings, but also for enhancing their performance in wear-resistant applications, thereby making a significant impact in this research field [1.51]. However, most recent investigations that have utilised the TIG process for surface modification by processing hard ceramic particles were conducted using the preplaced powder method. These studies found that the preplaced powder method often resulted in the complete dissolution of the reinforcement particles, as well as the initiation of cracking, porosity, and insufficient metallurgical bonding between base metal and cladding layers [1.52-1.57].

In contrast, the present study focuses on developing an innovative, low-cost, in-situ localised surface modification or repair method that metallurgically bonds MMCs on worn steel alloys. This new ceramic powder feeding process, which aims to overcome the drawbacks associated

with existing TIG and powder embedding technologies, is significant because it allows for the welding of the area that has undergone erosion damage using innovative ceramic materials-infused electrodes, thus filling the eroded area with the resulting composite material. The study aims to experimentally study the feasibility of applying the resultant composite material in the areas prone to wear erosion on steel alloy and engineering parts such as rotors, shafts, spindles, gears etc. So, the eroded part is expected to be repaired and reused, and further erosion will be minimised in that area due to increased hardness, wear resistance and other mechanical and chemical properties of the localised composite material. This research investigated the enhancement of worn low-carbon steel and austenitic stainless-steel components, which are common materials employed in various applications. However, the practical application of this knowledge may also be applied to other metal alloys such as Ti, Al, Ni, etc.

The proposed approach employs tubular fillers containing hard ceramic particles and is designed to deposit MMC's and significantly enhance wear resistance. The selection of the tubular filler's material is a critical factor, requiring careful consideration of matching, overmatching, and undermatching strategies concerning the mechanical properties and chemical composition of both the substrate and the filler material. When evaluating this compatibility, the concepts of matching, overmatching, and undermatching refer to the relative alloying composition and resulting metallurgical behaviour. For instance, a matching filler has a chemical composition that is approximately equivalent to that of the base metal. This ensures similar metallurgical properties, thermal expansion, and mechanical behaviour, promoting sound metallurgical bonding and reducing the risk of dilution-related inhomogeneities. Key physical properties influencing coating performance include melting point, wettability, elastic modulus, and the coefficient of thermal expansion.

Accordingly, low-carbon steel and stainless-steel tubular electrodes have been selected for investigation. Therefore, the objectives of this study are to:

- Significantly contribute to the field by developing a robust process for the hard ceramic powder feeding system on the substrate surface.
- Conduct a comprehensive examination of the deposited layers' microstructure, microhardness, and chemical composition, ensuring a thorough understanding of their characteristics.
- Characterise the deposited layers' tribological properties and compare it with available commercial hard facing consumables electrodes.

This thesis contributes to and expands existing knowledge by developing an innovative ceramic powder feeding process. Furthermore, this thesis will conduct a comprehensive microstructural characterisation of the deposited material, using optical microscopy and scanning electron microscopy. The chemical composition distribution and microhardness properties will be analysed through X-ray diffraction, energy-dispersive spectroscopy, and micro-indentation hardness testing. The composite material's sliding wear resistance will be evaluated under dry conditions using a pin-on-disc tribological test. The test samples will be examined under varying loading conditions, and the resulting wear scars will be analysed to characterise the dominant wear mechanisms affecting each specimen's surface. These investigations aim to provide a deeper understanding of the microstructural evolution, wear behaviour, and mechanical performance of the developed coatings. The insights gained from this research have the potential to significantly impact the field of wear-resistant materials and surface engineering.

1.2 Thesis Structure

This thesis is structured to systematically present the research undertaken in developing powder feeding process for TIG welding repair and resurfacing. The practical application of this research in the field of resurfacing is a key focus, ensuring its relevance and potential impact.

Chapter 2 offers a comprehensive literature review, commencing with a historical perspective on metal wear mechanisms and material loss prediction. It considers the microstructural characteristics of steel and explores various state-of-the-art surface engineering techniques used in developing ceramic-reinforced steel. The review critically evaluates the advantages and limitations of these techniques, establishing the current state of research in surface engineering, with a particular focus on the ceramic powder feeding process. Furthermore, this chapter discusses the fundamentals of TIG welding, including its main components and the incorporation of ceramic particles into steel alloys. A critical review of previous studies on the effects of TIG welding parameters is also presented, ensuring a thorough understanding of the research's foundation.

Chapter 3 outlines the research methodology, detailing the materials, experimental methods, and equipment. This chapter explains the experimental procedures in meticulous detail, ensuring reproducibility and clarity in understanding the research approach and instilling confidence in the research's reliability.

Chapter 4 presents the optimisation and validation of deposition process parameters, including refining tubular filler dimensions and ceramic powder content. This chapter is divided into sub-sections, each addressing using different base materials, such as low-carbon steel and stainless steel, and different carbide reinforcements, including silicon carbide SiC and tungsten carbide WC. The experimental results are discussed in detail, focusing on embedding reinforcement ceramic particles within the steel matrix. Based on these findings, the optimal processing parameters, powder content, and tubular filler dimensions were established.

Chapter 5 applies the optimised conditions derived from Chapter 4 to assess the wear resistance of deposited composite materials on worn LCS and 316L stainless-steel discs. This chapter investigates using tubular fillers containing ceramic particles for repairing eroded

surfaces, where grooves simulating wear damage were filled with weld deposits. Several material combinations were evaluated, and a comprehensive analysis of wear resistance was conducted. The results of pin-on-disc tribometer tests are presented, followed by an in-depth discussion of material loss, wear scars, and the surface morphology of worn discs tested against cast iron pin.

Chapter 6 concludes the thesis by summarising the key findings and contributions of the research. Additionally, this chapter provides recommendations for future work, highlighting potential advancements in ceramic-reinforced TIG welding and its applications in wear-resistant coatings.

1.3 References

[1.1] Pradeep, D.G., C.V. Venkatesh, and H.S. Nithin, Review on Tribological and Mechanical Behavior in HVOF Thermal-sprayed Composite Coatings. Journal of Bio- and Tribo-Corrosion, 2022. 8(1).

[1.2] Rajak, D.K., et al., Critical Overview of Coatings Technology for Metal Matrix Composites. Journal of Bio- and Tribo-Corrosion, 2019. 6(1).

[1.3] Sharma, D., et al., Surface modification of microalloyed steel by silicon carbide reinforcement using tungsten inert gas arcing. Materials Research Express, 2018. 6(3).

[1.4] Shrivas, S.P., et al., Investigation of TIG welding parameters to improve strength. Materials Today: Proceedings, 2020. 26: p. 1897-1902.

[1.5] Vora, J.J., K. Abhishek, and S. Srinivasan, Attaining optimized A-TIG welding parameters for carbon steels by advanced parameter-less optimization techniques: with experimental validation. Journal of the Brazilian Society of Mechanical Sciences and Engineering, 2019. 41(6).

[1.6] Wenbin, D., et al., Microstructure and mechanical properties of GTA surface modified composite layer on magnesium alloy AZ31 with SiCP. Journal of Alloys and Compounds, 2007. 429(1-2): p. 233-241.

[1.7] Zhai, W., et al., Recent Progress on Wear-Resistant Materials: Designs, Properties, and Applications. Adv Sci (Weinh), 2021. 8(11): p. e2003739.

[1.8] Zhang, D., et al., Thermodynamic analysis of the interface reaction and thermal stress of WCp/Fe composites. Ceramics International, 2020. 46(16): p. 26210-26215.

[1.9] Zhang, F., et al., Improving the impact wear properties of medium carbon steel by adjusting microstructure under alternating quenching in water and air. Wear, 2023. 512-513.

[1.10] Sun, S., et al., Preparing WC-Ni coatings with laser cladding technology: A review. Materials Today Communications, 2023. 37.

[1.11] Alam, M.S., Recent Trends in Surface Cladding on AISI 1045 Steel Substrate: A Review, in Functional Materials and Applied Physics. 2022. p. 94-101.

[1.12] Alam, M.S. and A.K. Das, Research Progress in Gas Tungsten Arc Cladding on Steel: A Critical Review, in Recent Advances in Manufacturing Processes and Systems. 2022. p. 859-867.

[1.13] Cao, X., et al., Surface microstructure and property modifications in AISI 304 stainless steel induced by pseudospark pulsed electron beam treatments. Vacuum, 2021. 184: p. 109914.

[1.14] Britton, R., et al., Effect of surface finish on gear tooth friction. J. Trib., 2000. 122(1): p. 354-360.

[1.15] Prabith, K. and I.R.P. Krishna, The numerical modeling of rotor–stator rubbing in rotating machinery: a comprehensive review. Nonlinear Dynamics, 2020. 101(2): p. 1317-1363.

[1.16] Raj, D., S.R. Maity, and B. Das, State-of-the-art review on laser cladding process as an in-situ repair technique. Proceedings of the Institution of Mechanical Engineers, Part E: Journal of Process Mechanical Engineering, 2021. 236(3): p. 1194-1215.

[1.17] Lewis, S.R., R. Lewis, and D.I. Fletcher, Assessment of laser cladding as an option for repairing/enhancing rails. Wear, 2015. 330-331: p. 581-591.

[1.18] Riveiro, A., et al., Laser cladding of aluminium on AISI 304 stainless steel with high-power diode lasers. Surface and Coatings Technology, 2014. 253: p. 214-220.

[1.19] Lazurenko, D.V., et al., Formation of wear-resistant copper-bearing layers on the surfaces of steel substrates by non-vacuum electron beam acladding using powder mixtures. Surface and Coatings Technology, 2020. 395: p. 125927.

[1.20] Kumar, A. and A.K. Das, Correction to: Development of Al-Ni-TiC Composite Coating on Commercially Pure Al Using Tungsten Inert Gas Welding Route and its Wear Behavior. Journal of Materials Engineering and Performance, 2022. 31(7): p. 5332-5332.

[1.21] Bartkowski, D. and A. Bartkowska, Wear resistance in the soil of Stellite-6/WC coatings produced using laser cladding method. International Journal of Refractory Metals and Hard Materials, 2017. 64: p. 20-26.

[1.22] Bartkowski, D., et al., Microstructure, microhardness and corrosion resistance of Stellite-6 coatings reinforced with WC particles using laser cladding. Optics & Laser Technology, 2015. 68: p. 191-201.

[1.23] Lu, B., D. Xia, and J. Luo. Mechanism of Corrosion-Enhanced Erosion of Steels in Oil and Gas Production. in TMS 2014: 143 rd Annual Meeting & Exhibition: Annual Meeting Supplemental Proceedings. 2016. Springer.

[1.24] Lu, B., J. Lu, and J. Luo, Erosion–corrosion of carbon steel in simulated tailing slurries. Corrosion Science, 2011. 53(3): p. 1000-1008.

[1.25] Chandel, S., S. Singh, and V. Seshadri, Experimental study of erosion wear in a centrifugal slurry pump using coriolis wear test rig. Particulate Science and Technology, 2012. 30(2): p. 179-195.

[1.26] El-Emam, M.A., et al., Computational methods of erosion wear in centrifugal pump: A state-of-the-art review. Archives of Computational Methods in Engineering, 2022. 29(6): p. 3789-3814.

[1.27] Tarodiya, R. and B.K. Gandhi, Hydraulic performance and erosive wear of centrifugal slurry pumps - A review. Powder Technology, 2017. 305: p. 27-38.

[1.28] Roco, M. and G. Addie, Erosion wear in slurry pumps and pipes. Powder Technology, 1987. 50(1): p. 35-46.

[1.29] Okonkwo, P.C. and A.M. Mohamed, Erosion-corrosion in oil and gas industry: a review. Int. J. Metall. Mater. Sci. Eng, 2014. 4(3): p. 7-28.

[1.30] Luo, X.W., et al., Abrasive Erosion Comparison for a Ceramics and a High Chrome Cast Iron Applied in a Slurry Pump. Key Engineering Materials, 2008. 368: p. 894-897.

[1.31] Eyre, T.S., Wear Mechanisms. Powder Metallurgy, 2013. 24(2): p. 57-63.

[1.32] You, W., et al., Sliding wear behavior of pearlitic structures in eutectoid steel. Wear, 1991. 143(1): p. 57-69.

[1.33] Meng, H. and K. Ludema, Wear models and predictive equations: their form and content. Wear, 1995. 181: p. 443-457.

[1.34] Eyre, T., The mechanisms of wear. Tribology international, 1978. 11(2): p. 91-96.

[1.35] Mellor, B.G., Surface coatings for protection against wear. 2006: Woodhead Publishing.

[1.36] Fauchais, P.L., J.V. Heberlein, and M.I. Boulos, Thermal spray fundamentals: from powder to part. 2014: Springer Science & Business Media.

[1.37] Pileggi, R., et al., Tribo-corrosion behaviour of chromium carbide-based coatings deposited by HVOF. Surface and Coatings Technology, 2015. 268: p. 247-251.

[1.38] Abdi, S. and S. Lebaili, Alternative to chromium, a hard alloy powder NiCrBCSi (Fe) coatings thermally sprayed on 60CrMn4 steel. Phase and comportements. Physics Procedia, 2009. 2(3): p. 1005-1014.

[1.39] Bolelli, G., et al., Corrosion resistance of HVOF-sprayed coatings for hard chrome replacement. Corrosion science, 2006. 48(11): p. 3375-3397.

[1.40] Winter, K.-M., J. Kalucki, and D. Koshel, Process technologies for thermochemical surface engineering, in Thermochemical surface engineering of steels. 2015, Elsevier. p. 141-206.

[1.41] Miracle, D., Metal matrix composites–from science to technological significance. Composites science and technology, 2005. 65(15-16): p. 2526-2540.

[1.42] Clyne, T.W. and P.J. Withers, An introduction to metal matrix composites. 1993: Cambridge university press.

[1.43] Miracle, D., Metallic composites in space: a status report. JOM, 2001. 53(4): p. 12.

[1.44] Chawla, N. and K. Chawla, Metal-matrix composites in ground transportation. JoM, 2006. 58: p. 67-70.

[1.45] Beidler, C., W. Hauth III, and A. Goel, Development of a B4C/Al cermet for use as an improved structural neutron absorber. Journal of testing and evaluation, 1992. 20(1): p. 67-70.

[1.46] Rittner, M.N., Expanding world markets for MMCs. JOM, 2000. 52(11): p. 43.

[1.47] Neville, A., et al., Assessing metal matrix composites for corrosion and erosion-corrosion applications in the oil sands industry. Corrosion, 2006. 62(8): p. 657-675.

[1.48] Liu, L. and J. Xu, A study of the erosion–corrosion behavior of nano-Cr2O3 particles reinforced Ni-based composite alloying layer in aqueous slurry environment. Vacuum, 2011. 85(6): p. 687-700.

[1.49] Wentzel, E.J. and C. Allen, Erosion-corrosion resistance of tungsten carbide hard metals with different binder compositions. Wear, 1995. 181: p. 63-69.

[1.50] Pagounis, E. and V. Lindroos, Processing and properties of particulate reinforced steel matrix composites. Materials Science and Engineering: A, 1998. 246(1-2): p. 221-234.

[1.51] Kumar Das, A., Recent developments in TIG torch assisted coating on austenitic stainless steel: A critical review. Materials Today: Proceedings, 2022. 57: p. 1846-1851.

[1.52] Baker, T.N., et al., Role of preplaced silicon on a TIG processed SiC incorporated microalloyed steel. Materials Science and Technology, 2020. 36(12): p. 1349-1363.

[1.53] Munoz-Escalona, P., S. Mridha, and T. Baker, Advances in Surface Engineering Using TIG Processing to Incorporate Ceramic Particulates into Low Alloy and Microalloyed Steels – A Review. Advances in Science and Technology Research Journal, 2021. 15(3): p. 88-98.

[1.54] Muñoz-Escalona, P., S. Mridha, and T.N. Baker, Effect of shielding gas on the properties and microstructure of melted steel surface using a TIG torch. Advances in Materials and Processing Technologies, 2016. 1(3-4): p. 435-443.

[1.55] Muñoz-Escalona, P., S. Mridha, and T.N. Baker, Effect of silicon carbide particle size on microstructure and properties of a coating layer on steel produced by TIG technique. Advances in Materials and Processing Technologies, 2016. 2(4): p. 451-460.

[1.56] Muñoz-Escalona, P., et al., Silicon carbide particulates incorporated into microalloyed steel surface using TIG: microstructure and properties. Materials Science and Technology, 2019. 36(1): p. 17-32.

[1.57] Muñoz-Escalona, P., et al., Comparison of empirical and predicted substrate temperature during surface melting of microalloyed steel using TIG technique and considering three shielding gases. Applied Surface Science, 2019. 477: p. 179-183.

Chapter 2 Literature review

2.1 Introduction

This chapter reviews the subject of wear phenomena in steel components and the frictional mechanisms responsible for surface degradation. To address these limitations, it explores the development of advanced surface materials, particularly metal matrix composites (MMCs), which are formed by embedding hard ceramic particles into a metallic matrix to enhance wear resistance. Various surface engineering techniques are reviewed, emphasising methods that enable the incorporation of ceramic particles into the target surface while minimising thermal or structural impact on the bulk substrate. The chapter also examines ceramic powder feeding strategies. It highlights the application of tungsten inert gas (TIG) welding for embedding reinforcements such as silicon carbide (SiC) and tungsten carbide-cobalt (WC-10%Co) to improve tribological performance.

2.2 Fundamentals of friction, wear, and their influence on surface degradation

Wear is critical in degrading metallic components in engineering systems, contributing to safety risks, economic loss, and environmental burden. Unlike strength or hardness, wear is not an intrinsic material property, instead, it arises from complex interactions between contacting surfaces, environmental conditions, and mechanical loading parameters [2.1-2.3]. This complexity makes it difficult to accurately predict service life under varying or extreme operational scenarios [2.4,2.5].

Surface engineering techniques have long been employed to mitigate wear related failures by enhancing the surface properties of metals through alloying, coatings, or heat treatment [2.6-2.11]. However, many conventional surface modification methods exhibit limitations such as limited wear life, inadequate bonding of coatings, or high process costs. In this context, the present study introduces an alternative strategy of embedding hard ceramic particles into a

steel matrix to repair and reinforce wear prone areas locally. This approach relies on a deeper understanding of friction and wear mechanisms, essential to support the rationale for using MMC ‘s in such applications.

Tribological contact typically occurs at microscopic asperities protrusions on otherwise smooth surfaces, which are the real contact points during sliding or rubbing [2.12, 2.13]. These regions are highly susceptible to stress concentration and material failure. Although surfaces may appear smooth macroscopically, they remain rough at the nanoscale [2.14]. The morphology and properties of asperities (such as size, shape, physical, and chemical) significantly influence wear mechanisms and rates. Bishop et al. [2.13] demonstrated that stress distribution under contact loading correlates closely with yield strength and that contact pressure can be approximated by modelling asperities as spherical or conical features.

Colaco and Serro [2.15] presented a comprehensive review of wear modelling from the atomic to macro scale, revealing how classical continuum theories often fail to explain material behaviour at the nanoscale. Similarly, Vakis et al. [2.3] emphasised the fragmented nature of tribological science, despite centuries of development from Holm’s pioneering theories [2.16] to the widely adopted Archard’s wear law [2.14, 2.17]. They noted that although empirical models exist in abundance, a unified, predictive understanding of wear mechanisms across length scales remains limited.

Beyond modelling limitations, experimental studies have consistently revealed the complexity of wear transitions. Hirst and Lancaster [2.18] observed that the degradation of protective oxide films plays a crucial role in shifting wear behaviour from mild to severe, often triggered by critical loads or temperatures. Lim et al. [2.19] added that velocity induced phase transformations, such as forming martensitic structures under frictional heating influence wear transitions.

Hardness has long been used as a primary indicator of wear resistance. However, studies by Mutton and Watson [2.20] revealed that hardness alone is insufficient for predicting wear behaviour. They found that heat treated steels can exhibit poorer wear resistance than softer pure metals under similar conditions. This discrepancy was attributed to the interplay between hardness, plastic deformation, and fracture behaviour at the wear interface. Moore [2.21] reported a positive correlation between pearlite content and wear resistance in steels, while Nakajima and Mizutani [2.22] identified the role of strain hardening and dislocation pile up around cementite plates in governing subsurface deformation during sliding.

Further microstructural investigations by Grabar and Skorinin [2.23] demonstrated that dislocation density increases significantly near worn surfaces and that grain elongation in sliding direction can contribute to localised failure. Grain boundaries-oriented perpendicular to the sliding direction were shown to impede dislocation motion and delay damage propagation. These findings reinforce the importance of tailoring microstructure not just hardness for enhanced wear resistance.

In addition to sliding and abrasive wear, oxidation plays a central role in many industrial wear scenarios. Fink [2.24] first observed the influence of tribo oxidation on wear in the 1930s, and Archard and Hirst [2.18] later established a strong connection between oxide layer formation and wear regime transitions. Wang et al. [2.25] conducted dry sliding experiments on several steels and found that wear rates increased with applied load, reaching critical thresholds that triggered transitions from mild to severe wear. The interplay between mechanical loading and oxide film stability significantly affected surface integrity and performance.

Despite significant progress in tribological modelling and surface engineering techniques, conventional metallic materials often fail to provide long term wear resistance under combined mechanical and thermal loading. Many commercial surface treatments suffer from limitations such as poor particle retention, interfacial cracking, excessive dilution of reinforcements, and

complex processing requirements alloys [2.14, 2.18, 2.22, 2.24-2.33]. These challenges underscore the demand for advanced materials capable of sustaining performance under high loads and extended sliding durations.

MMC's, particularly those incorporating hard ceramic particles such as SiC and WC-10%Co, have emerged as a promising solution. Their tailored combination of high hardness, toughness, and thermal stability allows them to outperform monolithic metals in tribological environments [2.34-2.37]. Furthermore, when strategically embedded into a ductile metallic matrix, these reinforcements improve resistance to abrasive and oxidative wear without compromising the toughness of the substrate. The next sections examine the development of MMC systems, the role of ceramic reinforcements, and the techniques employed to integrate these materials into steel substrates using surface engineering approaches.

2.3 Metal matrix composites

MMC's reinforced with hard ceramic particles such as SiC and WC-10%Co represents a major advancement in materials engineering for wear-intensive applications [2.37-2.43]. The superior performance of MMC's arises from the synergistic interaction between a ductile metallic matrix and embedded hard phases that enhance abrasion resistance, load-bearing capacity, and thermal stability. Studies have shown that SiC offers high hardness and oxidation resistance [2.44-2.48], while WC-10%Co provides additional toughness due to the Cobalt [2.49-2.55]. When effectively embedded into a metallic matrix, these ceramics significantly improve surface durability under sliding, impact, or erosive conditions [2.56-2.61]. Berns [2.35] provided extensive experimental validation showing that MMCs reinforced with WC/W_2C and CrB_2 can outperform white cast irons (WCI) by 30–40 times in abrasive wear resistance while demonstrating superior fracture toughness. However, the critical challenge in MMC fabrication lies in maintaining the integrity of the ceramic reinforcements during processing. High-temperature conditions may lead to complete dissolution and undesirable

interfacial reactions, which reduce composite effectiveness. Achieving optimal performance requires careful control over the matrix's reinforcement type, volume fraction, morphology, and distribution. Recent studies [2.36, 2.37, 2.39, 2.56, 2.62-2.64] underline the importance of particle stability, metallurgical bonding, and the avoidance of extensive dilution during composite deposition. These factors are especially relevant in surface engineering applications, where wear resistance must be enhanced without compromising the underlying substrate's mechanical properties.

2.4 Surfacing Methods and Powder Feeding

Advanced surface engineering techniques such as coating and cladding have been extensively employed to repair and enhance worn metallic components operating under aggressive service conditions. These methods enable the formation of surface layers with tailored mechanical, chemical, and tribological properties, significantly extending the service life of engineering parts. Cladding processes are particularly valuable, as they create a metallurgically bonded layer between the deposit and the substrate, offering superior mechanical integrity compared to traditional coatings [2.57, 2.58, 2.65-2.68]. Surface cladding is typically achieved by melting the surface of the substrate using a high-energy heat source while simultaneously depositing a secondary material. Commonly used heat sources include laser beams, electron beams, and electric arcs. Each technique's energy input characteristics, penetration depth, control precision, and compatibility with different reinforcement materials differ. Historically, widely adopted methods include thermal spraying [2.69-2.71], laser beam processing [2.58-2.60, 2.66, 2.67, 2.72-2.74], and TIG welding [2.75-2.82]. These technologies have significantly improved surface properties such as hardness, wear, and corrosion resistance.

2.4.1 Thermal Spray Technique

Thermal spraying, introduced in the late 19th century by Max Ulrich Schoop, involves projecting molten or semi-molten materials onto a prepared surface to form a coating [2.83].

Feedstock materials can be delivered as powders or wires and are melted by flame, arc, or plasma sources. Among thermal spray types, flame spraying, subdivided into powder and wire flame spray, is widely used due to its simplicity and versatility. Despite its broad industrial adoption, thermal spraying has notable limitations:

- Coatings may contain high oxide content and porosity [2.84].
- Weak interfacial bonding limits wear resistance [2.69].
- Residual stresses from thermal gradients can cause cracking and delamination [2.85].
- Achievable coating thickness is limited [2.86].
- The process poses health and safety risks due to dust and fumes.
- In addition, thermal spraying is often more suitable for corrosion protection than for heavy-duty wear applications requiring strong metallurgical bonding and thick surface layers.

2.4.2 Laser Beam Processing

Laser beam techniques are widely used in surface engineering due to their high energy density and precise thermal control. Lasers allow reinforcement materials to be introduced through several feeding configurations, including coaxial powder feeding [2.87], re-placed powder [2.88], off-axis powder feeding [89], and wire feeding [2.90]. The pre-placed powder is often used, though it can suffer from issues such as powder displacement by shielding gas and the evaporation of organic binders used for adhesion [2.66, 2.91]. Laser cladding is effective in producing high-performance wear-resistant surfaces, but the high cost of equipment, operational constraints, and limited scalability to large components restrict its use outside controlled environments.

2.4.3 TIG Welding

Tungsten Inert Gas (TIG) welding, also known as Gas Tungsten Arc Welding (GTAW), utilises a non-consumable tungsten electrode to generate a stable, high-temperature arc for localised

surface melting. TIG welding is widely used today due to its clean welds, arc stability, precise heat input, and strong metallurgical bonding across various metals, including stainless steel, carbon steel, and high-strength alloys [2.92-2.96].

TIG welding has been increasingly adapted for surface modification and cladding applications in recent decades. Its low dilution, narrow heat-affected zone, and ability to process dissimilar materials [2.97-2.102], make it attractive for reinforcing worn or damage-prone surfaces. As an economical alternative to laser-based methods, TIG offers promising capabilities in embedding ceramic reinforcements such as SiC and WC into steel matrices. Initial studies, such as those by Mirdha [2.93, 2.103], demonstrated the feasibility of TIG-based surface modification using ceramic powders. Subsequently, research has confirmed its potential for enhancing the surface hardness and wear resistance [2.104-2.111].

The most common approach for delivering ceramic particles in TIG surface engineering is the pre-placed powder method, [2.94, 2.99, 2.112, 2.113] where a layer of ceramic powder is adhered to the substrate using a binder (e.g., PVA) and then fused into the surface using TIG heat. While effective, this method poses several practical challenges: the need for furnace drying, the risk of powder displacement due to gas flow, and limited flexibility in complex geometries or on-site repairs. These limitations have stimulated interest in more advanced powder delivery methods, with ongoing research focused on optimising reinforcement incorporation and ensuring reliable metallurgical bonding during TIG processing.

2.5 Influences of TIG processing parameters

A set of key process parameters strongly influences the performance of a TIG-welded MMC deposit. These include welding current, voltage, torch travel speed, standoff distance, shielding gas composition and flow rate, and overall heat input. These factors affect the energy delivered to the weld zone, influencing solidification dynamics, microstructural evolution, bonding quality, and mechanical properties [2.68, 2.114-2.118]. Therefore, understanding and

optimising these parameters is essential for achieving high-quality, defect-free MMC surface layers.

2.5.1 Current and voltage

Welding current and voltage are among the most critical parameters in TIG welding, directly affecting the arc energy and heat input. Singh et al. [2.119] investigated the influence of welding current and travel speed on the deposition of WC powder on AISI 304 stainless steel. Their study revealed that increased heat input, driven by higher current, leads to longer solidification times, affecting microstructure and mechanical properties. The authors concluded that it is possible to tailor the microstructure for enhanced surface properties by carefully adjusting current and travel speed. TIG welding offers a cost-effective alternative to laser-based techniques. Foot-pedal modulation of current and voltage enables precise arc energy control. This feature is particularly advantageous for MMC deposition, allowing for controlled melting of the matrix while minimising the thermal degradation of embedded ceramic particles [2.95, 2.96, 2.120-2.123].

2.5.2 Welding rod angle

In TIG welding, the angle at which the filler rod is introduced into the weld pool plays a critical role in determining the quality, shape, and consistency of the deposited materials. The filler rod angle typically defined as the angle between the rod and the workpiece surface directly influences melting efficiency [2.124], bead profile, reinforcement distribution and overall weld integrity. Moreover, proper rod angle facilities consistent metal transfer into the weld pool.

2.5.3 Standoff distance and speed of travel

Standoff distance, the gap between the tungsten electrode and the substrate, significantly impacts arc shape, energy concentration, and shielding effectiveness. Singh et al. [2.124] found that increasing the standoff distance improved the hardness and wear resistance of the

deposited layer. Singh [2.125], involving SiC/C alloying on AISI 4140 steel, reported that low heat input, reduced powder content, and high travel speed enhanced tribological properties by minimising thermal stress. Similarly, Jayashree et al. [2.126] investigated WC-10Co-4Cr deposition and identified welding current as the most influential factor on surface hardness, followed by travel speed and standoff distance, while shielding gas flow rate had the least impact.

2.5.4 Heat input

Heat input (E), typically expressed in J/mm, governs the extent of substrate melting and reinforcement incorporation. Reported heat input ranges for TIG welding in MMC applications vary from 210 J/mm to 3479 J/mm [2.105]. While sufficient heat is required to form a stable fusion zone, excessive input can lead to undesirable phenomena such as ceramic particle dissolution. Most studies agree that TIG welding generally should not fully melt ceramic particles, especially those with high thermal stability such as SiC or WC [2.104-2.106]. Cracks and porosity are commonly reported when parameters are not optimised [2.109, 2.127, 2.128]. Nonetheless, ceramic reinforcements dramatically enhance surface hardness and wear resistance when properly incorporated.

2.5.5 Shielding gas

Shielding gases protect the molten weld pool from atmospheric contamination and could influence thermal conductivity and arc temperature. Patel et al. [2.110] compared argon and helium shielding for SiC deposition on mild steel and found that helium-containing gas mixtures increased arc temperature significantly. Munoz et al. [2.108] reported that the shielding gas argon, helium, or nitrogen had a measurable impact on microstructure and hardness.

2.6 SiC-Reinforced steel composites: challenges and insights

SiC is among the most widely explored ceramic reinforcements for steel-based MMC owing to its high hardness, chemical stability, thermal conductivity, and superior wear resistance [2.48, 2.106, 2.129, 2.130]. Its integration into steel substrates aims to produce surface layers with enhanced hardness and tribological performance under demanding service conditions. However, practical implementation faces major metallurgical challenges. SiC is highly reactive with molten steel, leading to partial or complete decomposition, formation of brittle intermetallic phases (e.g., Fe_3Si, Fe_2Si), graphite precipitation, and silicon diffusion into the steel matrix. These transformations compromise the mechanical integrity and durability of the reinforced layer.

Numerous studies [2.28, 2.103, 2.126, 2.129, 2.131-2.135] have investigated SiC incorporation through surface modification techniques such as laser and arc melting. Despite repeated documentation of increased surface hardness, a significant limitation persists, many studies do not evaluate the wear resistance of the modified layers, even when mechanical or microstructural improvements appear promising. This exclusion weakens the ability to assess long-term performance in wear-critical environments, where hardness alone is insufficient to predict durability or resistance to degradation [2.134, 2.136-2.139].

For example, Baker et al. [2.105] used TIG welding with SiC and Si preplaced powders on micro-alloyed steel. While the Si+SiC configuration reached up to 870 HV, extensive SiC dissolution and the formation of brittle Fe_3Si phases caused interfacial microcracking. The study acknowledged that the poor metallurgical bond and porosity from binder decomposition weakened the layer's structural integrity, and wear resistance was not evaluated. Similarly, Buytoz et al. [2.140] observed that higher SiC content and controlled heat input could yield hardness values exceeding 1100 HV, yet no wear data were reported. Graphitic carbon formation and weak adhesion were also concerns that could adversely affect wear behaviour.

In laser-based surface alloying, Majumdar et al. [2.141] noted improved hardness (~600 HV) and fine microstructural refinement in SiC-reinforced mild steel but also reported carbide decomposition and silicide formation near the melt interface. Although wear testing demonstrated reduced groove depth and plastic deformation, brittle intermetallic like Fe_2Si contributed to micro-fracture and debris formation, raising concerns about long-term durability. Other studies, including those by Terry et al. [2.44], Escalona et al. [2.106], and Reddy et al. [2.116], confirmed that SiC decomposes rapidly in molten iron, forming iron silicide's and graphite, often leading to high local hardness but with no residual SiC detected. Most of these studies omitted wear testing or provided only indirect evidence of tribological improvement.

The effects of TIG processing parameters, shielding gas type, and preplacement configuration have been further examined in recent work. Maleque et al. [2.142] and Patel et al. [2.110] showed that moderate energy input promotes carbide and silicide formation while improving hardness, but excessive heat leads to porosity and microcracking. While surface microhardness increased substantially, wear performance remained speculative. Even in studies that reported wear testing, such as Lailatul et al. [2.143], results indicated that improvements were closely tied to optimal energy input, which is a critical factor in achieving the desired wear performance. Beyond this, excessive melting caused SiC decomposition and diminished benefits. Others, like Sharma et al. [2.144], confirmed hardness gains through TIG arcing but offered no wear evaluation, limiting the conclusions regarding durability.

The literature confirms that SiC incorporation into steel can enhance surface hardness through phase transformation, carbide formation, and matrix refinement. However, its instability under fusion-based deposition and the frequent absence of wear testing remains significant gaps, highlighting the need for innovation and progress. Pre-placed powder methods introduce challenges related to powder retention, uneven dispersion, and porosity from binder gases. The

tendency of SiC to dissolve, rather than remain as a reinforcing phase, undermines its functional contribution in many TIG-processed MMC layers.

These microstructural transformations are supported by Lacaze and Sundman's thermodynamic assessment of the Fe–C–Si system [2.145], which demonstrates that SiC is inherently unstable in molten Fe under typical TIG processing conditions. According to the ternary phase diagram, SiC decomposition leads to Fe–Si intermetallic (Fe_3Si, Fe_2Si) and graphitic carbon, especially at high silicon contents and low carbon levels. These transformations are favoured thermodynamically and supported by equilibrium phase data and silicon activity modelling. While these secondary phases can increase hardness, they contribute to brittle fracture, interfacial separation, and inconsistent wear resistance, as shown across multiple experimental studies.

These findings [2.80, 2.105, 2.131, 2.142] underscore the urgent need for an improved deposition strategy that ensures better control over ceramic reinforcement delivery, limits thermal degradation, and enables reliable evaluation of mechanical and tribological properties. This motivates the present research, which aims to overcome the limitations of pre-placed powder techniques by using tubular filler electrodes pre-filled with ceramics powder. This approach seeks to preserve ceramic integrity, improve reinforcement bonding, and enable systematic assessment of wear resistance, establishing a more viable pathway for integrating SiC into steel substrates for industrial surface engineering applications.

2.7 WC-Reinforced steel composites: challenges and insights

Due to its exceptional physical and mechanical properties, WC is among MMC's most widely utilised ceramic reinforcements. It exhibits a high melting point, excellent hardness, superior wear resistance, low friction coefficient, thermal stability and oxidation resistance [2.50, 2.146-2.148]. These attributes make WC highly desirable in surface engineering applications requiring durability in abrasive and high-load environments [2.149-2.151]. As a primary

constituent in advanced cemented carbides, WC has been extensively used in TIG-based coatings for steel components, demonstrating notable improvements in hardness, microstructural strength, and wear resistance [2.55, 2.57-2.59, 2.63, 2.119, 2.152-2.154].

Singh et al. [2.154] investigated the TIG cladding of WC–10Co–4Cr on AISI 304 stainless steel and demonstrated that the extent of WC retention was strongly influenced by heat input and arc parameters. WC particles were better preserved at lower heat input, producing a finer, denser, and harder microstructure (700–900 HV). Higher standoff distances and increased argon shielding promoted lower heat input, enhancing particle retention and reducing dissolution. Abrasive wear testing showed that samples with higher WC retention exhibited the lowest wear loss (178 mg), whereas those with more dissolution displayed higher wear (232 mg), attributed to increased matrix exposure. The dominant wear mechanisms included WC particle pull-out and matrix plastic flow.

Similarly, Yuan et al. [2.57] studied TIG-deposited Ni–WC/W_2C coatings on 40Cr steel. They described a four-stage dissolution process of fragmentation, dissolution, diffusion, and precipitation leading to carbide-rich zones forming and retaining WC surrounded by secondary phases such as Ni_2W_4C, W_2C, Fe_3W_3C, and eutectic structures. Despite the complexity of phase evolution, the coatings provided significant wear resistance improvements (42–59% material loss reduction) over uncoated substrates. XRD confirmed the presence of both primary and secondary carbide phases, while wear mechanisms included abrasive, adhesive, and oxidative modes. Tungsten-rich phases acted as heat sinks, reducing thermal damage and improving stability during sliding wear.

Buytoz et al. [2.155] evaluated WC cladding on AISI 4340 steel using TIG with pre-placed powders. Although the powder amount was measured by weight rather than thickness, the study systematically examined the effect of WC content and heat input. The deposited layer exhibited multiple carbide phases including M_7C_3, $M_{23}C6$, M_2C, Fe_3W_3C and complex

intermetallic phases. Microhardness values reached 1200 HV in samples with well-retained WC. Excessive heat input, however, caused deeper WC dissolution and the formation of brittle intermetallic, reducing wear resistance. The study concluded that controlled processing is essential for balancing WC preservation with carbide evolution. Samples with the best wear tracks featured uniform, narrow wear scars and limited matrix exposure, directly correlating to WC retention.

Wang et al. [2.153] addressed a key practical challenge in TIG processing, the absence of commercially available ceramic-filled wires. To overcome this, the authors developed powder-core filler wires using WC, with Ni and Nb added to improve toughness and crack resistance. These wires were deposited on Q355 low-alloy steel. The unalloyed WC coating exhibited severe cracking, while WC–10%Ni and WC–5%Nb coatings were crack-free. Ni promoted retained austenite and stabilised the microstructure, while Nb refined grains and suppressed cracking. Across all conditions, the microstructural analysis revealed retained and partially dissolved WC, and diffusion transition layers forming around WC particles. Microhardness increased significantly, and wear resistance improved due to progressive WC abrasion. SEM analysis showed that WC protected the matrix by acting as a sacrificial hard phase during sliding, delaying exposure of the steel substrate.

Despite these promising outcomes, the studies above reveal systemic challenges in TIG-based WC deposition. High heat input, necessary for full substrate melting, often results in the breakdown of WC into brittle tungsten-rich phases, which may reduce wear resistance and increase crack susceptibility. Even with alloying additions such as Co, Ni, and Nb that promote matrix ductility and grain refinement, controlling WC stability remains difficult. Moreover, many investigations [2.95, 2.99, 2.113, 2.120, 2.156-2.160] still rely on pre-placed powder feeding, which suffers from poor particle retention, inconsistent distribution, porosity due to binders, and weak interfacial bonding especially under dynamic or field conditions.

These systems underscore a broader problem, current deposition techniques do not offer adequate control over carbide stability, distribution, or matrix bonding. In many cases, the mechanical improvements arise from phase transformations and secondary carbide formation rather than retained ceramic particles, limiting the potential of MMC systems.

Therefore, there is a critical need for an advanced TIG-based MMC deposition strategy that:

- Preserves primary ceramic reinforcement during deposition,
- Promotes strong metallurgical bonding without excessive carbide dissolution,
- Avoids thermal cracking and porosity,
- Enables consistent, scalable powder delivery to the molten pool.

To meet these requirements, the present research introduces a novel approach using tubular filler electrodes pre-filled with SiC and WC powders, allowing better control over powder feeding, arc shielding, and heat input. This technique aims to ensure improved carbide retention, optimise microstructure, and provide durable wear-resistant surfaces for industrial applications. This method offers a viable path toward high-performance MMCs produced via TIG welding by addressing the core limitations identified across prior studies.

2.8 References

[2.1] Fauchais, P.L., J.V. Heberlein, and M.I. Boulos, Thermal spray fundamentals: from powder to part. 2014: Springer Science & Business Media.

[2.2] Pileggi, R., et al., Tribo-corrosion behaviour of chromium carbide based coatings deposited by HVOF. Surface and Coatings Technology, 2015. 268: p. 247-251.

[2.3] Vakis, A.I., et al., Modeling and simulation in tribology across scales: An overview. Tribology International, 2018. 125: p. 169-199.

[2.4] Abdi, S. and S. Lebaili, Alternative to chromium, a hard alloy powder NiCrBCSi (Fe) coatings thermally sprayed on 60CrMn4 steel. Phase and comportements. Physics Procedia, 2009. 2(3): p. 1005-1014.

[2.5] Bolelli, G., et al., Corrosion resistance of HVOF-sprayed coatings for hard chrome replacement. Corrosion science, 2006. 48(11): p. 3375-3397.

[2.6] Winter, K.-M., J. Kalucki, and D. Koshel, Process technologies for thermochemical surface engineering, in Thermochemical surface engineering of steels. 2015, Elsevier. p. 141-206.

[2.7] Bell, T., Surface engineering of austenitic stainless steel. Surface engineering, 2002. 18(6): p. 415-422.

[2.8] Dong, H., et al., Surface engineering to improve tribological performance of Ti–6Al–4V. Surface engineering, 1997. 13(5): p. 402-406.

[2.9] Burakowski, T. and T. Wierzchon, Surface engineering of metals: principles, equipment, technologies. 1998: CRC press.

[2.10] Escobar, J., et al., Improvement of cavitation erosion resistance of a duplex stainless steel through friction stir processing (FSP). Wear, 2013. 297(1-2): p. 998-1005.

[2.11] Mukherjee, S. and A. Ghosh, Friction stir processing of direct metal deposited copper–nickel 70/30. Materials Science and Engineering: A, 2011. 528(9): p. 3289-3294.

[2.12] Schirmeisen, A., Wear: One atom after the other. Nat Nanotechnol, 2013. 8(2): p. 81-2.

[2.13] 13Bishop, R.F., R. Hill, and N. Mott, The theory of indentation and hardness tests. Proceedings of the Physical Society, 1945. 57(3): p. 147.

[2.14] Archard, J.F. and W. Hirst, The wear of metals under unlubricated conditions. Proceedings of the Royal Society of London. Series A. Mathematical and Physical Sciences, 1956. 236(1206): p. 397-410.

[2.15] Colaço, R. and A.P. Serro, Nanoscale wear of hard materials: An overview. Current Opinion in Colloid & Interface Science, 2020. 47: p. 118-125.

[2.16] Holm, E., R. Holm, and E.I. Shobert, Theory of hardness and measurements applicable to contact problems. Journal of Applied Physics, 1949. 20(4): p. 319-327.

[2.17] Archard, J., Contact and rubbing of flat surfaces. Journal of applied physics, 1953. 24(8): p. 981-988.

[2.18] 18. Hirst, W. and J. Lancaster, Surface film formation and metallic wear. Journal of Applied Physics, 1956. 27(9): p. 1057-1065.

[2.19] Lim, S., M. Ashby, and J. Brunton, Wear-rate transitions and their relationship to wear mechanisms. Acta metallurgica, 1987. 35(6): p. 1343-1348.

[2.20] Mutton, P. and J. Watson, Some effects of microstructure on the abrasion resistance of metals. Wear, 1978. 48(2): p. 385-398.

[2.21] Moore, M., The relationship between the abrasive wear resistance, hardness and microstructure of ferritic materials. Wear, 1974. 28(1): p. 59-68.

[2.22] Nakajima, K. and Y. Mizutani, Structural change of the surface layer of low carbon steels due to abrading. Wear, 1969. 13(4-5): p. 283-292.

[2.23] Garbar, I. and J. Skorinin, Metal surface layer structure formation under sliding friction. Wear, 1978. 51(2): p. 327-336.

[2.24] Fink, M., Wear oxidation—a new component of wear. Trans. Am. Soc. Steel Treat, 1930. 18: p. 1026-1034.

[2.25] Wang, S.Q., et al., Mild-to-severe wear transition and transition region of oxidative wear in steels. Wear, 2013. 306(1-2): p. 311-320.

[2.26] Hatchett, C., IV. Experiments and observations on the various alloys, on the specific gravity, and on the comparative wear of gold. Being the substance of a report made to the Right Honourable the Lords of the Committee of Privy Council, appointed to take

into consideration the state of the coins of this Kingdom, and the present establishment and constitution of his Majesty's Mint. Philosophical Transactions of the Royal Society of London, 1803(93): p. 43-194.

[2.27] Earles, S. and N. Tenwick, Friction and wear properties of Nimonic 75 at ambient temperatures up to 810 C. Wear, 1972. 19(3): p. 287-299.

[2.28] Čikara, D., M. Rakin, and A. Todić, Cast Steel-SiC composites as wear resistant materials. FME Transactions, 2009. 37(3): p. 151-155.

[2.29] Peng, D.X., et al., Wear behavior of ceramic powder cladded on carbon steel surface by gas tungsten arc welding. Industrial Lubrication and Tribology, 2013. 65(2): p. 129-134.

[2.30] Monfared, A., A.H. Kokabi, and S. Asgari, Microstructural studies and wear assessments of Ti/TiC surface composite coatings on commercial pure Ti produced by titanium cored wires and TIG process. Materials Chemistry and Physics, 2013. 137(3): p. 959-966.

[2.31] Roy, M., Surface engineering for enhanced performance against wear. 2013: Springer.

[2.32] Zhang, F., et al., Improving the impact wear properties of medium carbon steel by adjusting microstructure under alternating quenching in water and air. Wear, 2023. 512-513.

[2.33] Jiang, S., et al., Study on the Microstructure and Mechanical Properties of Martensitic Wear-Resistant Steel. Crystals, 2023. 13(8).

[2.34] Chong, P., H.C. Man, and T.M. Yue, Microstructure and wear properties of laser surface-cladded Mo–WC MMC on AA6061 aluminum alloy. Surface and Coatings Technology, 2001. 145(1-3): p. 51-59.

[2.35] Berns, H., Comparison of wear resistant MMC and white cast iron. Wear, 2003. 254(1-2): p. 47-54.

[2.36] Singh, L., B. Singh, and K.K. Saxena, Manufacturing techniques for metal matrix composites (MMC): an overview. Advances in Materials and Processing Technologies, 2020. 6(2): p. 441-457.

[2.37] Sarmah, P. and K. Gupta, Recent Advancements in Fabrication of Metal Matrix Composites: A Systematic Review. Materials (Basel), 2024. 17(18).

[2.38] Czuprynski, A. and M. Zuk, Matrix Composite Coatings Deposited on AISI 4715 Steel by Powder Plasma-Transferred Arc Welding. Part 3. Comparison of the Brittle Fracture Resistance of Wear-Resistant Composite Layers Surfaced Using the PPTAW Method. Materials (Basel), 2021. 14(20).

[2.39] Rajak, D.K., et al., Critical overview of coatings technology for metal matrix composites. Journal of Bio-and Tribo-Corrosion, 2020. 6: p. 1-18.

[2.40] 40. Dadbakhsh, S., et al., Selective Laser Melting to Manufacture "In Situ" Metal Matrix Composites: A Review. Advanced Engineering Materials, 2019. 21(3).

[2.41] Ramanathan, A., P.K. Krishnan, and R. Muraliraja, A review on the production of metal matrix composites through stir casting–Furnace design, properties, challenges, and research opportunities. Journal of Manufacturing processes, 2019. 42: p. 213-245.

[2.42] Vijayarangan, S., N. Rajamanickam, and V. Sivananth, Evaluation of metal matrix composite to replace spheroidal graphite iron for a critical component, steering knuckle. Materials & Design, 2013. 43: p. 532-541.

[2.43] Chawla, N. and K. Chawla, Metal-matrix composites in ground transportation. JoM, 2006. 58: p. 67-70.

[2.44] Terry, B. and O. Chinyamakobvu, Assessment of the reaction of SiC powders with iron-based alloys. Journal of materials science, 1993. 28: p. 6779-6784.

[2.45] Pei, Y.T., et al., Microstructure of laser-clad SiC-(Ni alloy) composite coating. Materials Science and Engineering: A, 1995. 194(2): p. 219-224.

[2.46] Kalogeropoulou, S., L. Baud, and N. Eustathopoulos, Relationship between wettability and reactivity in Fe/SiC system. Acta metallurgica et materialia, 1995. 43(3): p. 907-912.

[2.47] Starke, U., et al., High quality iron silicide films by simultaneous deposition of iron and silicon on Si (111). Journal of applied physics, 2002. 91(9): p. 6154-6161.

[2.48] Tang, W., et al., A study of the solid state reaction between silicon carbide and iron. Materials chemistry and physics, 2002. 74(3): p. 258-264.

[2.49] Abe, N., et al., Formation of WC-Co layers by an electron beam cladding method and evaluation of the layer properties. Vacuum, 2000. 59(1): p. 373-380.

[2.50] Koc, R. and S.K. Kodambaka, Tungsten carbide (WC) synthesis from novel precursors. Journal of the European Ceramic Society, 2000. 20(11): p. 1859-1869.

[2.51] Huang, S.W., M. Samandi, and M. Brandt, Abrasive wear performance and microstructure of laser clad WC/Ni layers. Wear, 2004. 256(11-12): p. 1095-1105.

[2.52] Bolelli, G., L. Lusvarghi, and M. Barletta, HVOF-sprayed WC–CoCr coatings on Al alloy: effect of the coating thickness on the tribological properties. Wear, 2009. 267(5-8): p. 944-953.

[2.53] Jankauskas, V., et al., Effect of WC grain size and content on low stress abrasive wear of manual arc welded hardfacings with low-carbon or stainless steel matrix. Wear, 2015. 328-329: p. 378-390.

[2.54] Wang, G., et al., Improving the wear resistance of as-sprayed WC coating by deep cryogenic treatment. Materials Letters, 2016. 185: p. 363-365.

[2.55] Hulka, I., et al., Influence of the laser cladding parameters on the morphology, wear and corrosion resistance of WC-Co/NiCrBSi composite coatings. Materials, 2021. 14(19): p. 5583.

[2.56] Oleiwi, A.A. and A.S.J. Jilabi, The Effects of Travel Speed of Tungsten Inert Gas Cladding of Tungsten Carbide and Nickel Composites on the Microstructure of Stainless Steel. Advances in Science and Technology Research Journal, 2024. 18(4): p. 177-190.

[2.57] Yuan, J., et al., Effect of the dissolution characteristic of tungsten carbide particles on microstructure and properties of Ni-WC/W2C reinforcement coating manufactured by TIG cladding. International Journal of Refractory Metals and Hard Materials, 2023. 110.

[2.58] Sun, S., et al., Preparing WC-Ni coatings with laser cladding technology: A review. Materials Today Communications, 2023. 37.

[2.59] Jilabi, A.S.J.A.Z. and H.N.A. Alakal, A review on laser and TIG cladding of WC-Ni composite on steel alloys, in 4th International Scientific Conference of Alkafeel University (Iscku 2022). 2023.

[2.60] Gao, W., et al., Effect of laser cladding speed on microstructure and properties of titanium alloy coating on low carbon steel. Surface and Coatings Technology, 2022. 451.

[2.61] Ranjan, R. and A.K. Das, Recent Advancements in Surface Modification by Gas Tungsten Arc Cladding Technique: A Review. Advanced Materials Research, 2022. 1173: p. 113-122.

[2.62] Feest, E., Metal matrix composites for industrial application. Materials & Design, 1986. 7(2): p. 58-64.

[2.63] Zhang, D., et al., Thermodynamic analysis of the interface reaction and thermal stress of WCp/Fe composites. Ceramics International, 2020. 46(16): p. 26210-26215.

[2.64] Bandhu, D., et al., Effect of Metal-Cored Filler Wire on Surface Morphology and Micro-Hardness of Regulated Metal Deposition Welded ASTM A387-Gr.11-Cl.2 Steel Plates. Materials (Basel), 2022. 15(19).

[2.65] Kang, L., et al., Mechanical properties and microstructure of laser-cladding additively manufactured 316L stainless steel sheets. Journal of Constructional Steel Research, 2022. 199.

[2.66] Vorkötter, C., et al., Additive Manufacturing of Columnar Thermal Barrier Coatings by Laser Cladding of Ceramic Feedstock. Advanced Materials Technologies, 2022. 7(10).

[2.67] Shi, F.K., et al., In-situ synthesis of NiCoCrMnFe high entropy alloy coating by laser cladding. Optics & Laser Technology, 2022. 151.

[2.68] Bose, S. and S. Das, Effect of Heat Input on Corrosion Resistance of 316 Austenitic Stainless Steel Cladding on Low-Carbon Steel Plate, in Advances in Micro and Nano Manufacturing and Surface Engineering. 2023. p. 163-176.

[2.69] Pradeep, D.G., C.V. Venkatesh, and H.S. Nithin, Review on Tribological and Mechanical Behavior in HVOF Thermal-sprayed Composite Coatings. Journal of Bio- and Tribo-Corrosion, 2022. 8(1).

[2.70] Li, C.-J., et al., The Bonding Formation during Thermal Spraying of Ceramic Coatings: A Review. Journal of Thermal Spray Technology, 2022. 31(4): p. 780-817.

[2.71] Sathish, M., N. Radhika, and B. Saleh, Duplex and Composite Coatings: A Thematic Review on Thermal Spray Techniques and Applications. Metals and Materials International, 2022. 29(5): p. 1229-1297.

[2.72] Ray, J., S.K. Acharyya, and D. Misra, Review on TIG cladding process and its comparative study with laser surface treatment, in INTELLIGENT SYSTEMS: A STEP TOWARDS SMARTER ELECTRICAL, ELECTRONIC AND MECHANICAL ENGINEERING: Proceedings of 2nd International Conference on Industrial Electronics, Mechatronics, Electrical and Mechanical Power (IEMPOWER), 2021. 2022.

[2.73] Arif, Z.U., et al., Laser deposition of high-entropy alloys: A comprehensive review. Optics & Laser Technology, 2022. 145.

[2.74] Gao, Y., et al., Microstructure evolution and wear resistance of laser cladded 316L stainless steel reinforced with in-situ VC-Cr7C3. Surface and Coatings Technology, 2022. 435.

[2.75] Rakesh, N., et al., Effect of fluxes on weld penetration during TIG welding – A review. Materials Today: Proceedings, 2023. 72: p. 3040-3048.

[2.76] Kumar, K., et al., A review on TIG welding technology variants and its effect on weld geometry. Materials Today: Proceedings, 2022. 50: p. 999-1004.

[2.77] Kumar, G.S., et al., Investigation of the TIG Welding Process for Joining AA6082 Alloy Using Grey Relational Analysis. Advances in Materials Science and Engineering, 2022. 2022: p. 1-8.

[2.78] Kumar Das, A., Recent developments in TIG torch assisted coating on austenitic stainless steel: A critical review. Materials Today: Proceedings, 2022. 57: p. 1846-1851.

[2.79] Alam, M.S. and A.K. Das, Research Progress in Gas Tungsten Arc Cladding on Steel: A Critical Review, in Recent Advances in Manufacturing Processes and Systems. 2022. p. 859-867.

[2.80] Kumar, A. and A.K. Das, Evolution of microstructure and mechanical properties of Co-SiC tungsten inert gas cladded coating on 304 stainless steel. Engineering Science and Technology, an International Journal, 2021. 24(3): p. 591-604.

[2.81] Sekhar, B.R., et al., Wear characteristic of TiC coated AISI 1020 mild steel fabricated by TIG cladding method. Materials Today: Proceedings, 2020. 26: p. 3288-3291.

[2.82] Shrivas, S.P., et al., Investigation of TIG welding parameters to improve strength. Materials Today: Proceedings, 2020. 26: p. 1897-1902.

[2.83] Kumar, S. and R. Kumar, Influence of processing conditions on the properties of thermal sprayed coating: a review. Surface Engineering, 2021. 37(11): p. 1339-1372.

[2.84] Knotek, O., Thermal spraying and detonation gun processes. Handbook of Hard Coatings Deposition Technologies, Properties and Applications, William Andrew, 2001.

[2.85] Bhushan, B. and B.K. Gupta, Handbook of tribology: materials, coatings, and surface treatments. 1991.

[2.86] Odhiambo, J.G., et al., Porosity and Its Significance in Plasma-Sprayed Coatings. Coatings, 2019. 9(7).

[2.87] Li, F., et al., Microstructural study of MMC layers produced by combining wire and coaxial WC powder feeding in laser direct metal deposition. Optics & Laser Technology, 2016. 77: p. 134-143.

[2.88] Devojno, O.G., et al., On the formation features, microstructure and microhardness of single laser tracks formed by laser cladding of a NiCrBSi self-fluxing alloy. Optics and Lasers in Engineering, 2018. 106: p. 32-38.

[2.89] Muvvala, G., D. Patra Karmakar, and A.K. Nath, Online monitoring of thermo-cycles and its correlation with microstructure in laser cladding of nickel based super alloy. Optics and Lasers in Engineering, 2017. 88: p. 139-152.

[2.90] Hofman, J.T., et al., FEM modeling and experimental verification for dilution control in laser cladding. Journal of Materials Processing Technology, 2011. 211(2): p. 187-196.

[2.91] Liu, C., et al., Modeling of thermal behavior and microstructure evolution during laser cladding of AlSi10Mg alloys. Optics & Laser Technology, 2020. 123.

[2.92] Patel, N.S. and R.B. Patel, A review on parametric optimization of TIG welding. International Journal of Computational Engineering Research, 2014. 4(1): p. 27-31.

[2.93] Mridha, S. and B.S. Ng, Addition of ceramic particles to TIG melted titanium surfaces. Surface Engineering, 1999. 15(3): p. 210-215.

[2.94] Varghese, V.M.J., M.R. Suresh, and D.S. Kumar, Recent developments in modeling of heat transfer during TIG welding—a review. The International Journal of Advanced Manufacturing Technology, 2012. 64(5-8): p. 749-754.

[2.95] Jeyaprakash, N., A. Haile, and M. Arunprasath, The parameters and equipments used in TIG welding: A review. The International Journal of Engineering and Science (IJES), 2015. 4(2): p. 11-20.

[2.96] Schneider, C., et al., Optimizing the Parameters of TIG-MIG/MAG Hybrid Welding on the Geometry of Bead Welding Using the Taguchi Method. Journal of Manufacturing and Materials Processing, 2017. 1(2).

[2.97] Fande, A.W., R.V. Taiwade, and L. Raut, Development of activated tungsten inert gas welding and its current status: A review. Materials and Manufacturing Processes, 2022. 37(8): p. 841-876.

[2.98] <IRJET_Review_on_Investigate_the_TIG_Weld.pdf>.

[2.99] Xu, G., et al., Comparison between diode laser and TIG cladding of Co-based alloys on the SUS403 stainless steel. Surface and Coatings Technology, 2006. 201(3-4): p. 1138-1144.

[2.100] Madadi, F., F. Ashrafizadeh, and M. Shamanian, Optimization of pulsed TIG cladding process of stellite alloy on carbon steel using RSM. Journal of Alloys and Compounds, 2012. 510(1): p. 71-77.

[2.101] Muigai, M.N., et al., TIG Welding Methods of Repairing Steel Components with Stainless Steel Coatings. Tribology in Industry, 2022. 44(3): p. 434-448.

[2.102] Vahdatkhah, P., S.R. Tabatabaee Kopaee, and H. Vahdat Khah, Weld repair of gas turbine disc: optimization of pulsed TIG welding process parameters and microstructural analysis of Cr–Mo-V Steel. The International Journal of Advanced Manufacturing Technology, 2022. 123(1-2): p. 213-232.

[2.103] Mridha, S. and T. Baker, Metal matrix composite layer formation with 3 μm SiCp powder on IMI318 titanium alloy surfaces through laser treatment. Journal of materials processing technology, 1997. 63(1-3): p. 432-437.

[2.104] Munoz-Escalona, P., S. Mridha, and T. Baker, Advances in Surface Engineering Using TIG Processing to Incorporate Ceramic Particulates into Low Alloy and Microalloyed Steels – A Review. Advances in Science and Technology Research Journal, 2021. 15(3): p. 88-98.

[2.105] Baker, T.N., et al., Role of preplaced silicon on a TIG processed SiC incorporated microalloyed steel. Materials Science and Technology, 2020. 36(12): p. 1349-1363.

[2.106] Muñoz-Escalona, P., et al., Silicon carbide particulates incorporated into microalloyed steel surface using TIG: microstructure and properties. Materials Science and Technology, 2019. 36(1): p. 17-32.

[2.107] Muñoz-Escalona, P., et al., Comparison of empirical and predicted substrate temperature during surface melting of microalloyed steel using TIG technique and considering three shielding gases. Applied Surface Science, 2019. 477: p. 179-183.

[2.108] Muñoz-Escalona, P., S. Mridha, and T.N. Baker, Effect of shielding gas on the properties and microstructure of melted steel surface using a TIG torch. Advances in Materials and Processing Technologies, 2016. 1(3-4): p. 435-443.

[2.109] Muñoz-Escalona, P., S. Mridha, and T.N. Baker, Effect of silicon carbide particle size on microstructure and properties of a coating layer on steel produced by TIG technique. Advances in Materials and Processing Technologies, 2016. 2(4): p. 451-460.

[2.110] Patel, P., S. Mridha, and T.N. Baker, Influence of shielding gases on preheat produced in surface coatings incorporating SiC particulates into microalloy steel using TIG technique. Materials Science and Technology, 2014. 30(12): p. 1506-1514.

[2.111] Mridha, S., et al., Effect of voltage on the consolidation of TiC particulates on steel substrate fused by TIG welding arc. International Journal of Mechanical and Materials Engineering, 2012. 7(1).

[2.112] Mridha, S., et al., Intermetallic coatings produced by TIG surface melting. Journal of Materials Processing Technology, 2001. 113(1-3): p. 516-520.

[2.113] Buytoz, S., M. Ulutan, and M.M. Yildirim, Dry sliding wear behavior of TIG welding clad WC composite coatings. Applied Surface Science, 2005. 252(5): p. 1313-1323.

[2.114] Mondal, A., et al., Influence of heat input on weld bead geometry using duplex stainless steel wire electrode on low alloy steel specimens. Cogent Engineering, 2016. 3(1).

[2.115] Khan, T.I. and D. Fowles, Surface modification of Ti–6Al–4V alloy using metal arc heat source. Surface Engineering, 2013. 13(3): p. 257-259.

[2.116] Reddy, G.H., S. Arul, and R. Sellamuthu, Improving Surface Hardness of Mild Steel Plates by Addition of Silicon Carbide Using Gas Tungsten Arc as Heat Source. Applied Mechanics and Materials, 2014. 592-594: p. 879-882.

[2.117] Gan, Z., et al., Modeling of thermal behavior and mass transport in multi-layer laser additive manufacturing of Ni-based alloy on cast iron. International Journal of Heat and Mass Transfer, 2017. 111: p. 709-722.

[2.118] Lai, Q., et al., Influences of depositing materials, processing parameters and heating conditions on material characteristics of laser-cladded hypereutectoid rails. Journal of Materials Processing Technology, 2019. 263: p. 1-20.

[2.119] Singh, J., L. Thakur, and S. Angra, An investigation on the parameter optimization and abrasive wear behaviour of nanostructured WC-10Co-4Cr TIG weld cladding. Surface and Coatings Technology, 2020. 386.

[2.120] Dadfar, M., et al., Effect of TIG welding on corrosion behavior of 316L stainless steel. Materials Letters, 2007. 61(11-12): p. 2343-2346.

[2.121] Vidyarthy, R.S., D.K. Dwivedi, and M. Vasudevan, Influence of M-TIG and A-TIG Welding Process on Microstructure and Mechanical Behavior of 409 Ferritic Stainless Steel. Journal of Materials Engineering and Performance, 2017. 26(3): p. 1391-1403.

[2.122] Patil, T., et al., COOLING SYSTEM IN TIG WELDING BY USING VAPOUR COMPRESSION CYCLE. 2018.

[2.123] Naing, T.H. and P. Muangjunburee, Effect of Conventional and Pulsed TIG Welding on Microstructural and Mechanical Characteristics of AA 6082-T6 Repair Welds. Journal of Wuhan University of Technology-Mater. Sci. Ed., 2023. 38(4): p. 865-876.

[2.124] Jasbir Singh, L.T., Surjit Angra, Effect of argon flow rate and standoff distance on the microstructure and wear behaviour of WCCoCr TIG cladding. Journal of Physics, 2019.

[2.125] Bhoi, S., et al., Effect of Grain Refinement on Tribological Study of Low Carbon Steel. Transactions of the Indian Institute of Metals, 2021. 74(6): p. 1489-1499.

[2.126] P. K, J., et al., TIG welding parameters optimization of Al–Si–Mg ternary alloy–SiC powder reinforced composites using Taguchi and RSM techniques. Cogent Engineering, 2022. 9(1).

[2.127] Sahoo, C.K. and M. Masanta, Microstructure and mechanical properties of TiC-Ni coating on AISI304 steel produced by TIG cladding process. Journal of Materials Processing Technology, 2017. 240: p. 126-137.

[2.128] Sahoo, C.K., L. Soni, and M. Masanta, Evaluation of microstructure and mechanical properties of TiC/TiC-steel composite coating produced by gas tungsten arc (GTA) coating process. Surface and Coatings Technology, 2016. 307: p. 17-27.

[2.129] Woldan, A., J. Kusiński, and E. Tasak, The microstructure of plain carbon steel laser-alloyed with silicon carbide. Materials Chemistry and Physics, 2003. 81(2-3): p. 507-509.

[2.130] Srijampan, W., et al., Effects of silicon carbide contents on the microstructure of sintered steels. ScienceAsia, 2021. 47S(1).

[2.131] Alam, M.S., Recent Trends in Surface Cladding on AISI 1045 Steel Substrate: A Review, in Functional Materials and Applied Physics. 2022. p. 94-101.

[2.132] Chen, J.-P., L. Gu, and G.-J. He, A review on conventional and nonconventional machining of SiC particle-reinforced aluminium matrix composites. Advances in Manufacturing, 2020. 8(3): p. 279-315.

[2.133] Paijan, L.H., et al., Influence of ceramic particles size on the incorporation of SiC into stainless steel material using 480 J/mm heat input for tribological applications. Jurnal Tribologi, 2023. 37: p. 14-27.

[2.134] Zhai, W., et al., Recent Progress on Wear-Resistant Materials: Designs, Properties, and Applications. Adv Sci (Weinh), 2021. 8(11): p. e2003739.

[2.135] Zhang, W., Tribology of SiC ceramics under lubrication: Features, developments, and perspectives. Current Opinion in Solid State and Materials Science, 2022. 26(4).

[2.136] Mithun, C., R. Sellamuthu, and R. Saravanan, Effect of surface modification on microstructure, hardness and wear rate of steels with 0.2%, 0.4% and 1.1 Wt% C by the addition of Titanium using Gas Tungsten Arc. Materials Today: Proceedings, 2018. 5(2): p. 7586-7594.

[2.137] Chandra, D., N.R. Chauhan, and S. Rajesha, Hardness and toughness evaluation of developed Al metal matrix composite using stir casting method. Materials Today: Proceedings, 2020. 25: p. 872-876.

[2.138] Hu, Y., et al., Experimental study on wear properties of wheel and rail materials with different hardness values. Wear, 2021. 477.

[2.139] Ghumman, K.Z., et al., Experimental investigation of effect of welding parameters on surface roughness, micro-hardness and tensile strength of AISI 316L stainless steel welded joints using 308L filler material by TIG welding. Journal of Materials Research and Technology, 2022. 21: p. 220-236.

[2.140] Buytoz, S., Microstructural properties of SiC based hardfacing on low alloy steel. Surface and Coatings Technology, 2006. 200(12-13): p. 3734-3742.

[2.141] Majumdar, J.D., Development of in-situ composite surface on mild steel by laser surface alloying with silicon and its remelting. Surface and Coatings Technology, 2010. 205(7): p. 1820-1825.

[2.142] Maleque, M. and M. Afiq. Melting of SiC powders preplaced duplex stainless steel using TIG welding. in IOP Conference Series: Materials Science and Engineering. 2018. IOP Publishing.

[2.143] Lailatul, P. and M. Abd Maleque, Tribological properties of surface coated duplex stainless steel containing SiC ceramic particles. Jurnal Tribologi, 2018. 18: p. 136-148.

[2.144] Sharma, D., et al., Surface modification of microalloyed steel by silicon carbide reinforcement using tungsten inert gas arcing. Materials Research Express, 2018. 6(3).

[2.145] Lacaze, J. and B. Sundman, An assessment of the Fe-C-Si system. Metallurgical Transactions A, 1991. 22: p. 2211-2223.

[2.146] Schwartzkopf, P., et al., Refractory hard metals: borides, carbides, nitrides, and silicides. The basic constituents of cemented hard metals and their use as high-temperature materials. 1953: Macmillan.

[2.147] Luković, J., et al., Synthesis and characterization of tungsten carbide fine powders. Ceramics International, 2015. 41(1): p. 1271-1277.

[2.148] Kosolapova, T.Y., Carbides: properties, production, and applications. 2012: Springer Science & Business Media.

[2.149] Rieck, G.D., Tungsten and its Compounds. 2013: Elsevier.

[2.150] Beardsley, T., Fine grain. Scientific American, 1992. 267(4): p. 114-115.

[2.151] Sabzi, M., S.M. Dezfuli, and S.M. Far, Deposition of Ni-tungsten carbide nanocomposite coating by TIG welding: Characterization and control of microstructure and wear/corrosion responses. Ceramics International, 2018. 44(18): p. 22816-22829.

[2.152] Zhang, M., et al., Microstructure and Properties of WC-Reinforced Inconel 718 Alloy Cladding Layer by TIG on Low Carbon Steel Surface. Transactions of the Indian Institute of Metals, 2023. 77(1): p. 219-227.

[2.153] Wang, Y., et al., Microstructure and property of tungsten carbide particulate reinforced wear resistant coating by TIG cladding. International Journal of Refractory Metals and Hard Materials, 2021. 100.

[2.154] Singh, J., L. Thakur, and S. Angra, Abrasive wear behavior of WC-10Co-4Cr cladding deposited by TIG welding process. International Journal of Refractory Metals and Hard Materials, 2020. 88.

[2.155] Buytoz, S., M.M. Yildirim, and H. Eren, Microstructural and microhardness characteristics of gas tungsten are synthesized Fe–Cr–C coating on AISI 4340. Materials Letters, 2005. 59(6): p. 607-614.

[2.156] Mridha, S., Titanium nitride layer formation by TIG surface melting in a reactive environment. Journal of Materials Processing Technology, 2005. 168(3): p. 471-477.

[2.157] Ulutan, M., et al., Microstructure and Wear Behavior of TIG Surface-Alloyed AISI 4140 Steel. Tribology Transactions, 2010. 54(1): p. 67-79.

[2.158] Tosun, G., Ni–WC coating on AISI 1010 steel using TIG: microstructure and microhardness. Arabian Journal for Science and Engineering, 2014. 39: p. 2097-2106.

[2.159] Bello, K.A., et al., Preparation and characterisation of TIG-alloyed hybrid composite coatings for high-temperature tribological applications. Transactions of the IMF,

[2.160] Saroj, S., et al., Sliding abrasive wear characteristic of TIG cladded TiC reinforced Inconel825 composite coating. International Journal of Refractory Metals and Hard Materials, 2017. 69: p. 119-130.

Chapter 3 Materials & methods

3.1 Materials

3.1.1 Material Selection Strategy

The material selection in this study followed a structured, progressive approach to developing a novel MMC system using TIG welding. Criteria such as chemical compatibility, weldability, and retainment of ceramic reinforcements SiC and WC within the steel matrix guided the process. A low carbon steel base metal (LCS-BM) was initially chosen due to its industrial relevance and poorer inherent wear resistance. The development proceeded through multiple tubular filler combinations, starting with medium carbon steel tube (MCS-T), then low carbon steel tube (LCS-T), 304L stainless steel tube (304LSS-T), and finally 316L stainless steel tube (316LSS-T). Chapter 4 presents the optimisation of the tubular filler material, including powder content, filler geometry, and shielding configuration. Among these, 316LSS-T demonstrated the most effective retention of ceramic particles with minimal dissolution, supported by favourable alloying elements, including Ni, Cr, and Mo.

Based on this progression, 316LSS-T was selected as the filler material for all further experiments. In Chapter 5, LCS-BM and 316LSS-BM were used as base metals for wear testing, with 316LSS-T remaining the consistent filler across all samples. To benchmark performance, a commercial hard-facing electrode (HF600) was used to compare it with the developed ceramic-material-infused electrode. Pin-on-disc wear testing employed a cast iron pin under varying loads to simulate industrial conditions.

3.1.2 Base metals

3.1.2.1 LCS-BM

BS970 LCS was selected for its good weldability, machinability, and affordability despite its poor wear resistance. Its composition is listed in Table 3.1, and its microstructure revealed typical ferrite and pearlite phases under optical microscopy.

Table 3.1 Chemical composition wt% of BS970 LCS (supplier certificate)

Element	C	Si	Mn	P	S	Fe
wt %	0.16	0.19	0.76	0.016	0.007	Bal.

3.1.2.2 AISI 316LSS-BM

AISI 316LSS was used as a base metal in the wear tests due to its stable austenitic structure and suitability for embedding ceramic reinforcements. Table 3.2 lists the chemical composition. The microstructure was examined under optical microscopy and showed fully austenitic microstructure of as-received material.

Table 3.2 Chemical composition wt% of AISI 316LSS (supplier certificate)

Element	C	Si	Mn	Cr	Ni	Mo	Fe
wt %	0.03	0.6	1.2	18	12.1	2.6	Bal.

3.1.3 Tubular filler materials

3.1.3.1 MCS-T

In the early phase, upper match MCS with a higher carbon content than LCS-BM, was used to assess its suitability as a tubular filler for LCS-BM surface. This setup evaluated the effect of ceramic particle addition and the unique arc control offered by manual TIG welding when joining these steels. The higher carbon content was expected to promote strong metallurgical bonding with the substrate and potentially form a martensitic matrix during solidification. The chemical composition of the MCS-T is shown in Table 3.3.

Table 3.3 Chemical composition of AIS wt% I 1040 MCS (supplier certificate)

Element	C	Si	Mn	P	S	Fe
wt%	0.37	0.2	0.5	0.03	0.02	Bal.

3.1.3.2 LCS-T

In the second stage of experimentation, a BS970 LCS-T filler was used to match the BS970 LCS-BM, forming a self-matching system. This configuration aimed to evaluate the effect of chemical matching on the quality of the deposit, including metallurgical bonding and defect minimisation. The lower carbon content in the LCS-T was expected to reduce residual stresses,

improve weldability, and refine the diffusion dynamics at the weld interface (based on previous section MCS-T results). It also offered potential benefits in reducing the dissolution of ceramic particles by minimising aggressive chemical reactions during the high-temperature phase. The LCS-T's chemical composition and microstructure are identical to those described in LCS-BM (section 3.1.2.1).

3.1.3.3 AISI 304LSS-T

304LSS is a widely used austenitic stainless steel, recognised for its mechanical stability and excellent weldability. It was introduced in the third experimentation stage, following earlier trials with MCS-T and LCS-T fillers, revealing significant challenges in retaining hard ceramic particles during the TIG deposition process. These findings guided the selection of stainless-steel fillers, particularly due to their alloying elements, Cr and Ni, which were expected to enhance austenitic phase stability, improve wettability, and promote stronger bonding between the steel matrix and ceramic reinforcements. Using 304LSS-T thus allowed for the evaluation of an austenitic filler's influence on microstructural integrity and reinforcement retention. The chemical composition of 304LSS-T is presented in Table 3.4.

Table 3.4 Chemical composition wt% of AISI 304LSS-T (supplier certificate)

Element	C	Si	Mn	P	Cr	Ni	Fe
wt %	0.03	0.2	1.0	0.04	18.2	7.3	Bal.

3.1.3.4 AISI 316LSS-T

AISI 316LSS-T was selected as the final tubular filler material. Compared to 304L, 316L contains Mo which, alongside Ni and Cr plays a critical role in improving weld stability. Ni stabilises the austenitic phase as austinite stabiliser [3.1], Cr promotes particle-matrix bonding as a carbide reformer [3.2], and Mo refines carbides as carbide refiner while suppressing carbon mobility [3.3, 3.4]. Mo achieves this by forming stable carbide phases that trap carbon within the crystal lattice, limiting diffusion and helping protect ceramic particles from dissolution during deposition.

3.1.4 Ceramic reinforcement materials

3.1.4.1 Silicon carbide

SiC powder was selected as a reinforcement material due to its exceptional properties, including high hardness, superior wear resistance, low density, high thermal conductivity, and good electrical conductivity [3.5-3.8]. These characteristics make SiC ideal for enhancing the surface performance of MMC under abrasive and high-load conditions. As determined by scanning electron microscopy, the particle size of the SiC powder ranged from 29 μm to 118 μm. The particles exhibited an angular and edgy morphology, favourable for mechanical interlocking within the steel matrix.

3.1.4.2 Tungsten carbide

WC10%Co powder was selected as a reinforcement material due to its widespread application in developing MMC. This material combines the extreme hardness and wear resistance of WC with the toughness and strength imparted by Cobalt (Co) [3.9], which serves as a metallic binder. The WC-Co powder used in this study contained a mix of angular and spherical particles, with sizes ranging from 75 μm to 150 μm. Scanning electron microscopy examined the powder morphology and composition. The presence of sharp angular particles is particularly significant, as particles with smaller curvature radii tend to melt at lower temperatures than their alloy counterparts, according to the solidification theory [3.10, 3.11]. This makes their retention during deposition a critical factor (particle/matrix interface) in MMC performance.

3.1.5 HF600 hard facing electrode.

The HF600 is a commercially available filler metal designed for wear-resistant applications, particularly under abrasive and sliding conditions. Optimised for TIG welding, HF600 forms a hard microstructure upon solidification, making it suitable for enhancing the durability of industrial components. In this study, HF600 was used to deposit hard-facing layers on both

LCS-BM and 316LSS-BM. The resulting deposition was analysed regarding its microstructure, hardness, and wear resistance, serving as a benchmark for comparison against the developed tubular filler. The chemical composition of the HF600 electrode, is provided in Table 3.5.

Table 3.5 Chemical composition wt% of HF600 (supplier certificate)

Element	C	Si	Cr	Cu	P	Mn	Ni	Fe
wt%	0.46	3.05	9.1	0.25	0.04	0.06	0.5	Bal.

3.2 Methods

3.2.1 Experimental methods

3.2.1.1 Filler rod manufacturing

To prepare the ceramic-reinforced tubular filler rods used in the TIG welding deposition, a multi-stage manual fabrication method was employed to ensure consistent powder loading and secure encapsulation. The tubular filler consisted of a predefined length and diameter, with both ends sealed following controlled powder packing. Initially, one end of the tube was hermetically sealed via welding to form a closed container. The tube was then vertically mounted and gradually filled with the desired ceramic powder (either SiC or WC-10%Co). To ensure uniform and maximum filling density, a solid metal rod with a diameter slightly smaller than the inner diameter of the tube was gently inserted and tapped into the cavity, compacting the ceramic powder and minimising voids. This manual compaction method enhanced the stability of the powder column and reduced the risk of segregation during handling.

Once the tube was filled, the open end was also sealed, thus encapsulating the powder completely within the steel sheath. To improve powder retention and enhance mechanical integrity, the sealed tube underwent mechanical compression using a rolling mill machine, which slightly flattened the tubular cross-section. This step served to densify the internal powder column, reduce internal voids, and improve bonding during subsequent TIG welding

deposition. Further technical details and optimization of this filler rod fabrication approach are discussed in Chapter 4.

3.2.1.2 TIG welding

This study employed TIG welding to deposit MMC, offering a controllable and accessible alternative to laser-based deposition methods. A Miller Dynasty 300DX TIG machine, equipped with a 2.4 mm diameter tungsten electrode to generate the arc, was used. The process operates with an estimated energy absorption efficiency of 48% [3.12]. A key component in this setup was the remote foot pedal control, which allowed precise manual current and voltage adjustment. This enabled real time control of the heat input and, consequently, the geometry and stability of the weld pool [3.13]. Unlike semi-automated systems [3.14-3.18], this study used manual approach, allowing precise control over the arc during deposition. Although the current and voltage were manually controlled using a foot pedal during the TIG welding process, the actual values applied during each deposition were recorded. These parameters are detailed and presented in the relevant sections of Chapters 4 and 5, corresponding to each experimental condition.

3.2.1.3 Pin-on-disk sliding wear test

Representative disc samples prepared for dry sliding wear testing are illustrated in Figure 3.1. Figure 3.1a steel disc with a machined central groove, designed to accommodate composite deposition. Figure 3.1b presents the same disc after deposition. Figure 3.1c depicts the same disc sample after surface machining, prior to wear testing. Under dry sliding conditions, the samples were subjected to wear testing using an in-house pin-on-disc tribometer shown in Figure 3.2.

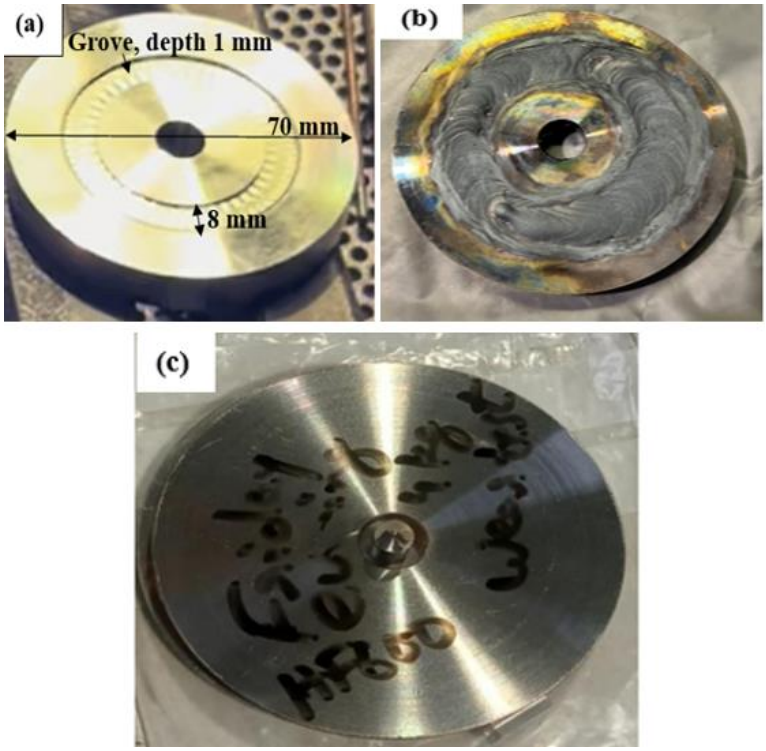

Figure 3.1 Preparation stages of disc samples for wear testing (a) disc with central groove for deposition, (b) after dispositioning, (c) after machining prior to wear testing

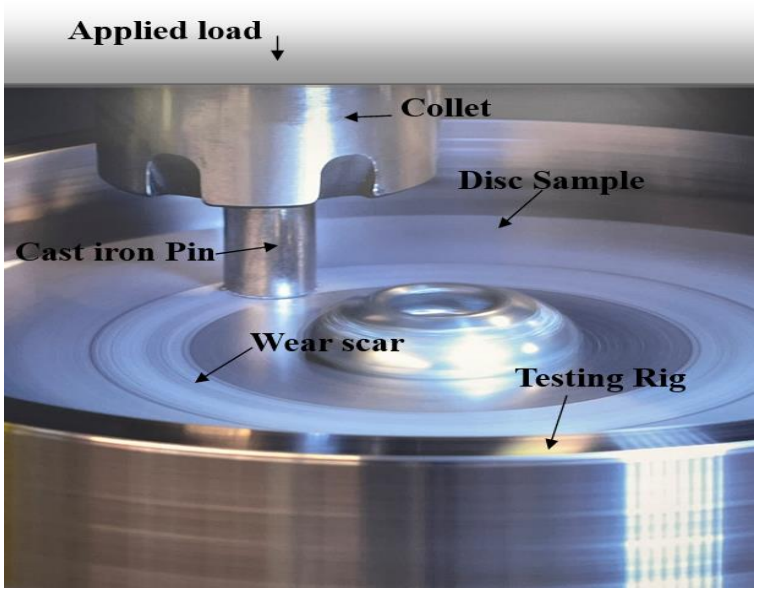

Figure 3.2 Pin on disk testing rig

The wear testing procedure was conducted in accordance with ASTM G99, following these standardised steps:

- The pin and disc contact surfaces were cleaned to remove grease or contaminants.
- The initial mass of each disc sample was measured using an analytical balance with an accuracy of ±0.0001 g.
- The pin and disc were securely mounted in the testing rig.
- The contact surfaces were aligned to maintain perpendicular within ±1°.
- The applied load was set, and the disc's rotational speed was adjusted accordingly.
- The test was initiated and allowed to run continuously without interruption or restarting.
- The test duration was fixed at 3 hours.
- Upon completion, the worn samples were carefully removed.
- The final mass of each sample was measured using the same analytical balance.

Three samples from each material configuration, as outlined in Table 3.6, were fabricated to ensure repeatability, and the corresponding standard deviations were calculated. In all cases, the tubular filler was 316LSS-T. The naming convention used in Table 3.6 follows the format: [Base metal+Reinforcement]. For example:

- 316LSS-BM+SiC refers to a 316L stainless steel base metal disc deposited with a 316LSS-T tubular filler with SiC.
- LCS-BM+WC10%Co refers to a low-carbon steel base metal disc deposited with a 316LSS-T filler with WC-10%Co.
- 316LSS-BM or LCS-BM refers to unreinforced base metal discs.
- 316LSS+HF600 or LCS+HF600 represents base metal discs hard faced using HF600 electrode.

Table 3.6 Description of sample configurations and test combinations used in the pin on disc wear analysis

Number of samples	Disc	Pin	Pin dia (mm)	Load (Kg)	Speed (rpm)	Duration (h)
9	316LSS-BM	CI	6	2,4,6	80	3
9	316LSS-BM+HF600	CI	6	2,4,6	80	3
9	316LSS-BM+SiC	CI	6	2,4,6	80	3
9	316LSS-BM+WC	CI	6	2,4,6	80	3
9	LCS-BM	CI	6	2,4,6	80	3
9	LCS-BM+HF600	CI	6	2,4,6	80	3
9	LCS-BM+SiC	CI	6	2,4,6	80	3
9	LCS-BM+WC	CI	6	2,4,6	80	3

3.2.1.3.1 White cast iron for wearing test

White cast iron (WCI) was used as the counter-body (pin) in the dry sliding pin-on-disc wear tests to assess the wear resistance of the deposited surfaces. Its high hardness and carbide-rich

microstructure provide a consistent and aggressive wear mechanism, making it an ideal material for evaluating the durability of MMC deposits. Table 3.7 shows the chemical composition of WCI. Its microstructure consists of a continuous network of chromium carbides distributed within a pearlitic matrix. In subsequent chapters, the white cast iron pin is called CI pin.

Table 3.7 chemical composition wt% of CI (supplier certificate)

Element	C	Cr	Si	Mn	P	S	Fe
wt%	3.03	27	0.7	1.0	0.03	0.02	Bal.

3.2.2 Sample preparation methods

After deposition, all samples were prepared for metallographic analysis to evaluate their microstructure, hardness, and phase composition. The preparation involved four primary stages: sectioning, mounting, polishing, and etching.

3.2.2.1 Sample sectioning.

Samples designated for metallographic examination were sectioned using an abrasive cutting wheel accompanying on an ATA Brilliant 230 metallographic cut-off saw. The sample was securely held using the machine's integrated vice assembly. A continuous cooling system circulates fluid was applied to prevent thermal accumulation and preserve the specimen's microstructural integrity. This method minimised surface deformation, which was later eliminated during polishing.

3.2.2.2 Mounting

After sectioning, specimens were mounted using an ATA Opal 410 hot mounting press. Each sample was embedded in conductive phenolic resin (Bakelite) under a pressure of 25 MPa at 200°C for 15 minutes, producing a stable and conductive mount for further preparation and analysis.

3.2.2.3 Polishing.

The samples were subjected to sequential grinding and polishing to eliminate surface deformation caused by sectioning and to achieve a high-quality finish suitable for microstructural analysis. The preparation was carried out using a Struers Rotopol-21 system combined with the Rotoforce-5 head. Samples were first mounted in holders and aligned using the Struers Uniforce alignment device to ensure uniform surface preparation. The grinding process began with FEPA P220 grit abrasive paper, followed by progressive polishing using diamond suspensions down to 1 μm, and finally, 0.04 μm colloidal silica for fine polishing. Alcohol was used as the polishing suspension during the diamond stages, except the 1 μm stage. Grinding was conducted under a 120 N force at 300 rpm for 2 minutes, while polishing was performed using the same force at 150 rpm for 2 minutes per stage.

3.2.2.4 Etching

Etching was performed according to guidelines in the ASM Handbook [3.19], using different reagents based on the material type:

- Nital for carbon steel
- 10% Oxalic acid for stainless steel
- Kaling's reagent for HF600

These etchants selectively revealed the microstructural features for optical microscopy.

3.2.3 Analytical approaches

3.2.3.1 Optical microscopy

Following the etching process, all specimens were examined using an Olympus GX-51 inverted optical microscope as shown in Figure 3.3. Polarised light was adjusted under extinction conditions to reveal grain structures and boundaries. Micrographs were captured at magnifications ranging from ×50 to ×1000, enabling detailed analysis of microstructural features.

Figure 3.3. Optical microscope

3.2.3.2 Scanning electron microscope

A Hitachi S-3700 series scanning electron microscope (SEM) as shown in Figure 3.4 was used to investigate the microstructure of the base metals, deposits, electrodes, and ceramic powders. An accelerating voltage of 15 kV was applied to ensure adequate resolution for examining matrix reinforcement interfaces and particle retention.

Figure 3.4 - Hitachi Series S-3700 Scanning Electron Microscope

3.2.3.3 Energy dispersive spectroscopy

Elemental composition was analysed using the SEM integrated with energy dispersive spectroscopy (EDS). During EDS, a high-energy electron beam excites atoms in the sample, and the characteristic X-rays are detected to identify the elements present. This technique allowed for both qualitative and quantitative analysis of the sample composition. These capabilities were essential for confirming the presence and dispersion of SiC and WC particles within the steel matrix.

3.2.3.4 Hardness measurement

Vickers microhardness testing was conducted on all prepared samples using an automated micro indentation testing machine Figure 3.5. A load of 500 grams was applied for each indentation. Line mode tests assessed the hardness distribution across the weld zone, heat affected zone, and base metal. During testing, the machine enables visual comparison of hardness variations and the overall effect of the deposition process. However, the automated system could not target specific points, such as individual undissolved carbide particles. To address this limitation, a manual MVK G1 Vickers hardness tester was used to perform targeted indentations on localised features. This allowed for precise hardness measurement.

Figure 3.5 - Automatic Micro-indentation hardness testing machine

3.2.3.5 X-ray diffractometry (XRD)

As shown in Figure 3.6, a Bruker D8 Advance X-ray diffractometer was used to identify the phase composition of all materials. The Bruker D8 Advance is equipped with Da Vinci geometry and a Cu Kα radiation source (λ = 1.5406 Å). The X-ray tube was operated at 40 kV and 40 mA, with a step size of 0.5 s and an increment of 0.02°, scanning over a 2θ range of 20°–90°.

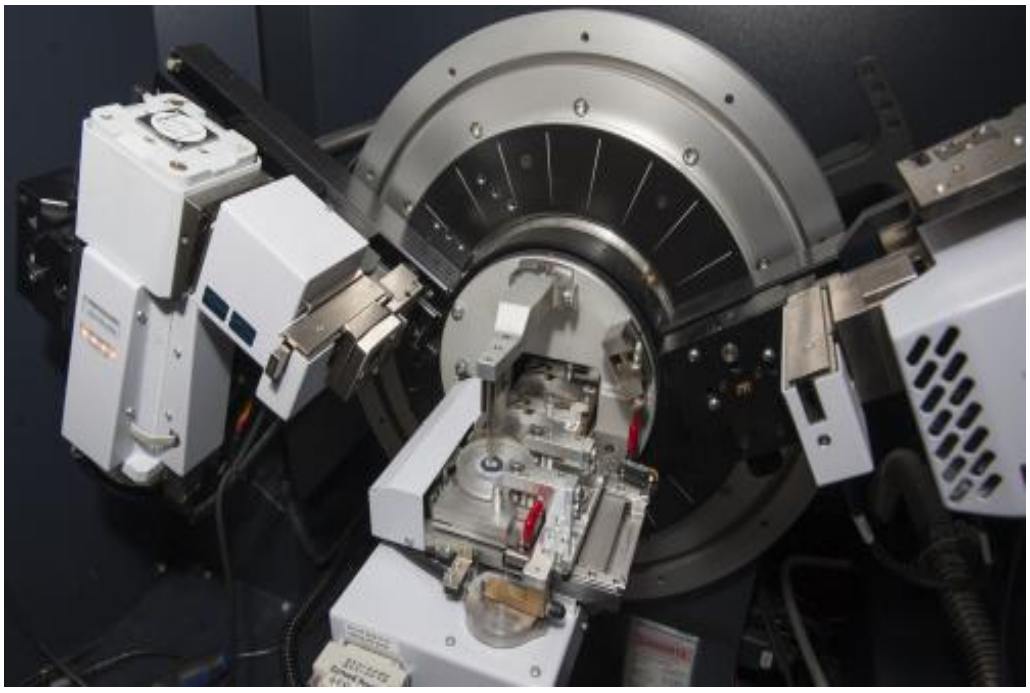

Figure 3.6 - X-Ray Diffractometry (XRD) machine

The instrument generates distinct diffraction patterns, which are compared against a built-in database of known phases. All XRD data were analysed using the ICDD PDF-2 database via the instrument's interface. Phase identification for the powder materials was straightforward, and their diffraction patterns were matched with entries from the JCPDS database. However, this was not the case for the resolidified solid surfaces. This challenge can be attributed to several factors. First, the fusion zone's small size and irregular geometry, combined with the variety of alloying elements and the dissolution of ceramic particles, may result in overlapping or broadened peaks. Second, the beam's limited spatial resolution made isolating specific

regions difficult, such as the interface between FZ and BM. Third, sample positioning and surface preparation errors may have influenced peak clarity.

X-ray diffraction was also performed using a 1 mm beam collimator to mitigate these limitations, as shown in Figure 3.7. This allowed for a more focused spot on the sample surface. The X-ray beam scanned an area of 1 mm in radius, which improved localisation. However, even with this configuration, accurately targeting the interface between FZ and BM remained challenging.

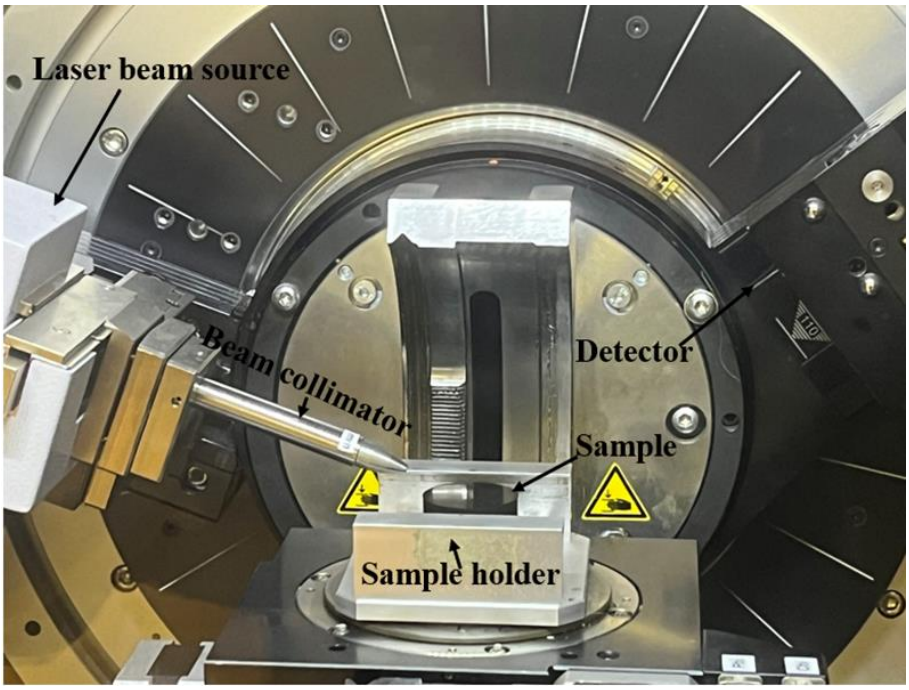

Figure 3.7 - XRD configuration using 1 mm beam collimator including point focus

3.3 References

[3.1] Guo, C., et al., Effects of WC–Ni content on microstructure and wear resistance of laser cladding Ni-based alloys coating. Surface and Coatings Technology, 2012. 206(8-9): p. 2064-2071.

[3.2] Singh, J., L. Thakur, and S. Angra, Abrasive wear behavior of WC-10Co-4Cr cladding deposited by TIG welding process. International Journal of Refractory Metals and Hard Materials, 2020. 88.

[3.3] Khan, M., M.W. Dewan, and M.Z. Sarkar, Effects of welding technique, filler metal and post-weld heat treatment on stainless steel and mild steel dissimilar welding joint. Journal of Manufacturing Processes, 2021. 64: p. 1307-1321.

[3.4] Liang, R., et al., Effect of line energy density in repairing 34CrNiMo6 steel by electron beam remelting. Journal of Manufacturing Processes, 2022. 79: p. 314-325.

[3.5] Zhang, W., Tribology of SiC ceramics under lubrication: Features, developments, and perspectives. Current Opinion in Solid State and Materials Science, 2022. 26(4).

[3.6] Majumdar, J.D., et al., Laser composite surfacing of stainless steel with SiC. physica status solidi (a), 2006. 203(9): p. 2260-2265.

[3.7] Dutta Majumdar, J., et al., Studies on compositionally graded silicon carbide dispersed composite surface on mild steel developed by laser surface cladding. Journal of Materials Processing Technology, 2008. 203(1-3): p. 505-512.

[3.8] Rams, J., et al., Al/SiC composite coatings of steels by thermal spraying. Materials Letters, 2008. 62(14): p. 2114-2117.

[3.9] Konyashin, I., et al., Strengthening zones in the Co matrix of WC–Co cemented carbides. Scripta Materialia, 2014. 83: p. 17-20.

[3.10] Wang, Y., et al., Microstructure and property of tungsten carbide particulate reinforced wear resistant coating by TIG cladding. International Journal of Refractory Metals and Hard Materials, 2021. 100.

[3.11] Huang, S.W., M. Samandi, and M. Brandt, Abrasive wear performance and microstructure of laser clad WC/Ni layers. Wear, 2004. 256(11-12): p. 1095-1105.

[3.12] Lomovsky, O.I., et al., Laser-induced reaction of Si powder with a steel substrate. Inorganic Materials, 2012. 48(3): p. 263-266.

[3.13] Patel, N.S. and R.B. Patel, A review on parametric optimization of TIG welding. International Journal of Computational Engineering Research, 2014. 4(1): p. 27-31.

[3.14] Kumar, A., R. Kumar Ram, and A. Kumar Das, Mechanical characteristics of Ti-SiC metal matrix composite coating on AISI 304 steel by gas tungsten arc (GTA) coating process. Materials Today: Proceedings, 2019. 17: p. 111-117.

[3.15] Sahoo, C.K. and M. Masanta, Microstructure and mechanical properties of TiC-Ni coating on AISI304 steel produced by TIG cladding process. Journal of Materials Processing Technology, 2017. 240: p. 126-137.

[3.16] Sahoo, C.K., L. Soni, and M. Masanta, Evaluation of microstructure and mechanical properties of TiC/TiC-steel composite coating produced by gas tungsten arc (GTA) coating process. Surface and Coatings Technology, 2016. 307: p. 17-27.

[3.17] Sekhar, B.R., et al., Wear characteristic of TiC coated AISI 1020 mild steel fabricated by TIG cladding method. Materials Today: Proceedings, 2020. 26: p. 3288-3291.

[3.18] Sharma, D., et al., Surface modification of microalloyed steel by silicon carbide reinforcement using tungsten inert gas arcing. Materials Research Express, 2018. 6(3).

[3.19] Petzow, G., Metallographic etching: techniques for metallography, ceramography, plastography. 1999: ASM international.

Chapter 4 Optimisation of filler composition and geometry for MMC deposition via TIG

4.1 Introduction

A body of academic research has been conducted to understand and manage the tribological behaviour of materials subjected to sliding contact [4.1-4.5]. In recent years, TIG welding has gathered significant academic interest due to its potential applications in enhancing the wear resistance of metallic surfaces [4.6]. Consequently, depositing hard ceramic particles onto the surfaces of worn steel components offers, not only the possibility of repairing wear-induced damage, but also extending service life by increasing the hardness and wear resistance of the repaired areas.

Recent TIG studies have largely relied on the preplaced powder method [4.7–4.13], which, while effective in improving surface properties [4.8, 4.12, 4.14–4.20], often requires high heat input, leading to reinforcement dissolution and brittle phase formation [4.21–4.25]. These issues are influenced by physical and chemical material properties [4.26–4.29]. In contrast, tubular fillers offer improved control over particle retention, showing strong potential for embedding hard ceramics within the steel matrix. On the other hand, the influence of processing parameters was experimentally optimised during this research to achieve the most effective deposition conditions. An experimental investigation was conducted to determine the optimal filler material, filler size, powder content, and processing parameters.

A progressive series of materials configurations was explored to identify the optimum material composition for MMC deposition. The following combination of tubular filler materials and ceramic reinforcements were tested:

- MCS-T filler with SiC deposited on LCS-BM (section 4.2)
- LCS-T filler with SiC deposited on LCS-BM (section 4.3)
- LCS-T filler with SiC10%Ni deposited on LCS-BM (section 4.4)

- LCS-T filler with WC10%Co deposited on LCS-BM (section 4.5)
- 304LSS-T filler with SiC deposited on LCS-BM (section 4.6)
- 316LSS-T filler with SiC deposited on LCS-BM (section 4.7)
- 316LSS-T filler with WC10%Co deposited on LCS-BM (section 4.8)
- HF600 hard facing electrode deposited on LCS-BM (section 4.9 used as a commercial benchmark)

The results obtained from varying material compositions and processing conditions were systematically evaluated. Microstructural and chemical analyses of the specimens were performed using optical microscopy, SEM, with EDS, and XRD. Additionally, microhardness measurements were conducted across the cross-section of the samples. Based on the optimised processing parameters, the most suitable filler material with appropriate dimensions was selected for further assessed for its reliability in the deposition of MMC for the final wear assessment (chapter5).

4.2 Evaluation of MCS-T filler with SiC particles deposited on LCS-BM

4.2.1 Experimental procedure

The first stage of the study involved selecting an overmatching filler material to investigate the effect of carbon content on the LCS-BM with a carbon content of 0.1%. Consequently, a MCS-T filler, with a carbon content of 0.37%, was used. The chemical composition of the LCS-BM and the MCS-T are detailed in Chapter 3, (Section 3.1.2.1), and Section (3.1.3.1) respectively. The MCS-T filler was fabricated with an OD of 4 mm and an ID of 3 mm. It was internally packed with SiC powder and sealed at both ends.

The size, shape, and chemical composition of the SiC powder is detailed in Chapter 3, (Section 3.1.4.1). Prior to the deposition process, the substrate surface was abraded using 220-grit paper and subsequently cleaned with acetone to eliminate contaminants and ensure proper adhesion.

Figure 4.1 provides a schematic diagram illustrating the deposition process and a cross-sectional view of the cored filler. A Miller TIG torch equipped with a 2.5 mm diameter tungsten electrode was used to establish the arc between the electrode tip and the specimen surface, ensuring stable and controlled deposition conditions.

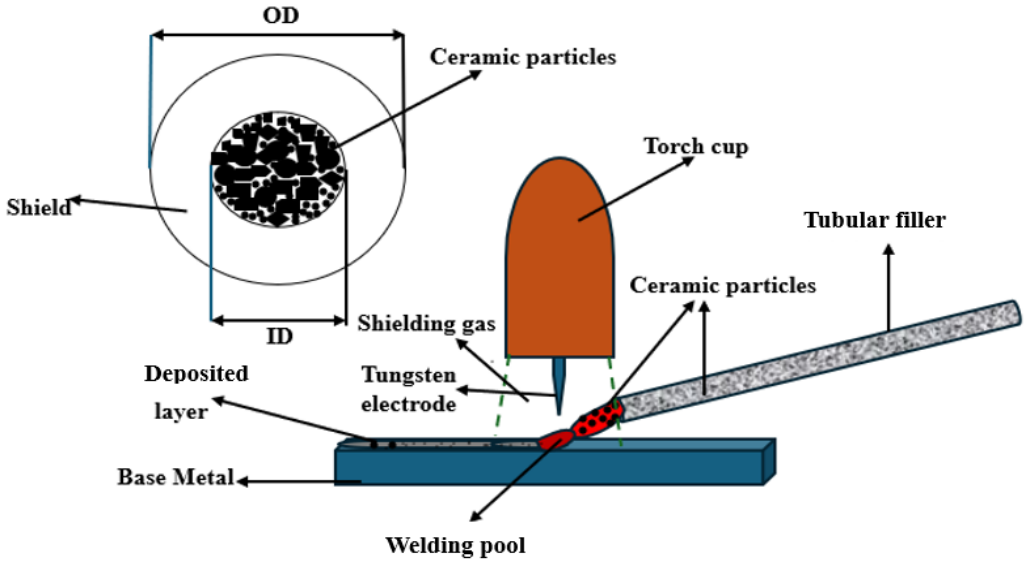

Figure 4.1. Schematic diagram of the deposition process

The maximum direct operating current was 200 A (DCEN). The arc was initiated at electrode heights of 1 mm to 3 mm. To prevent the molten pool from oxidising, argon shielding gas was supplied at a flow rate of 10 L/min. The current and voltage frequencies were regulated to control the formation of the molten pool and the transfer of liquid droplets from the filler. During the welding process, a foot pedal was used to dynamically adjust the current and voltage. The current was maintained within the 175–200 A range, while the voltage varied between 11 and 16 V. The torch travel speed was controlled manually to ensure consistent deposition and fusion.

A single weld bead was deposited, and the specimen was allowed to cool naturally to room temperature. As described in Chapter 3, the standard specimen preparation procedure was

followed for metallographic and microhardness examination. A prepared hardness tested sample is illustrated in Figure 4.2.

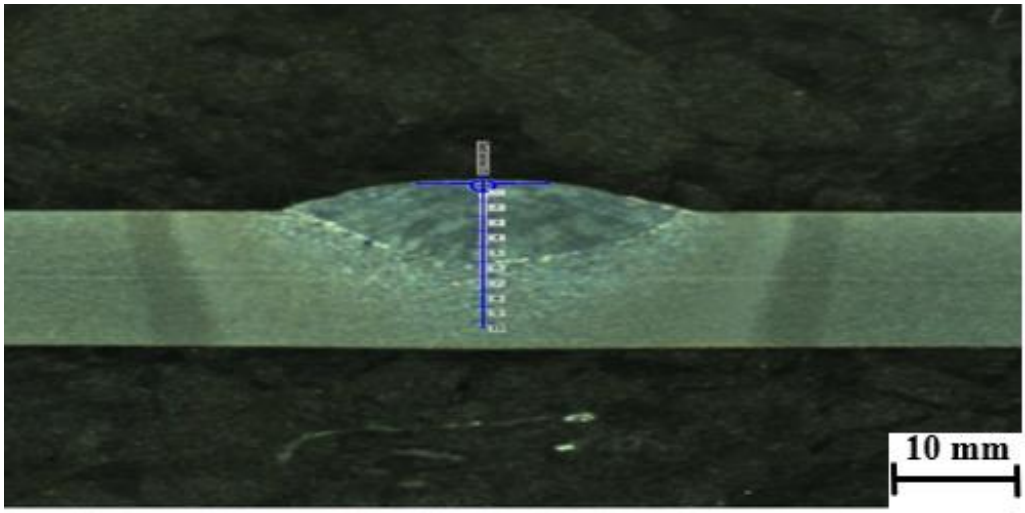

Figure 4.2 The cross section of a prepared sample for metallographic and microhardness examination

4.2.2 Results and discussion

4.2.2.1 Microstructure

Microstructural analysis was conducted using an optical microscope after etching, the examined area was divided into the following zones: base metal (BM), heat-affected zone (HAZ), interface (IF), and fusion zone (FZ), as illustrated in Figure 4.3a. Figure 4.3b, and 4.3c represent the FZ near the IF.

It can be observed that the LCS-BM, SiC powder, and MCS-T underwent melting and mixing during their liquation state, with most components dissolving and recrystallising into a new morphology upon solidification. The presence of C and Si in the FZ contributed to a microstructure characterised by needle-like martensite and graphite formations. Furthermore, the MCS-T's high C content and any dissolved SiC particles resulted in an increased C and Si concentration in the FZ. Steel containing more than 0.4% C and high Si content is particularly susceptible to rapid cooling rates, leading to martensitic transformation and an increased risk of cracks upon solidification [4.30, 4.31].

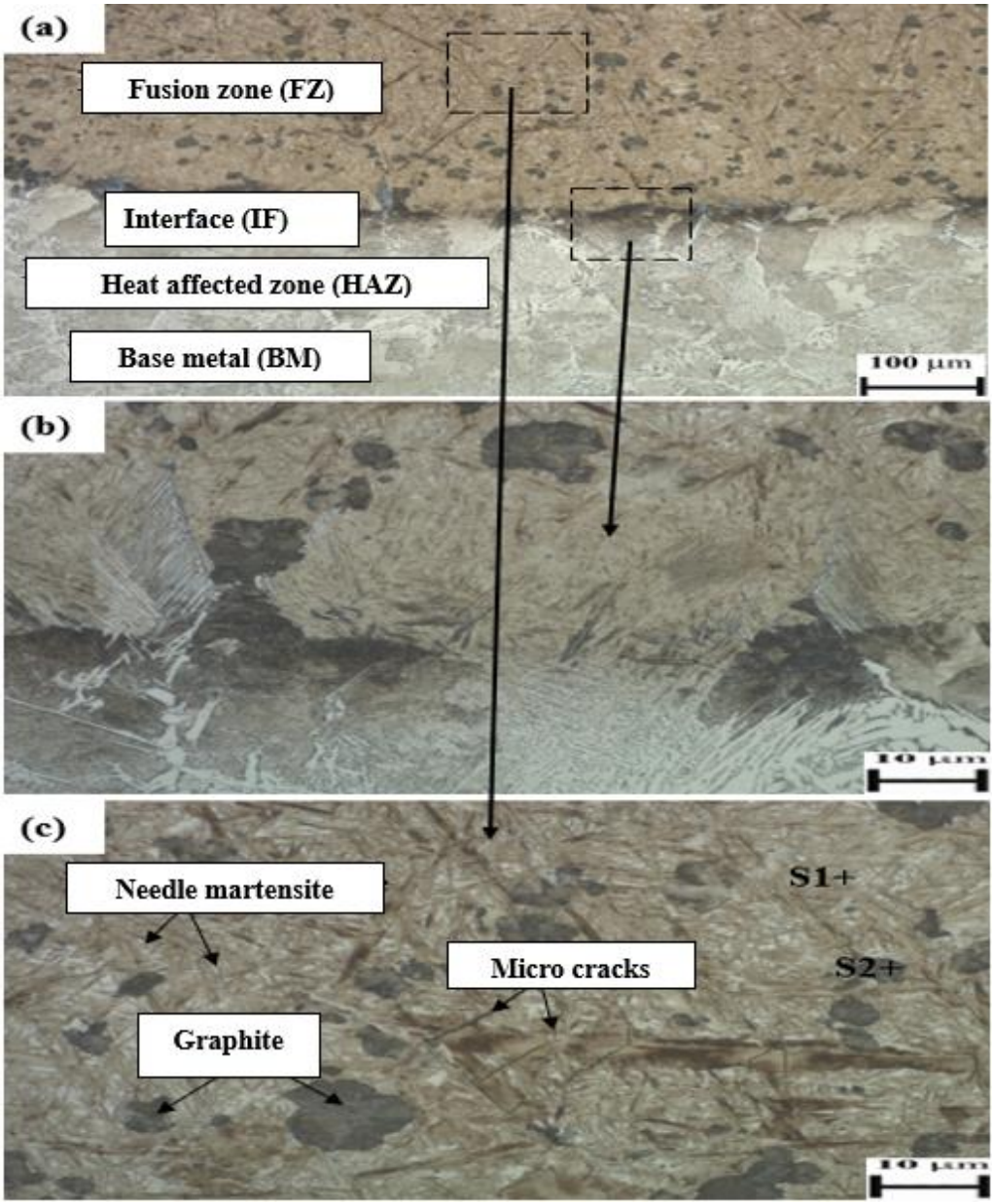

Figure 4.3. The microstructural characterisation under the optical microscope, (a) represents the FZ, IF, HAZ, and BM. (b) represents a higher magnification near the IF, (C) with a higher magnification of the FZ

Figure 4.4a presents the microstructure of the transverse section of the SiC layer deposited using the MCS-T filler. It can be observed that the tubular electrode in this sample had a higher powder content relative to the discharged droplet from the filler, attributed to its 4 mm ID and 1 mm wall thickness. As a result, the liquid droplets discharged from the filler contained a greater concentration of SiC powder. During the feeding process, the shielding gas flow

influenced the SiC powder, with some particles trapped within the molten pool as shown in Figure 4.4b, while others were displaced. However, microstructural analysis revealed that the SiC powder did not fully incorporate in the molten pool, with some SiC particles dissolving and diffused into the solidified zone. However, the primary mechanism behind the observed phase transformations, specifically the formation of graphite and martensite, is attributed to the dissolution of SiC particles during processing. Once dissociated, the released Si and C atoms diffuse into the steel matrix, where they actively alter the microstructure, developing these new phases [4.8, 4.10-4.12].

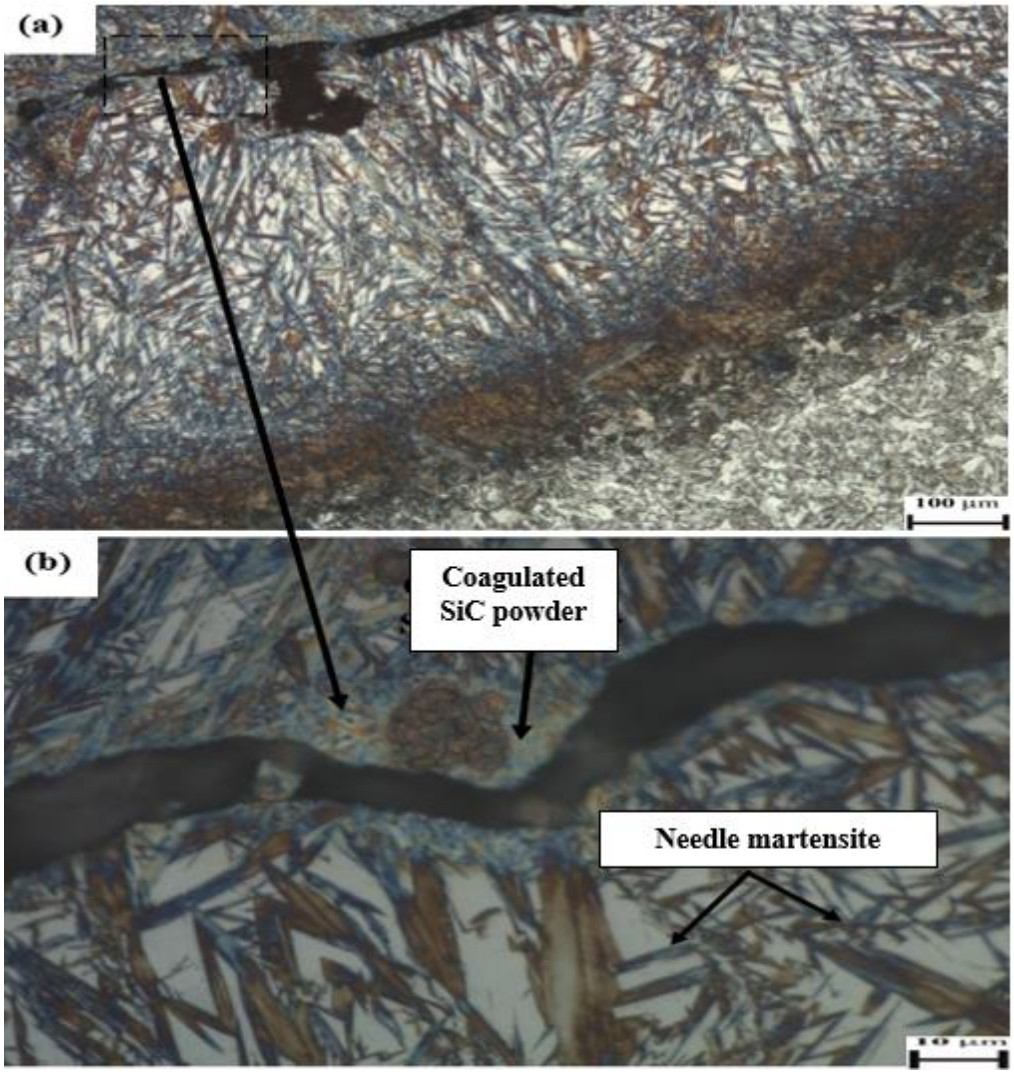

Figure 4.4 Optical micrograph of the transverse microsection of SiC Layer (a) surface view of FZ, interface, and HAZ (b) higher magnification showing the voids of trapped SiC inside FZ and the needle martensite transformation

4.2.2.2 Chemical composition

For the chemical analysis, the EDS data presented in Figure 4.5 correspond to the positions marked in Figure 4.3c. Spectrum 1 exhibits an increase in C and Si content compared to the base metal and filler composition. The elevated Si content indicates that SiC particles were successfully diffused into the deposited layer. However, Spectrum 2 reveals even higher C and Si concentrations than Spectrum 1. This position is associated with the presence of a spherical particles, which assumed to be a graphite [4.32]. At this location, the Fe concentration decreased from 92 wt% to 89.42 wt%, indicating localised enrichment of C content [4.31, 4.33, 4.34]. In the absence of significant Si content in liquid Fe, the dissolution of SiC leads to graphite saturation before the complete dissolution of SiC occurs. This behaviour is well documented within Fe-Si-C alloy systems [4.31, 4.34-4.37].

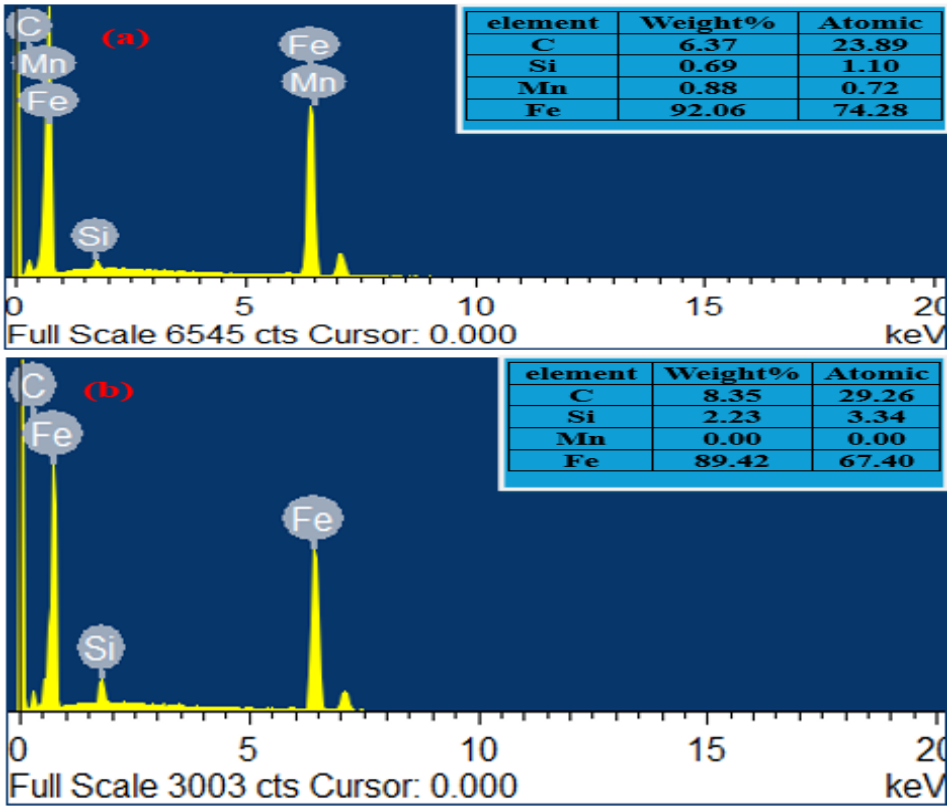

Figure 4.5. Chemical composition obtained by EDS of the FZ points outlined in Figure 4.3C, (a) S1+ and (b) S2+

4.2.2.3 Microhardness

As expected, the FZ's microstructure, which contains graphite along with elevated C and Si content, exhibited higher hardness values compared to the BM as shown in Figure 4.6. The maximum hardness recorded in the FZ was approximately 769 Hv. However, hardness values gradually decreased to 240 Hv in the HAZ at a depth of 2.5 mm from the surface. Beyond this point, the hardness further declined, nearly returning to the BM hardness of approximately 180 Hv.

However, cracks and voids were prominently observed within the melting zone, likely due to the high C content and the rapid cooling rate. Despite these defects, the microhardness of the deposited layer increased significantly compared to the BM.

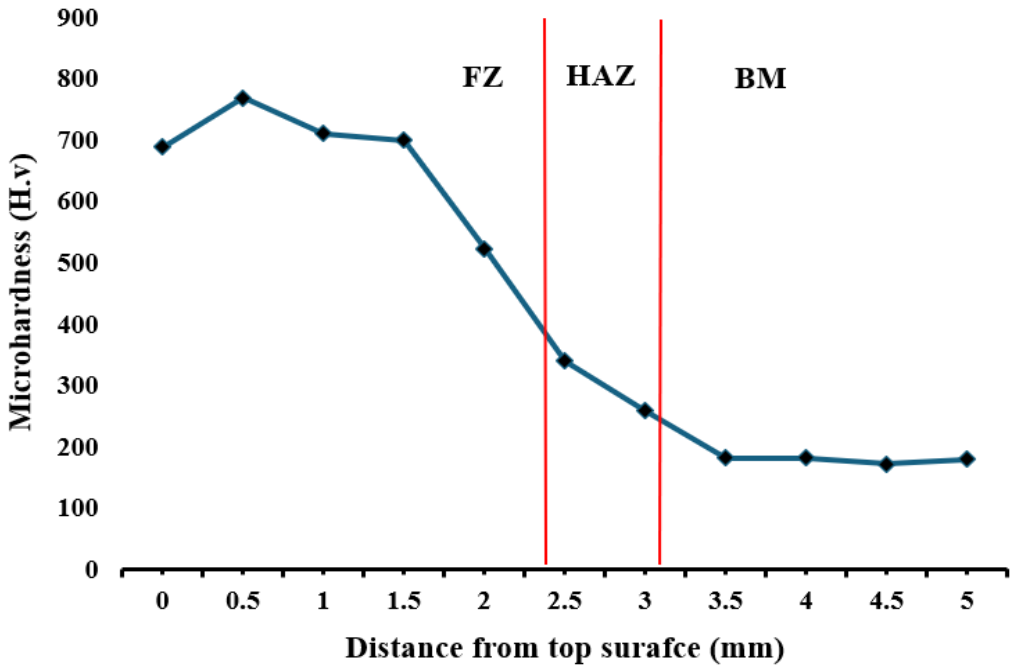

Figure 4.6. Vickers microhardness measurement of the SiC and MCS-T filler as a function of distance from the top surface

4.2.3 Filler evaluation and development

During the deposition process, as the substrate surface melted and the electrode was positioned vertically at the edge of the molten pool, the molten droplets successfully merged into the molten pool. However, due to gravity and the low density of SiC powder, a significant portion

of the ceramic particles failed to be entered into the weld pool and were dispersed by the shielding gas flow. To overcome these challenges, the modified tubular filler was developed by compressing the filler using a roller milling machine. Figure 4.7 presents the compressed cored filler's cross-sectional view. This approach crushed and embedded the hard ceramic particles inside the tubular filler, creating a densely packed filler tube containing ceramic particles. However, the MCS-T filler electrode proved to be unsuitable due to its high C content and the presence of Si. This composition led to undesirable microstructural transformations and hindered the effective retention of ceramic particles in the weld pool. Based on these findings, MCS-T fillers were deemed unsuitable, and LCS-T filler with no Si content and a reduced C concentration were fabricated for further analysis.

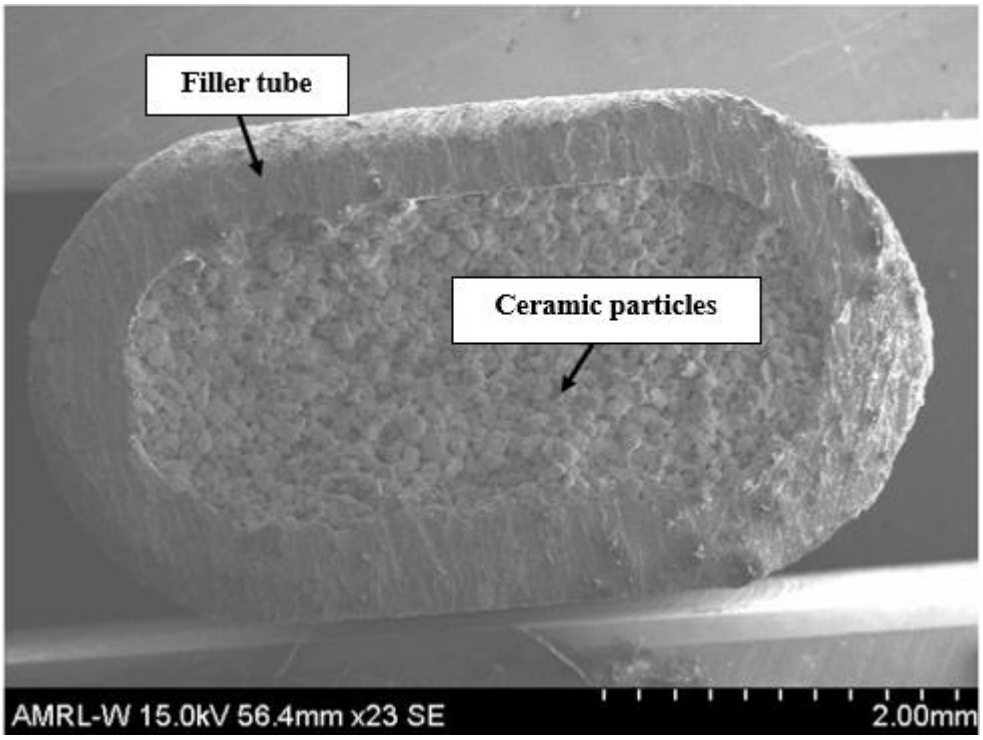

Figure 4.7. cross section of the developed ceramic material- infused electrode containing ceramic particles after compression by roller milling machine

4.3 Evaluation of LCS-T filler with SiC particles deposited on LCS-BM

4.3.1 Experimental procedure

A LCS-BM and LCS-T filler with characteristics detailed in Chapter 3, (Section 3.1.3.1) were chosen. LCS-T fillers were manufactured with various OD and ID, as listed in Table 4.1, and subsequently filled with SiC powder, sealed, and compressed. The experimental procedure and preparation were as in the previous section as for all stages except for current and voltage. In this stage, the operating current was at 175–200 A with a voltage range of 11–16 V.

Table 4.1 Filler tube details (LCS-T)

Sample	Tube-filler material	OD in mm	ID mm in mm	Powder
T1	LCS	5	4	SiC
T2	LCS	5	3	SiC
T3	LCS	5	2.5	SiC

4.3.2 Results and Discussion

4.3.2.1 Microstructure and Composition

Figure 4.8a presents the microstructure of sample T1 and revealed that the SiC particles were completely dissolved. According to the Fe-Si-C phase diagram, SiC reacts rapidly with liquid Fe [38]. Since both the LCS-BM and the LCS-T filler share the same chemical composition, the FZ exhibited a high concentration of Fe as steel matrix, in addition to the Si dissolved from the SiC powder. These elements reacted during solidification, leading to the formation of a graphite structure. Additionally, the high cooling rate and localised regions of elevated C and Fe content in the FZ facilitated the transformation of needle-like martensite, as shown in Figure 4.8b.

The microstructure of T2, presented in Figure 4.9a, was characterised by very fine-grained ferrite growing in a columnar fashion, with a bainitic phase transformation occurring across the austenite boundaries during solidification. The C distribution in the FZ was uneven, with localised regions exhibiting cast iron-like cellular structures. Notably, the IF exhibited a strong metallurgical bonding, with no visible line fusion (No sharp transition). In Figure 4.9b, the

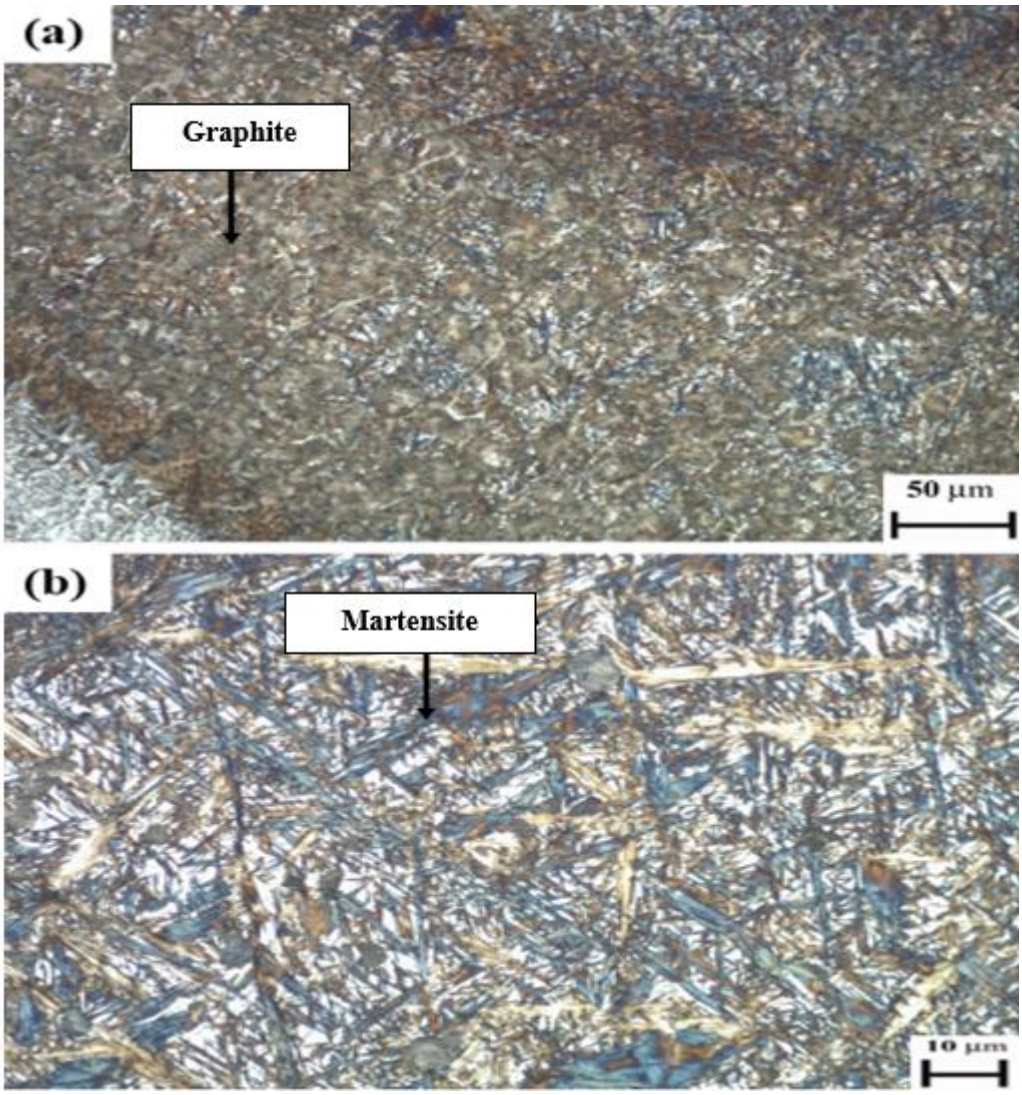

Figure 4.8. The microstructure of T1, (a) shows the transformed graphite phase and the martensitic transformation during solidification due to high content of C and Si, and (b) needle martensite phase

microstructure comprises ferrite, martensite, and retained austenite, forming a structure that can be categorised as lower bainite. Lower and upper bainite are characterised by irregular ferrite grains, with C rich secondary phases dispersed between the ferrite grains [4.39-4.42].

Figure 4.10 illustrates the microstructure of (T3) deposited layer. The IF between the FZ and the BM exhibited good metallurgical bonding, as shown in Fig 4.10a, with no visible fusion line. Compared this weld deposit with other weld deposits processed by other tubular filler dimensions, this configuration proved to be the most optimal for bonding quality and structural

integrity. In Figure 4.10b, partially dissolved SiC particles were retained within the composite, likely due to the thicker tube wall shielding the powder from direct arc exposure and minimising excessive dissolution.

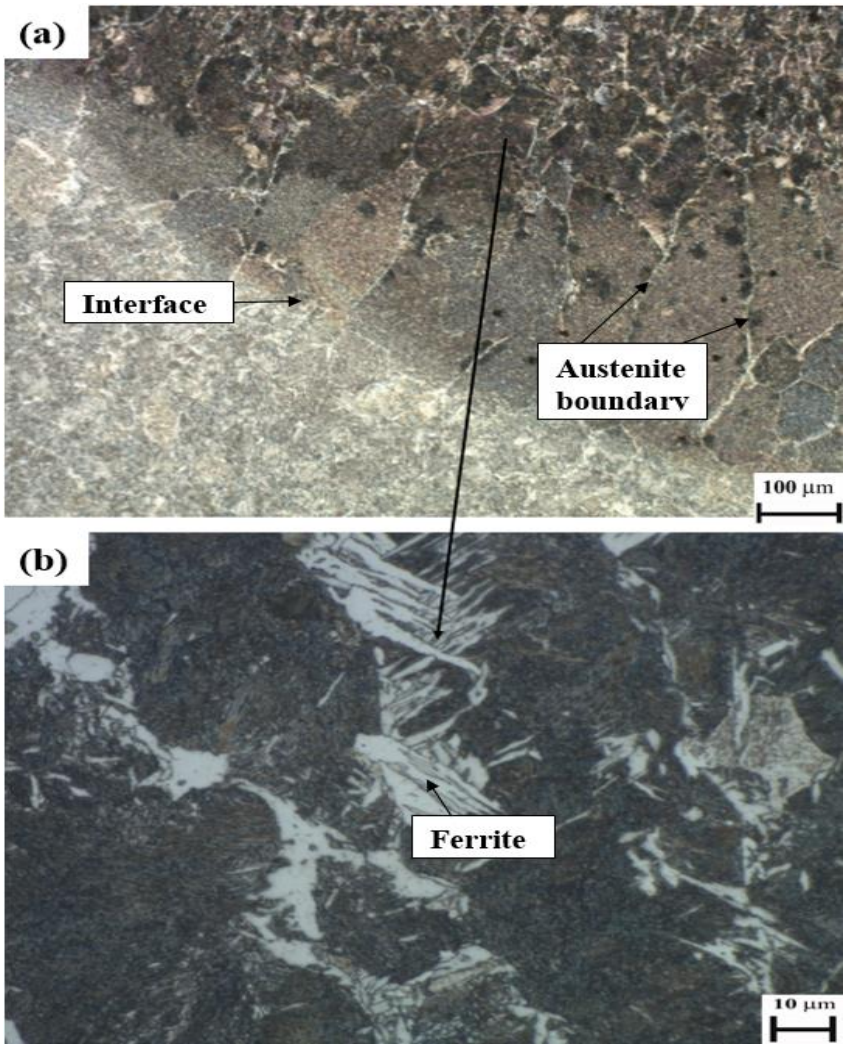

Figure 4.9. microstructure of T2, (a) represents the IF (b), a higher magnification of the FZ, shows a bainitic and ferritic phase transformation across the austenite boundary during solidification

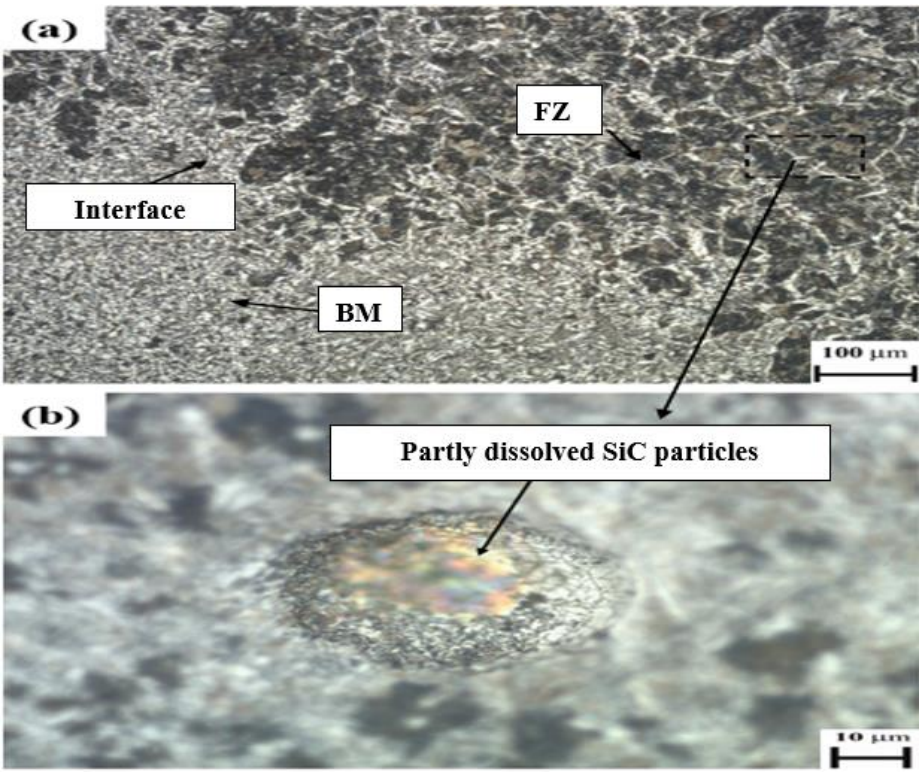

Figure 4.10. Microstructure of T3, (a) shows the IF and the absence of the line fusion between the BM and FZ, (b) a higher magnification of partly dissolved and retained SiC particles which stand out in relive above the soft metal matrix after grinding and polishing

In Figure 4.11, the XRD spectra of T1, T2, and T3 were compared with those of SiC powder, BM, and tubular filler. The spectra from the BM and tubular filler exhibited peaks corresponding only to ferrite and cementite Fe_3C, with no detectable SiC phase in T1, T2, or T3. This absence of a SiC phase confirms that the SiC particles were wholly dissolved and precipitated in a new morphology. However, optical microscopy analysis revealed retained SiC particles in T3, suggesting a low volume fraction of these partially dissolved particles remained. Due to their small quantity, no distinct peaks were detected in the XRD spectra. In T1, which contained a high concentration of SiC powder, peaks corresponding to martensite were identified. The formation of martensite was attributed to the high C content released from the dissolution of SiC and the rapid solidification rate characteristic of the TIG welding

process. Additionally, in T2, an iron-silicon phase Fe_3Si was formed, indicating the diffusion and interaction of Si with the Fe matrix during solidification.

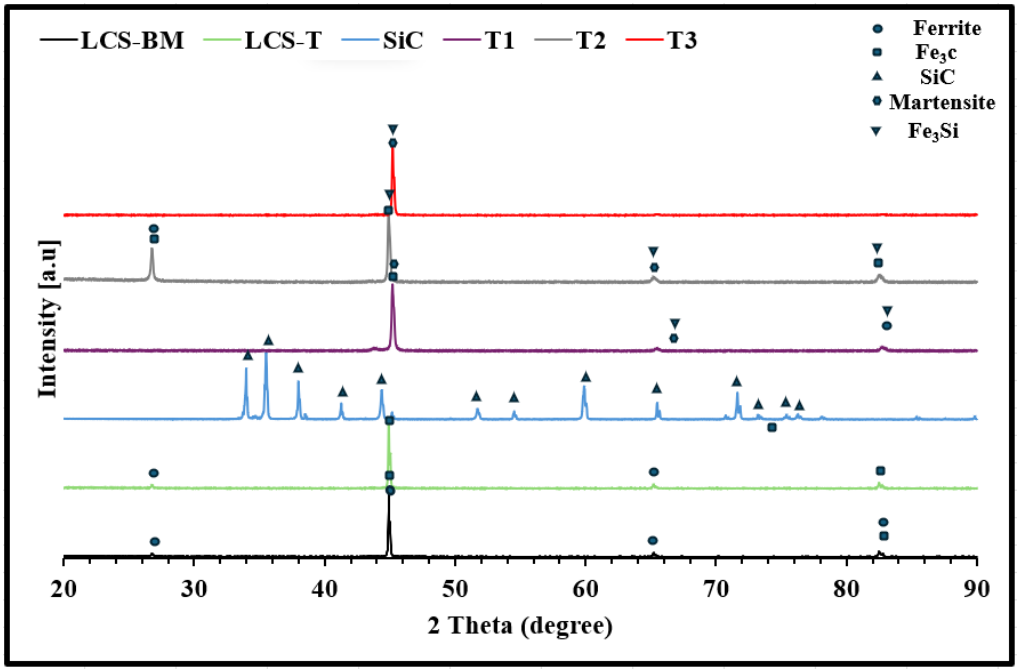

Figure 4.11. XRD spectra of T1, T2, T3, SiC powder, BM and Tube Filler

4.3.2.2 Microhardness

Figure 4.12 presents the microhardness measurements of the three tested samples. T1, processed with a 3 mm ID, exhibited complete dissolution of SiC, resulting in a maximum recorded microhardness of approximately 754 HV. The hardness varied from the top surface of the FZ toward the BM, with the highest reading observed at a depth of 1.75 mm. At 2.2 mm, it decreased to 625 HV before reaching the BM hardness of 180 HV. These variations were expected due to the presence of martensite and graphite, forming a microstructure resembling cast iron [4.38, 4.43].

T2 recorded a maximum hardness of 507 HV at a depth of 1.5 mm. This specimen exhibited the lowest microhardness among the tested samples, attributed to its bainitic, and ferritic microstructure. In this case, the SiC particles were not fully incorporated into the FZ, reducing hardness. T3 displayed the highest microhardness, with a peak value of approximately 815 HV at a depth of 1.5 mm. This increase in hardness was attributed to the presence of partially

melted SiC particles. Additionally, at depths of 1.75 mm and 2 mm, the hardness remained within the 800 HV range, further confirming the influence of retained SiC particles on the mechanical properties of the deposited layer. The variation in hardness between T1, T2, and T3 is attributed to the variation of tubular filler dimensions.

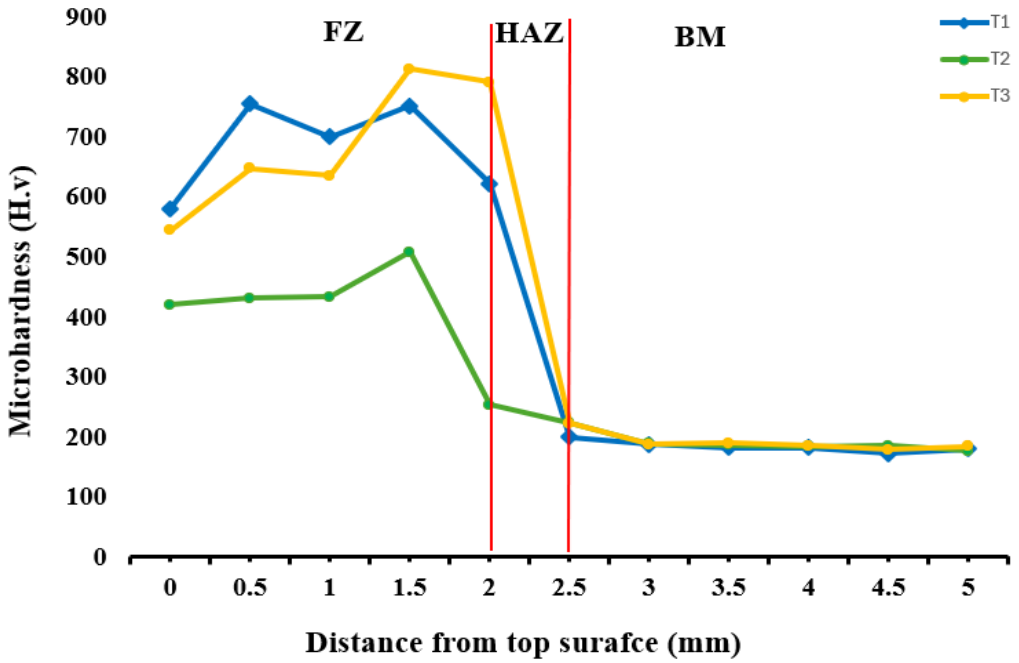

Figure 4.12. The line microhardness profile of the cross-sectional area of three series tested specimens

The investigation into using LCS-T fillers with SiC particles on a LCS-BM demonstrated significant variations in microstructural development and mechanical properties, particularly microhardness. The findings confirmed that SiC particles were fully dissolved in most cases, leading to a notable increase in hardness due to the formation of graphite, martensite, and bainite structures. However, the degree of SiC retention and dissolution varied depending on the tubular filler dimensions, which directly influenced the deposited layer's hardness and overall microstructure.

The study highlights the importance of optimising tubular filler dimensions to balance the dissolution and retention of ceramic reinforcements, ensuring enhanced mechanical properties and metallurgical bonding. Future work should focus on improving SiC retention, controlling

phase transformations, and fine-tuning welding parameters to enhance the performance of SiC-reinforced MMC layers further. The next phase of this study will focus on adding nickel Ni to SiC to further minimise the dissolution of SiC particles and enhance their retention within the weld pool.

4.4 Evaluation of LCS-T filler with SiC10%Ni deposited on LCS-BM

Several studies have explored using metallic binders such as Ni to mitigate the dissolution behaviour of SiC in iron-based matrices [4.11, 4.12, 4.38]. However, these studies primarily employed the preplaced powder method, which as previously discussed, presents several drawbacks. The present study aims to evaluate whether the addition of Ni can effectively stabilise SiC particles in the TIG welding process, ensuring better retention and improved wear resistance in the deposited MMC's by utilising a LCS-T filler containing SiC10%Ni.

Ni is a well-known austenite stabiliser that extends the austenite phase region and reduces the solidification rate. In cladding and coating using composite materials, Ni is frequently added to carbides to improve crack resistance [4.45]. Ni and Fe exhibit excellent metallurgical compatibility, making Ni a suitable additive for iron-based systems [4.46]. Given these advantages, incorporating Ni into SiC powder through this novel powder feeding system presents a promising approach to enhancing SiC particle retention, reducing dissolution, and improving the mechanical performance of the deposited MMC. Therefore, investigating the effect of Ni addition to SiC powder in this study is essential for optimising TIG welding-based MMC's deposition technique.

4.4.1 Experimental Procedure

LCS-T Filler wires were manufactured, filled with SiC-10%Ni, and compressed. During the deposition process, the current ranged between 175 and 200 A, while the voltage varied from 11 to 16 V.

4.4.2 Results and Discussion

The substrate surface was melted during the deposition process, and the filler was inserted in the edge, allowing it to melt and release detached droplets into the molten pool. As a result, the elemental compositions of the BM and filler mixed within the molten pool. Once the arc advanced forward, the molten pool solidified, initiating grain nucleation and growth. Iron, inherently ferritic at temperatures below its melting point, transformed into austenite as cooling progressed. Given the fast-cooling rate associated with the TIG process, the microstructure in previous samples was typically transformed into graphite and martensite. However, as shown in Figure 4.13, adding Ni extended the austenite phase region, effectively suppressing martensitic transformation. This observation suggests that Ni influences the final microstructural development by promoting a more ductile phase composition than previous samples.

As a result, the microstructure primarily consisted of retained austenite, within which idiomorphic ferrite nucleated inside the austenite grains, while allotriomorphic ferrite grew along the grain boundaries. However, despite the presence of Ni, the SiC powder was not effectively protected from dissolution, aligning with findings from previous studies [4.38, 4.47, 4.48] that utilised the preplaced powder method. Given this outcome, no further analysis was conducted on this.

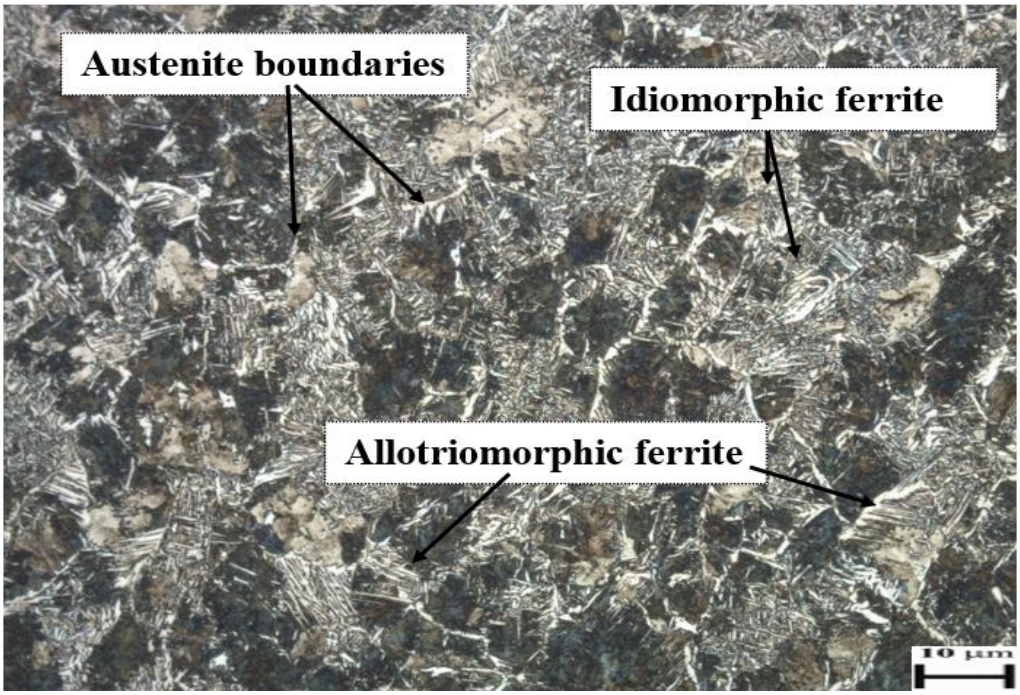

Figure 4.13. Represents a higher magnification of the FZ which consists of retained austenite, idiomorphic ferrite and allotriomorphic ferrite

4.5 Evaluation of LCS-T filler with WC-10%Co deposited on LCS-BM

4.5.1 Experimental procedure

A LCS base metal was selected, and LCS-T tubular fillers were manufactured as listed in Table 4.2 and filled with WC-10%Co ceramic powder. The size, shape, and chemical composition of the WC-10%Co powder are provided in Chapter 3, (Section 3.2.6). In this stage, the operating current was at 180–200 A with a voltage range of 12–16 V. Specimen preparation followed the procedure described in the previous section, ensuring consistency in surface treatment, deposition, and testing methodologies.

Table 4.2 Filler tube details (LCS-T)

Sample	Tube filler material	OD in mm	ID in mm	Powder
T1	LCS	5	4	WC10%Co
T2	LCS	5	3	WC10%Co
T3	LCS	5	2.5	WC10%Co

4.5.2 Results and Discussion

4.5.2.1 Microstructure and Chemical Composition

Figure 4.14 presents the main zones observed: the FZ, IF, HAZ, and BM. A defect-free deposited layer was successfully achieved through TIG welding process. Within the HAZ, the microstructure of the BM underwent phase transformation and refinement due to the heat input observed from welding. There was minimal atomic segregation at the interface between the BM and the FZ, in contrast to the SiC-based samples. A fusion line (sharp transition) was formed between the FZ and the BM, likely due to the high density of tungsten particles, which penetrated deeper into the liquid phase. The good wettability of W with Fe [49-51] may have further restricted the segregation of Fe atoms between the BM and the FZ.

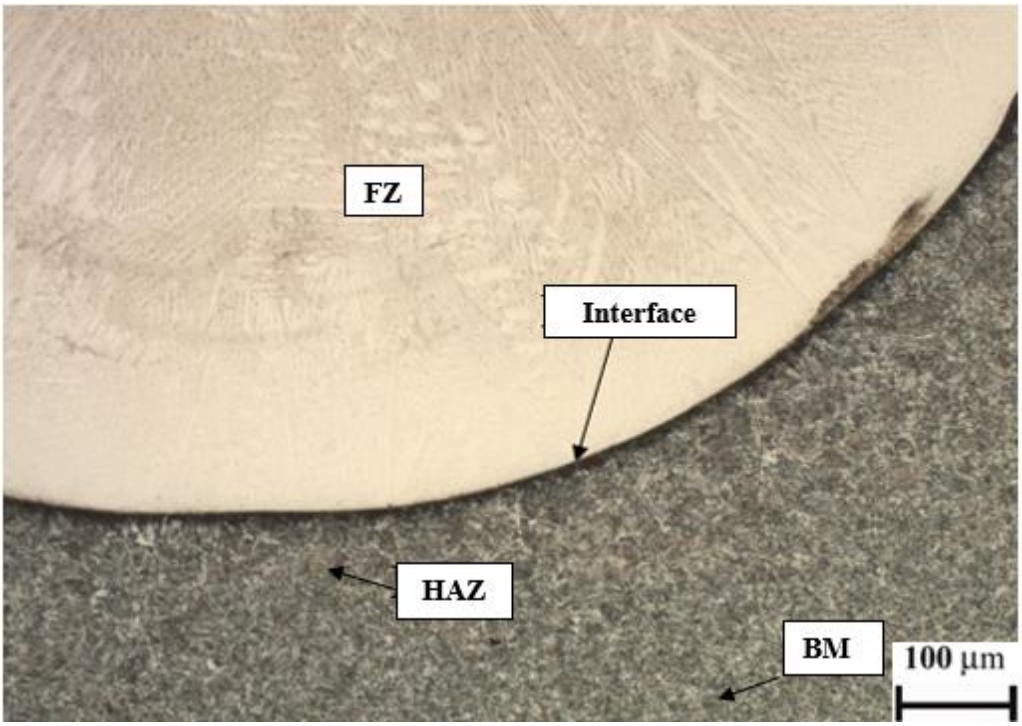

Figure 4.14. Micrograph of LCS/WC10%Co weld joint highlighting FZ, IF, HAZ, and BM

The diffusion behaviour observed in this study highlights that Si tends to migrate from the FZ toward the BM across the HAZ. This phenomenon is attributed to the high mobility of Si in

Fe, which is primarily temperature driven. In contrast, tungsten exhibited minimal segregation, likely due to its low diffusion rate and strong atomic bonding within the matrix.

The growth of the Fe matrix is significantly influenced by the solidification conditions during the TIG melting process. Dendritic growth occurs at the bottom of the molten pool, where the temperature gradient is high, and the solidification rate is low. Due to the supercooling effect in the TIG process and the high Fe content, the formation of Fe-rich dendrites was initiated. Additionally, the C content from the BM, filler, and dissolved WC particles diffused into the dendritic structure, resulting in a supersaturated solid solution upon solidification. The dendritic growth was further influenced by the high solidification rate of the TIG process and the melting point difference between Fe and WC [4.52]. Notably, WC has a melting point of approximately 2700°C, while LCS is approx. 1350°C [4.53]. The experimental results reflected the composition and dimensions of the infused tubular filler, which determines the ceramic powder content and its effect on the final microstructure. The cross-section of sample T1, processed with a 5 mm OD and 4 mm ID, is shown in Figure 4.15, focusing on the FZ at higher magnification.

Under the optical microscope, no remaining WC particles were detected, confirming that the WC-10%Co powder was fully dissolved and incorporated into the iron matrix solution. Since the BM and infused filler shared the same chemical composition (matched system), the molten pool primarily consisted of liquid Fe, into which W, C, and Co released from the dissociation of the WC-10%Co powder were integrated. These elements subsequently combined and resolidified in a dendritic manner, influenced by the presence of W and Co [4.54].

The microstructural evolution in the three samples, particularly the growth of dendritic austenite and the formation of MC carbides between the dendrite arms, can be attributed to the combined influence of WC particles and Co. WC particles within the deposited layer provided nucleation sites during solidification, promoting carbide precipitation, particularly MC

carbides, which preferentially formed between the dendritic arms. The Co content was also crucial as an austenite stabiliser, extending the austenite phase region during solidification and cooling. However, the effect of Co as an austenite stabiliser in such systems has not been extensively studied [4.55].

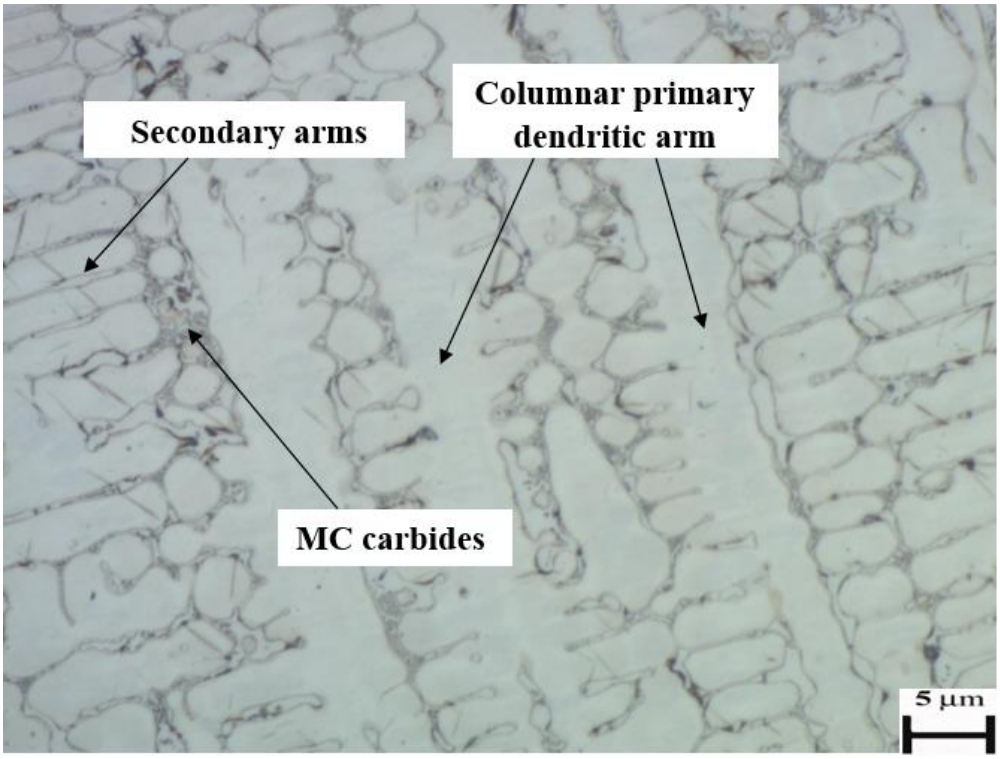

Figure 4.15. Microstructure of T1 LCS\ WC10%Co

The first phase to solidify was observed to be the primary dendritic austenite, followed by the growth of a secondary phase between the dendrite arms. Upon further cooling, the austenite phase partially transformed into martensite. However, the presence of Co restricted complete martensitic transformation, stabilising the austenite phase. Additionally, the formation of the fusion boundary was complex, influenced by WC and Co's differing dissolution and melting behaviours [4.53]. The resulting microstructure primarily consisted of a dendritic austenite network and eutectic MC carbides.

Variations in the dendritic arm dimensions among the three samples were directly related to the decreasing powder content controlled by the filler OD and ID. As the powder content

decreased, the WC proportion in the deposited layer was reduced, leading to smaller and more discontinuous dendritic arms. Furthermore, the reduced carbide content altered the interaction between MC carbides and dendritic austenite, resulting in less pronounced dendritic growth and modifications to the overall microstructural morphology. Additionally, reducing the powder content in T2 limited its ability to suppress martensitic transformation, further promoting martensite formation. As highlighted in Figure 4.16, the needle-like martensite transformation was initiated within the dendritic arms.

The chemical composition of key points labelled in Fig 4.16 was analysed using EDX. The results are summarised in Table 4.3, revealed distinct compositional differences between the

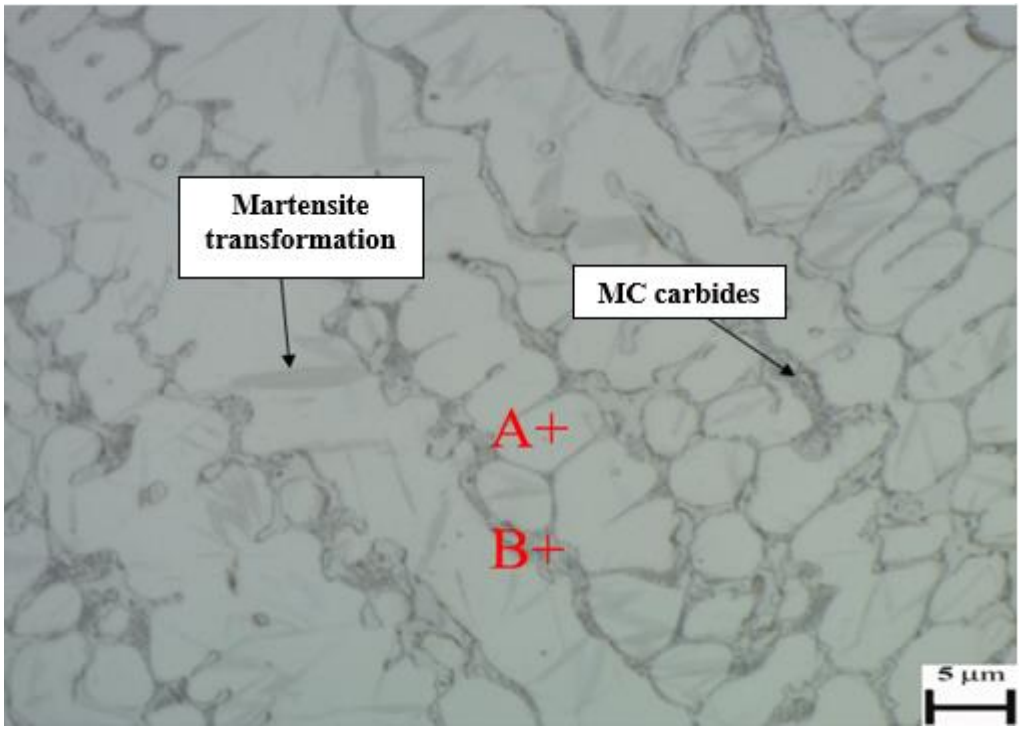

Figure 4.16. Microstructure of T2

Table 4.3 EDS analysis wt% for points labelled in Figure 4.16

Point	C	Fe	W	Co
A+	5.9	64.8	12.9	4.3
B+	8.7	55.2	10.7	2.1

dendritic arms and the eutectic regions. The dendritic arms exhibited a higher concentration of Fe and Co, with a lower C content than the eutectic regions. Based on these findings, it is reasonable to assume that the MC carbides present in the eutectic regions are primarily WFeC carbides.

In the sample with the lowest powder content T3, shown in Figure 4.17, the martensitic transformation within the dendritic arms is likely attributed to the reduced presence of WC and Co. The lower powder content decreased Co's stabilising effect on the austenite phase, thereby reducing the thermal stability of austenite during cooling and solidification. As a result, under rapid cooling conditions, the unstable austenite transformed into martensite within the dendritic structure. Furthermore, the increased thickness of the LCS-T filler tube introduced a higher proportion of ferrite or martensite forming elements, further promoting martensitic transformation.

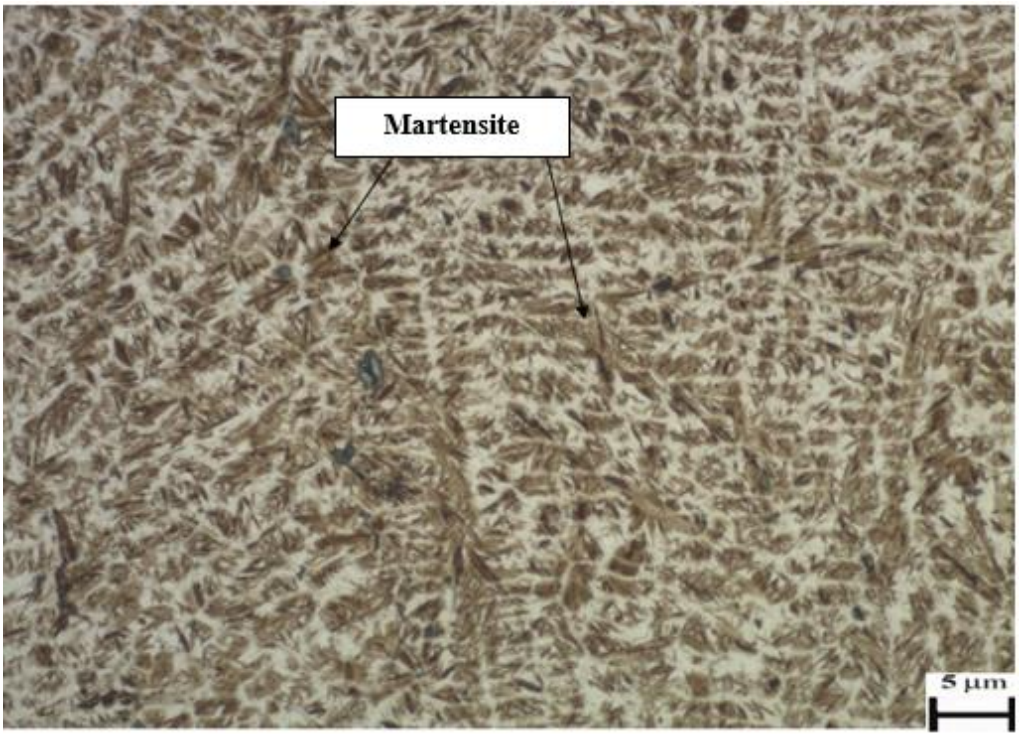

Figure 4.17. Microstructure of T3

The volume fraction of phases developed in the three samples was determined using image analysis software, as illustrated in Figure 4.18, 4.19, and 4.20. In T1, the volume fraction of dendrites was 82.3%, with MC carbides comprising 17.7%. In T2, the volume fraction of MC carbides increased to 20.6%, while the dendritic phase decreased to 79.4%. In the third sample T3, martensitic transformation occurred within the dendritic structure, reflecting the reduced carbide content and its influence on microstructural evolution.

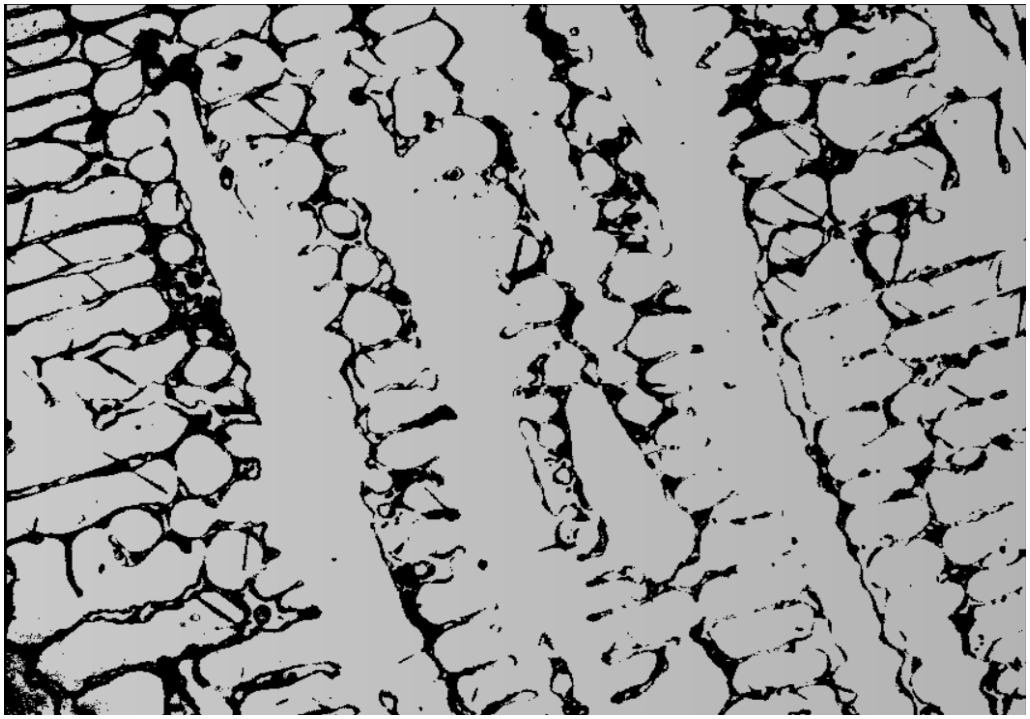

Figure 4.18. Processed micrograph of figure 4.15 analysed using ImageJ software to determine the volume fraction of dendrite and MC carbides

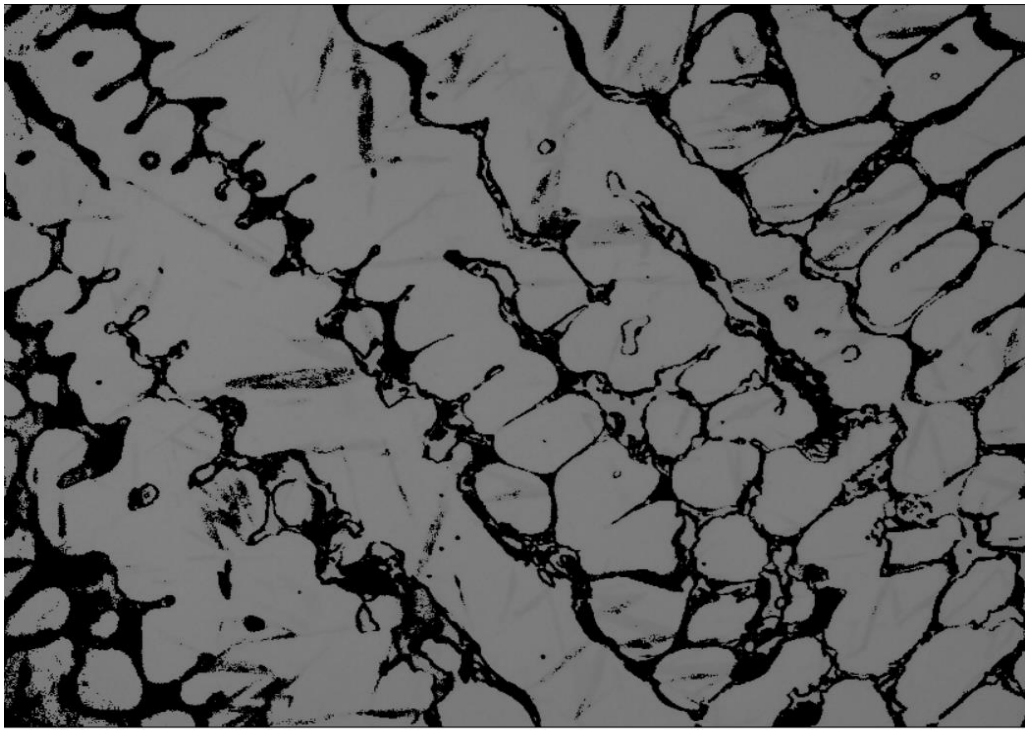

Figure 4.20. Processed micrograph analysing volume fraction of phases in Figure 4.16

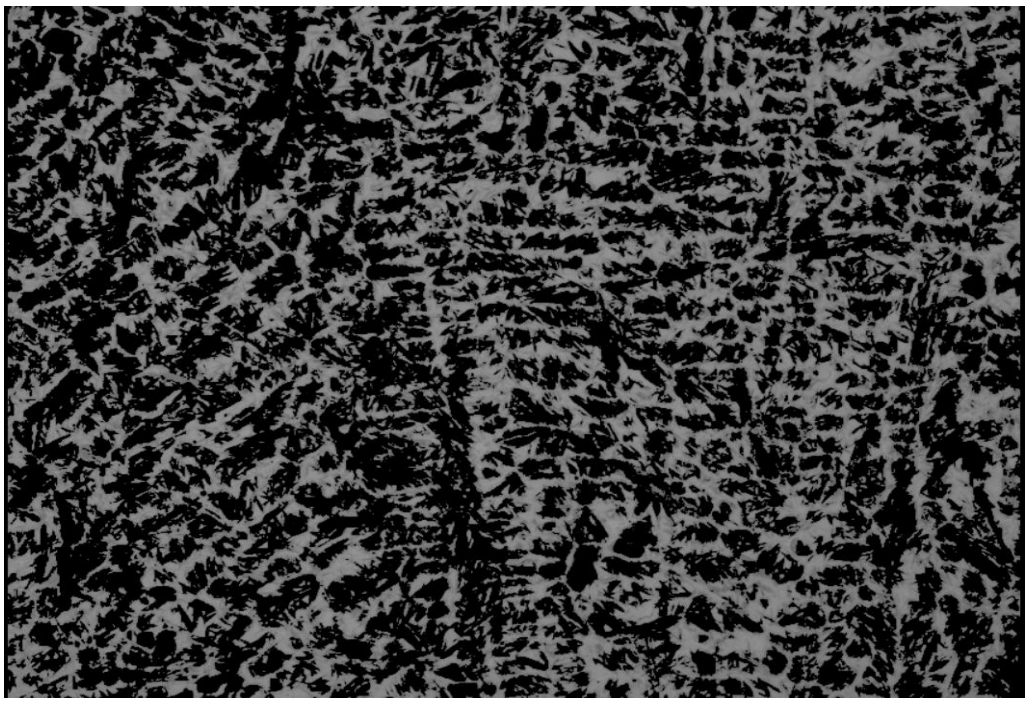

Figure 4.19 Processed image analysing volume fraction in Figure 4.17

Figure 4.21 illustrates XRD patterns for the three samples. The FZ of all three samples was

analysed, and the identified phases included ferrite, martensite, and MC carbides, confirming the microstructural evolution induced by the TIG deposition process.

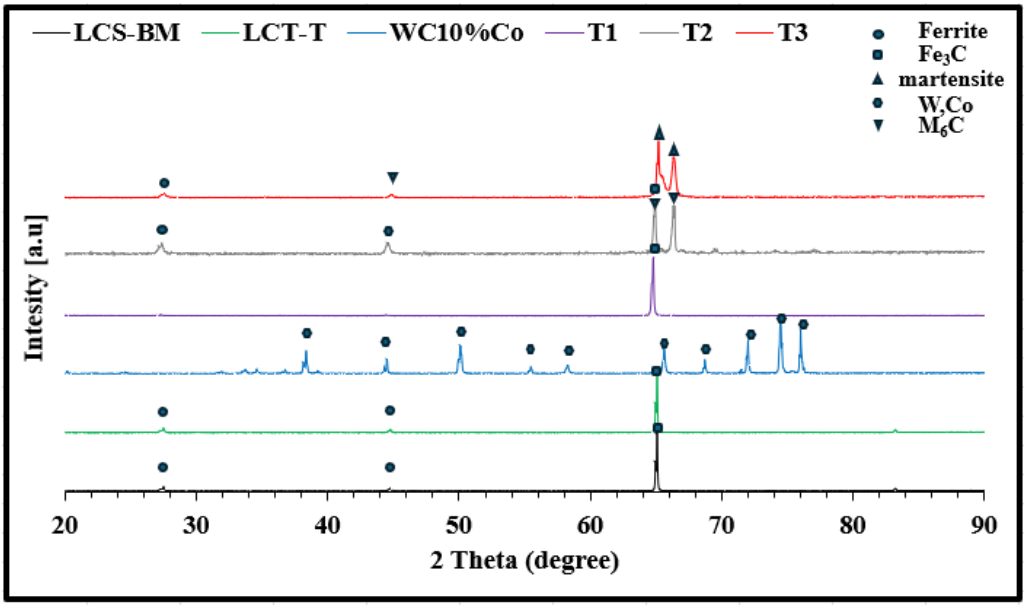

Figure 4.21. XRD patterns of T1, T2, and T3

4.5.2.2 Microhardness

Microhardness measurements of the three samples, illustrated in Figure 4.22, exhibited significant variation due to differences in filler dimensions and hence, content of powder and the resulting microstructures. Sample T1, which exhibited dendritic microstructure, recorded the highest hardness with a maximum microhardness of 789 HV. This hardness level was attributed to the increased W and Co content in the deposited layer.

Sample T2, characterised by a lower dendritic structure, showed a decrease in microhardness, with a maximum value of 603 HV. Sample T3, which had the lowest powder content and was dominated by a martensitic microstructure, exhibited the lowest microhardness among the three samples, reaching a maximum of 538 HV.

The hardness analysis demonstrated the versatility of this deposition method in tailoring microstructure and material properties through filler dimensions and powder content. These findings confirm that the method effectively integrates the influence of filler chemical

composition and dimensions, allowing for precise control over the mechanical properties of the deposited layer. Adjusting filler dimensions can achieve a wide range of hardness and wear resistance profiles, making this approach adaptable for various engineering applications requiring specific mechanical performance.

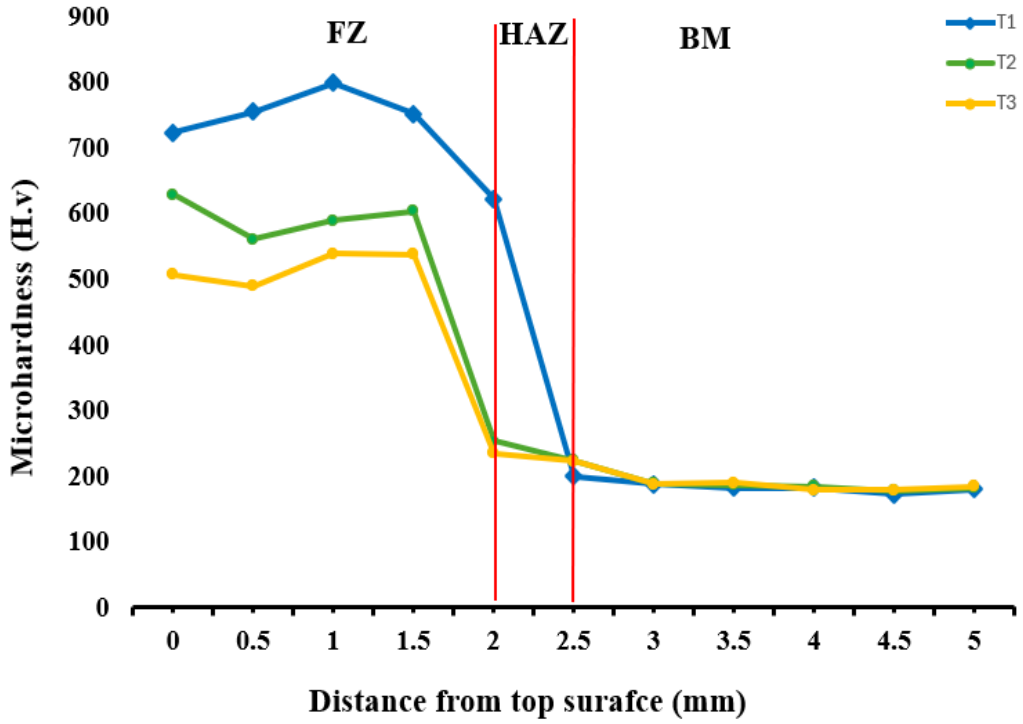

Figure 4.22. The microhardness analysis of T1, T2, and T3

4.5.3 Filler evaluation and development

The filler material was filled with SiC and WC in varying particle sizes and compositions, including SiC mixed with 10% Ni and WC mixed with 10% Co. The primary goal was to establish a strong metallurgical bonding between the FZ and the BM while ensuring the retention of hard ceramic particles within the steel matrix.

The chemical composition matching approach between the BM and filler material showed the potential to enhance the bonding between the deposited layer and the substrate. However, SiC exhibited significant segregation into the BM, driven by its high mobility in Fe at elevated temperatures. Similarly, the WC-10%Co system demonstrated strong interfacial bonding.

Despite these advantages, a significant challenge observed across all samples was the dissolution of ceramic particles within the molten steel pool.

Microstructural analyses using XRD, SEM-EDS, and optical microscopy confirmed the absence of ceramic particles in the final solidified structure. This dissolution behaviour was primarily attributed to the thermodynamic interactions in the molten pool, which hindered the retention of hard particles as discrete reinforcement phases. While the current method achieved strong interfacial bonding, it was insufficient in preserving ceramic particles, which is critical for achieving the desired MMC properties. This highlights the need for modifications in the filler material's chemical composition to enhance the stability of hard particles during the deposition process.

To address these challenges, alternative filler materials should be explored, particularly austenitic stainless steel such as 304LSS-BM or 316LSS-BM, which offers promising potential due to its Cr, Ni, and Mo content. These elements have been shown to significantly improve the stability of carbide particles and refine the microstructure:

- Cr: A strong carbide forming element, Cr could help stabilise carbide phases and reduce their dissolution in the molten pool. It also enhances corrosion resistance and contributes to overall material stability.
- Ni: By extending the austenitic region, Ni maintains ductility and toughness while minimising the formation of brittle martensitic phases.
- Mo: By refining carbide structures, Mo promotes a more uniform distribution of hard particles within the matrix, improving wear resistance.

These results from the present study emphasise the proposed method's potential for producing MMC’s by embedding hard ceramic particles within a steel matrix. However, controlling the filler's chemical composition is crucial to preserving the structural integrity of these particles.

4.6 Evaluation of 304LSS-T filler with SiC deposited on LCS-BM.

The selection of a 304LSS-T filler was driven by its chemical composition. This section evaluates the suitability of a 304LSS-T filler with SiC particles for MMC applications. The primary focus of this experiment is to examine the microstructure, chemical composition, and microhardness of the deposited layer, providing insights into the effectiveness of this tubular filler configuration and its potential for improving steel-matrix properties. A critical aspect of this study is determining whether the chemical composition of 304LSS-T filler effectively protects the embedded SiC particles from dissolution during the welding TIG process. If SiC dissolution occurs, the resulting microstructure will be analysed to understand the interaction between the filler material, SiC, and BM. This investigation will provide valuable insights into the suitability of 304LSS-T filler for MMC applications.

4.6.1 Experimental Procedure

A LCS substrate was selected for this study, with its characteristics detailed in Chapter 3. The 304LSS-T filler was fabricated with an OD of 4 mm and an ID of 2 mm. The microstructure and chemical composition of austenitic stainless steel are provided in Chapter 3, (Section 3.1.2.2). During the welding process, the current was varied between 165 and 190 A, while the voltage ranged from 11 to 15 V.

4.6.2 Results and Discussion

The microstructural characteristics of the deposited layer were examined using optical microscopy to evaluate the FZ and its interaction with the BM. As shown in Figure 4.23a, the FZ formed during the TIG welding process was distinguishable from the BM. However, at higher magnification presented in Figure 4.23b, the interface between the FZ and the BM exhibited noticeable elemental segregation, suggesting diffusion of elements such as Si across the interface during the deposition process.

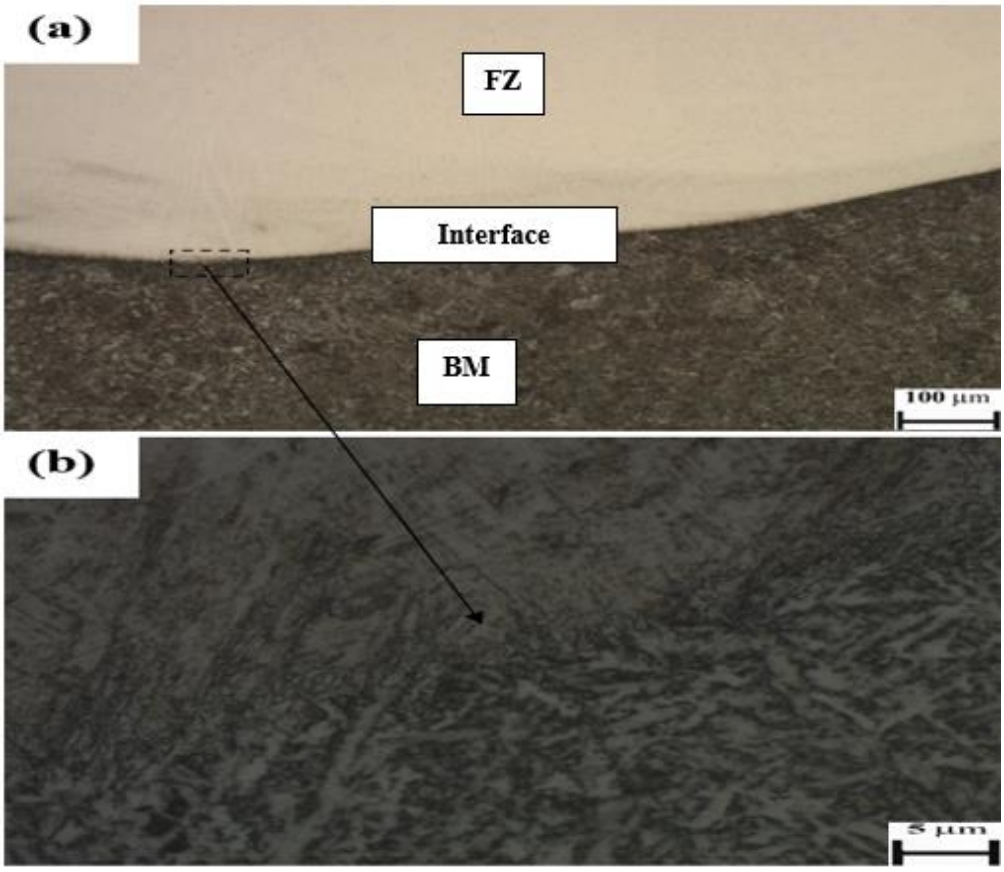

Figure 4.23. (a) Optical micrograph showing the FZ, IF, and BM, (b) Higher magnification of IF revealing detailed microstructural features

A more detailed microscopic examination of the FZ, as presented in Figure 4.24, revealed that the SiC particles within the 304LSS-T filler were dissolved during the TIG deposition process. No distinct SiC particles were observed in the final microstructure, indicating complete dissociation of the ceramic reinforcement. This dissolution facilitated the interaction of SiC derived elements, Si and C, with the molten stell matrix.

Upon solidification, the FZ exhibited a predominantly austenitic stainless-steel matrix, accompanied by the formation of carbides and iron silicide's, resulting from chemical reactions during cooling. Additionally, crack initiation was observed within the FZ, extending across the austenitic steel matrix boundaries. This feature is likely attributed to thermal stress during solidification or differential thermal expansion between the steel matrix and carbide phases.

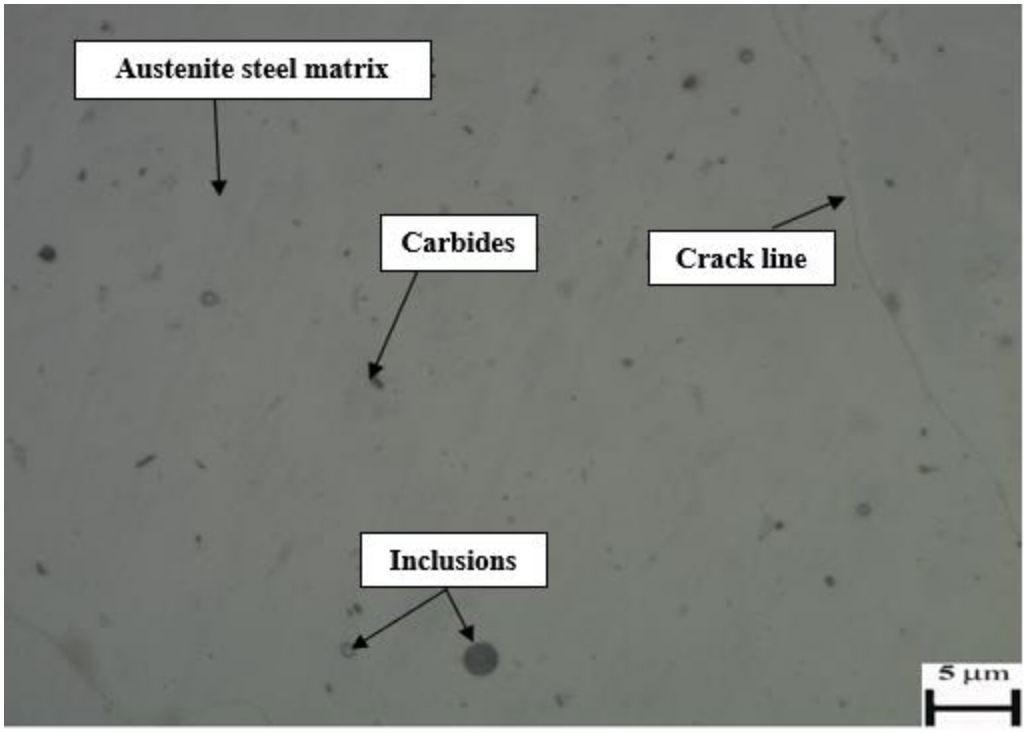

Figure 4.24. Microstructure of the FZ, showing the austenitic steel matrix with carbide growth and inclusions

The formation and growth of carbides and martensitic phases within the austenitic matrix introduced internal stresses due to variations in thermal expansion coefficients between the different phases. Additionally, volumetric contraction or expansion associated with phase transformations during cooling contributed to the development of residual stresses, which may have led to microcracking in the FZ. These findings highlight the complex interactions between SiC particles and the 304LSS matrix, highlighting the need for further optimisation in filler composition, deposition parameters to enhance the deposited composite layer's structural stability and mechanical performance.

4.6.3 Filler evaluation and development

The observed defects and phase transformations within the FZ, particularly in the 304LSS-T filler, underscore the need for material composition and dimensional design modifications to improve the overall microstructural stability. Owing to its enhanced chemical stability and

improved carbide retention, 316LSS-T was selected as the new filler material to address these challenges.

Including Mo in 316LSS is expected to be critical in stabilising chemical interactions within the FZ, potentially preventing excessive carbide formation. Mo has been shown to refine carbide structures in metal matrices [4.56] and may offer protection against carbide dissolution. Specifically, it enhances the stability of carbides, such as chromium carbides, by forming strong molybdenum-carbide bonds.

Furthermore, Mo's ability to strengthen the matrix interface reduces the likelihood of carbide dissolution during high-temperature processing, making it particularly effective in retaining the desired properties of MMC during fabrication [4.57]. As demonstrated in various advanced MMC studies, these characteristics make Mo particularly valuable in applications requiring high thermal stability and wear resistance [4.58].

Additionally, a dimensional filler tube modification was introduced to optimise deposition characteristics further. Increasing the ID from 2 mm to 3 mm reduced the filler thickness to 1 mm, effectively minimising the amount of melted austenitic matrix material during the welding process. This adjustment is expected to improve the retention of reinforcement particles. These modifications mark a significant step toward refining the MMC deposition process, which will ensure improved structural integrity.

4.7 Evaluation of 316LSS-T filler with SiC deposited on LCS-BM

Initial investigations employed LCS-T as the filler material, followed by 304LSS-T, which provided critical insights into microstructural evolution, microhardness, and chemical phase transformation. These studies revealed several challenges, including carbide formation, phase transformation, and interactions between the filler material, BM, as well as processing parameters which influenced the overall performance of the deposited layers.

Building on these findings, this study explores using 316LSS-T filler, with SiC particles, and deposited on LCS-BM via TIG welding. The primary focus of this section is to evaluate the resulting microstructure, the morphology of carbides, and the formation of new phases at the FZ and IF, to assess this novel filler system's effectiveness in developing MMC to achieve a comprehensive understanding.

4.7.1 Experimental procedure

The 316LSS-T filler was fabricated with an OD of 4 mm and an ID of 3 mm. During the welding process, the current ranged between 173 and 190 A, while the voltage varied between 14.9 and 15.3 V.

4.7.2 Results and Discussion

4.7.2.1 Microstructure and Phase Composition

The sample processed with a 316LSS-T filler containing silicon carbide SiC particles demonstrated effective retention of SiC within the FZ. As illustrated in Figure 4.25, the retained SiC particles are identifiable in the microstructure, with their size and morphology closely matching the SiC particles. This suggests minimal dissolution or structural alteration occurred during the deposition process, indicating improved particle stability within the molten pool. The matrix surrounding the retained SiC particles predominantly consists of retained austenite, with distinct carbide precipitation observed at austenite grain boundaries. The formation of these secondary carbide phases can be attributed to the partial dissolution of SiC particles during deposition and solidification. As the SiC particles interacted with the molten steel, Si and C were released, initiating the nucleation and growth of carbides between the austenitic grains.

While a substantial fraction of the SiC particles remained intact, some degree of dissolution contributed to carbide formation, reinforcing the mechanical integrity of the deposited layer. This finding highlights the effectiveness of the 316LSS-T filler material, and the precise

control over the processing parameters in preserving SiC particles, which is critical for achieving an MMC with enhanced wear resistance and structural stability.

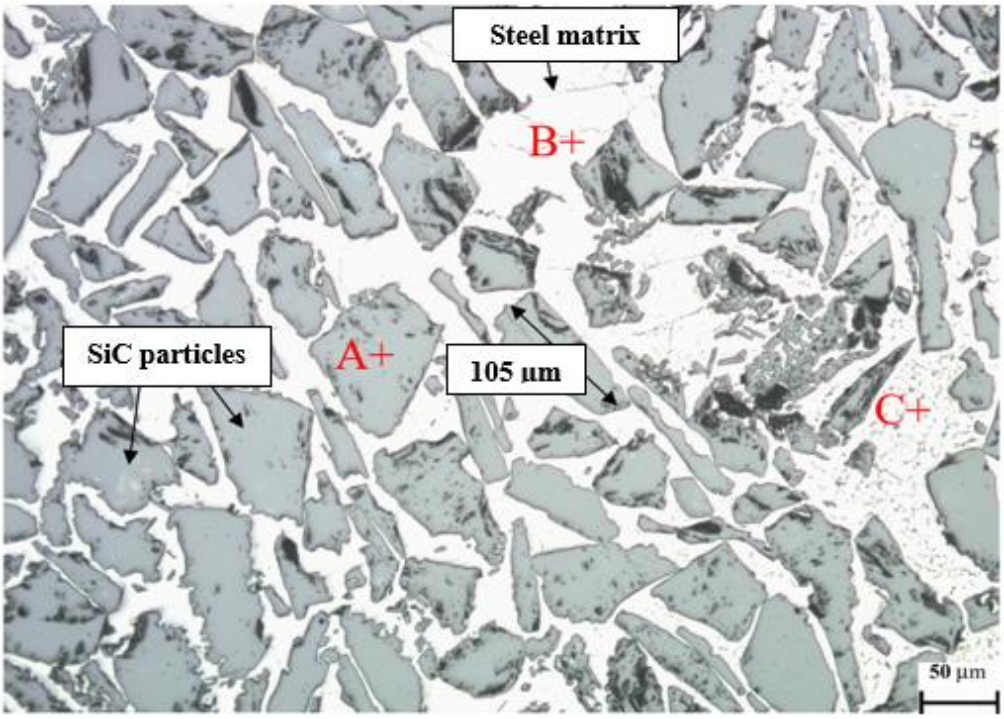

Figure 4.25. FZ of the sample processed with 316LSS-T filler, the microstructure shows retained SiC particles embedded within the steel matrix

Table 4.4 Chemical composition analysis of the three points labelled in Figure. 4.25 using EDS

Point	C	Si	Cr	Ni	Fe
A+	19.8	51.4	0.00	0.00	17.8
B+	5.3	1.8	3.1	3.2	87.6
C+	6.1	3.1	4.3	2.1	84.4

However, microcracks were observed in the steel matrix, which is likely attributed to high thermal stresses induced by carbide precipitation and the mismatch in thermal expansion between SiC and steel matrix. The chemical and thermal dynamics of this system are highly sensitive, particularly due to the reactive nature of Si in the molten steel state.

According to the Si-C-Fe phase diagram, Si exhibits high reactivity with Fe even at 1100°C, a temperature significantly below the melting points of both Si and Fe. This pronounced Si-Fe interaction necessitates precise control of processing conditions, as rapid diffusion and carbide

formation can substantially influence matrix evolution and microstructural stability. Uncontrolled Si-Fe interactions may lead to excessive carbide precipitation and localised stress accumulation, potentially contributing to cracking within the matrix.

Despite these challenges, the primary objective of retaining SiC particles within the austenitic steel matrix was successfully achieved. The 316LSS-T filler, with SiC particles, proved effective in creating a reinforced composite structure with minimal dissolution of SiC. This outcome underscores the viability of using a SiC filled in 316LSS-T filler to develop a durable composite system with promising tribological and mechanical performance enhancements.

EDS analysis was conducted on the sample, focusing on three distinct points, as labelled in Figure 4.25: Point A (ceramic particles), Point B (steel matrix), and Point C (carbide precipitation site).

Point A, located within the ceramic particles, the composition exhibited high carbon (C) content along with 51.4% Si and 17.8% Fe. This elemental composition is consistent with SiC, confirming the successful retention of ceramic particles within FZ and their minimal dissolution during the deposition process. At Point B, analysed within the steel matrix, the composition included C, Si, Cr, Ni, and Fe, aligning with the expected austenitic nature of the 316LSS matrix. This confirms that the overall steel composition remained stable despite interacting with SiC during processing.

At Point C, which was identified near a potential carbide precipitation site, the analysis revealed elevated levels of C and Si compared to the steel matrix. This suggests that partial dissolution of SiC particles occurred during the deposition process, releasing Si and C into the molten steel matrix. The presence of these elements promoted the precipitation of carbides, particularly chromium carbides, within the matrix. These findings provide valuable insights into the chemical interactions occurring during deposition.

Figure 4.26 presents the XRD diffraction patterns for the LCS-BM, 316LSS-T, the SiC, and the processed sample. The analysis focused on a localised area and confirmed the retention of SiC within the matrix, as evidenced by the presence of characteristic SiC peaks in the diffraction pattern. The XRD patterns were compared against reference spectra for SiC, verifying that SiC particles remained intact within the processed sample.

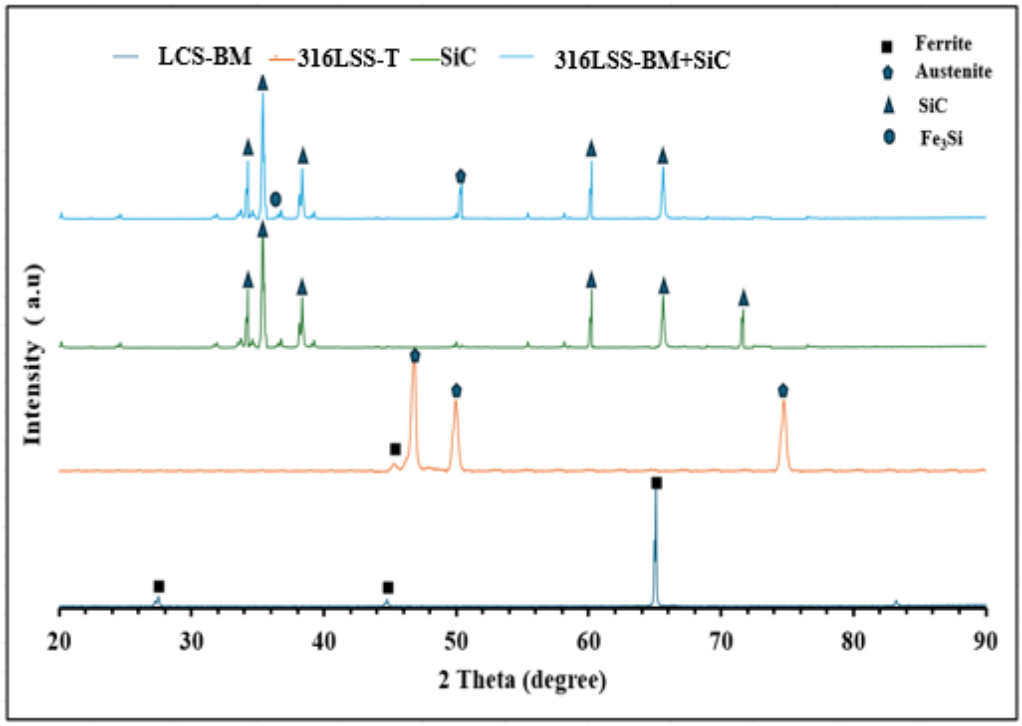

Figure 4.26. XRD for 316LSS-BM +SiC sample

Additionally, distinct peaks corresponding to austenite were observed, confirming the predominantly austenitic nature of the steel matrix. Notably, the analysis identified peaks corresponding to iron silicide phases Fe_3Si, suggesting that partial dissolution of SiC particles occurred during the deposition process. This dissolution led to chemical interactions between the released Si and Fe, forming iron silicide phases within the matrix. These findings reinforce the effectiveness of the 316LSS-T filler material in retaining SiC particles while also highlighting the complex phase interactions that occur during deposition.

4.7.2.2 Microhardness

The sample underwent line microhardness testing using an automatic micro-indentation testing machine to evaluate hardness distribution across the cross-section as shown in Figure 4.27. The results revealed that the BM exhibited a microhardness of approximately 180 HV, characteristic of the ductile LCS substrate. In contrast, the FZ displayed significantly higher hardness values, ranging from 800 HV to 1125 HV. The elevated hardness in the FZ is primarily attributed to the presence of retained SiC particles and precipitated carbides, which serve as reinforcement phases within the steel matrix.

The resulting unique microstructure and increased hardness are expected to significantly enhance the composite's wear resistance, making it a viable candidate for applications requiring superior durability and mechanical performance.

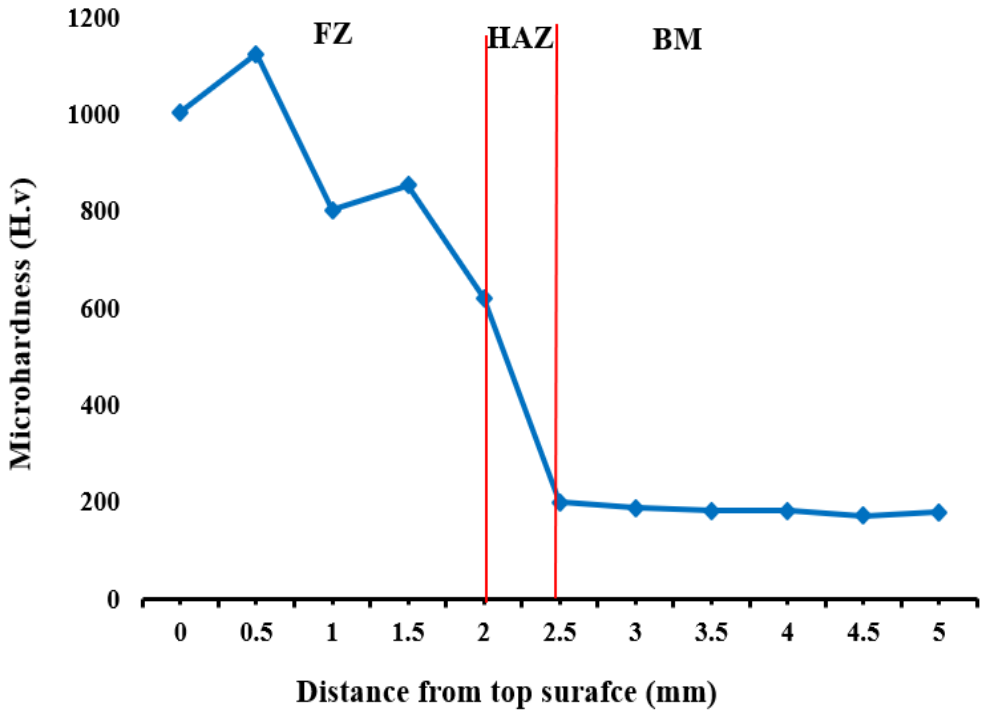

Figure 4.27 Line Microhardness analysis

4.8 Evaluation of 316LSS-T filler with WC-10%Co deposited on LCS-BM.

This study section focuses on fabricating MMC using a 316LSS-T filler filled with WC-10%Co powder deposited onto a LCS-BM. The primary objective is to evaluate the resulting microstructure, microhardness, phase composition, and interface characteristics between the BM and FZ. Upon successful deposition, these MMC will undergo further analysis to assess their wear properties, contributing to the broader aim of this thesis: enhancing the wear resistance of steel surfaces through the development of advanced MMC. This investigation seeks to establish an optimised processing approach for producing high-performance, wear resistant steel-based composites suitable for demanding engineering applications.

4.8.1 Experimental Procedure

The LCS substrate, and the 316LSS-T were selected as in the previous section. The size, morphology, and chemical composition of WC-10%Co powder are detailed in Chapter 3, (Section 3.1.4.2). During the welding process, the current ranged between 173 and 190 A, while the voltage varied between 14.9 and 15.3 V.

4.8.2 Results and Discussion

4.8.2.1 Microstructure and Chemical Composition

Figure 4.28 presents the microstructure of the processed sample, highlighting the FZ and the BM. The FZ exhibits a homogeneous dendritic network formed during solidification, with retained hard particles embedded within the steel matrix. Despite partial dissolution, the WC hard particles remained in the steel matrix, contributing to the overall composite structure. In contrast, the BM retained the characteristic microstructure of LCS, distinguishing it from the modified MMC morphology observed in the FZ.

Figure 4.29 shows the typical microstructure of the FZ, which includes a homogeneous dendritic network and dispersed hard particles. The 316LSS-T filler material exhibited an austenitic stainless-steel microstructure, which melted and was incorporated into the solidified layer. The chromium content in the filler wire promoted the formation of dendritic carbides,

while the dissolution WC-Co released W and C atoms, further enhancing carbide formation during solidification [4.59, 4.60].

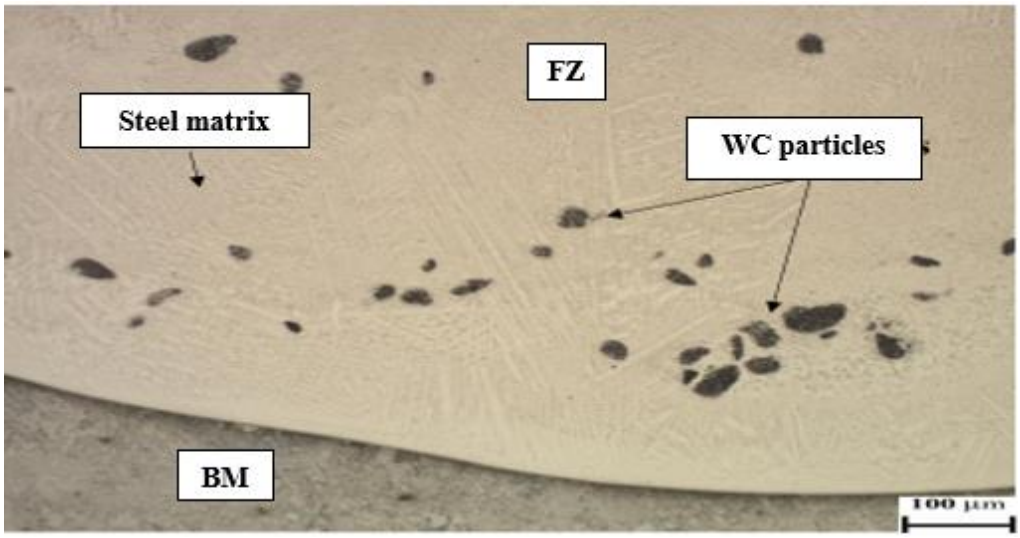

Figure 4.29. Cross-section of 316SSWC10%CO, showing the FZ, and BM

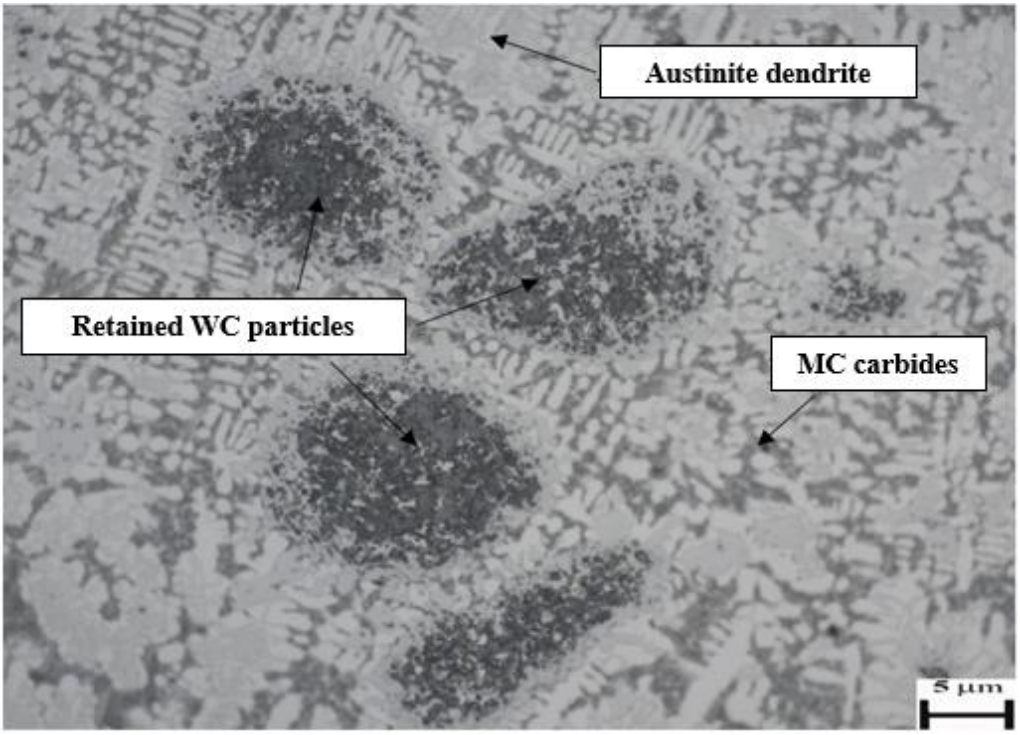

Figure 4.28. Microstructure of the FZ of sample 316LWC10%Co

Figure 4.30 highlights the retained WC ceramic particles embedded within the steel matrix, illustrating their distribution and interaction with the surrounding material. A transition layer is visible at the interface between the WC particles and the steel matrix, indicating strong metallurgical bonding. The steel matrix is uniformly distributed around the embedded particles, further reinforcing the integrity of the composite structure. After grinding and polishing, the embedded particles appeared in relief above the relatively softer steel matrix, confirming their superior hardness and wear resistance.

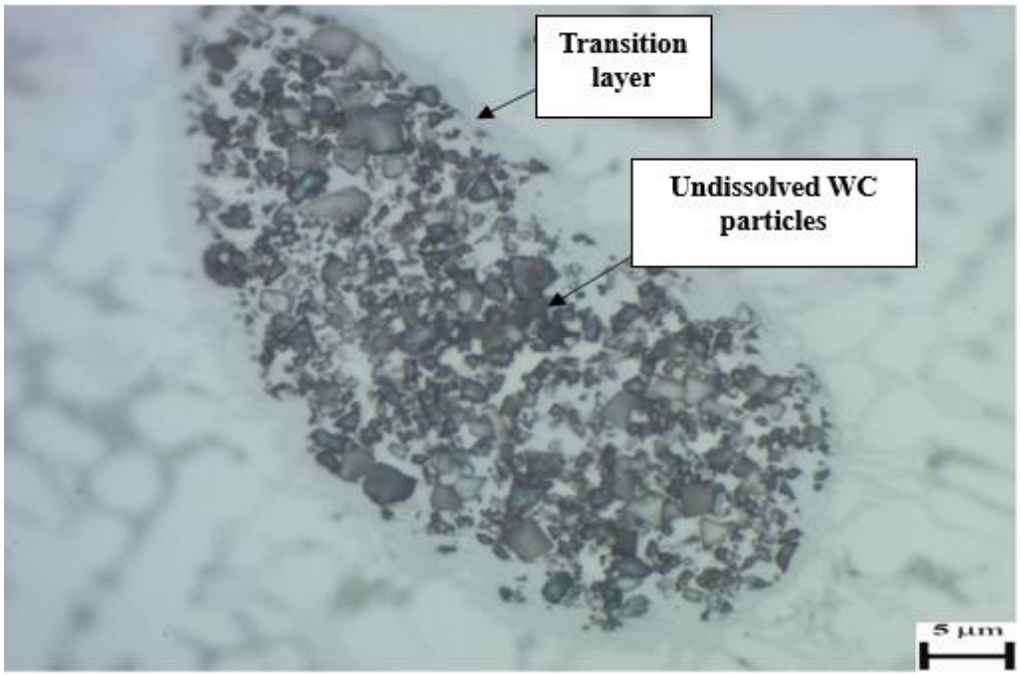

Figure 4.30. Microstructure of sample 316SSWC10%Co, showing the retained WC particles, standing out in relief above the steel matrix after grinding and polishing

XRD analysis confirmed the presence of M_6C carbides, which were observed surrounding the retained WC particles, as shown in Figure 4.31. These findings agree with previous studies [4.49, 4.61], further validating the formation of complex carbides during solidification. Based on the chemical composition of the BM, reinforcement particles, and filler material, it can be inferred that the majority of the carbides formed were $(Co, W, Cr, Fe)_{23} C_6$ or $(Co, W, Cr, Fe)_6C$ [62]. The presence of Cr, W, and C atoms in the dendritic growth region contributed to the formation of $M_{23}C_6$ carbides, further influencing the microstructural evolution [4.63].

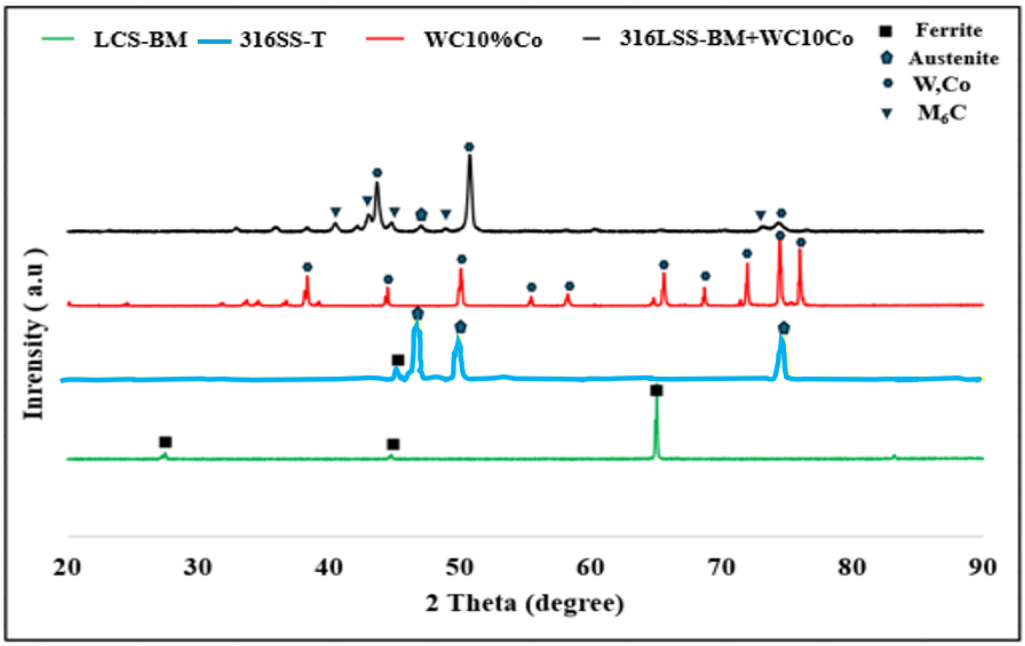

Figure 4.31. XRD results for 316LSS-BM+WC10Co sample

The chemical composition of the processed sample was analysed using EDS to assess the elemental distribution along vertical and horizontal lines and at specific points within the weld region. The results, illustrated in Figure 4.32 and Table 4.5, provide insight into diffusion patterns, the uniformity of elemental composition, and the retention of WC particles within the steel matrix. The vertical line analysis from the top of the FZ down to the BM revealed significant changes in elemental concentrations. The Cr content decreased slightly, moving downward, suggesting a gradual dilution of the 316LSS-T filler within the FZ. Co remained relatively stable along the vertical line but slightly increased in deeper regions, possibly due to diffusion from the WC. Ni exhibited variability along the vertical axis, peaking at 11.7 wt% at V1 (see figure 4.32) and decreasing toward the BM, a trend consistent with filler dilution within the FZ. The WC content ranged from 12 wt% to 25 wt%, confirming the partial distribution and retention of WC particles within the steel matrix. Fe concentration was uniformly distributed along the FZ, peaking around V3 and V5 (63 wt%), with a notable increase at V10 (93 wt%), which aligns with the expected composition of the LCS-BM.

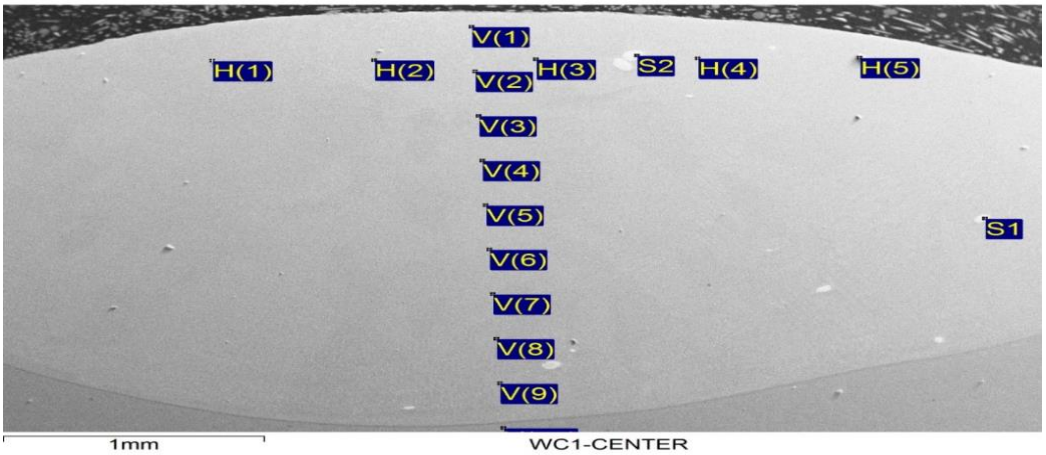

Figure 4.32. EDS line, and spot analysis on the sample of 316LSS-T with WC10%Co

Table 4.5 EDS line and spot results labelled in Fig. 4.32

Spectrum	Cr	Mn	Co	Ni	WC	Fe
V (1)	6.09	0.84	2.78	11.70	13.99	56.46
V (2)	5.59	0.71	2.00	8.75	25.21	49.57
V (3)	3.77	0.71	2.34	10.22	12.93	63.34
V (4)	3.42	0.73	1.99	8.83	13.78	64.42
V (5)	3.70	0.74	2.29	9.62	15.88	61.12
V (6)	3.79	0.85	2.43	10.02	16.11	60.29
V (7)	4.16	0.71	2.36	9.64	18.16	58.64
V (8)	3.79	0.70	2.46	10.25	14.64	61.89
V (9)	3.67	0.72	2.80	11.22	15.57	60.37
V (10)	0.00	1.33	0.00	0.00	0.00	93.87
H (1)	3.02	0.67	2.03	7.17	11.73	52.11
H (2)	4.03	0.75	2.47	11.57	13.88	59.76
H (3)	5.20	0.70	2.47	11.93	15.00	57.17
H (4)	4.26	0.82	2.59	10.70	15.91	58.61
H (5)	1.70	0.25	0.91	0.00	3.97	23.94
S1	1.08	0.20	3.78	2.01	73.52	9.71
S2	0.75	0.00	4.39	2.51	74.04	7.53

This analysis highlights the successful incorporation of WC particles into the FZ while ensuring their chemical stability and distribution within the matrix.

The horizontal line analysis, conducted across the FZ, confirmed a uniform chemical composition. Cr, Co, Ni, and Fe exhibited consistent concentrations across the horizontal

spectra, indicating effective mixing and homogeneity within the FZ. Spot analysis at specific points (S1 and S2) further validated the chemical characteristics of retained WC particles. At S1, the WC concentration was measured at 73.52 wt%, while at S2, it was 74.04 wt%, confirming a high presence of undissolved WC particles. This demonstrates that a significant fraction of WC reinforcement remained intact within the steel matrix, reinforcing the stability and structural integrity of the composite. Overall, the chemical composition analysis validates the successful incorporation of WC particles into the steel matrix, resulting in an MMC structure with strong particle-matrix bonding.

4.8.2.2 Microhardness

The hardness was evaluated using automated micro-hardness testing machine described in Chapter 3, (Section 3.2.6.1). The results provide insights into hardness distribution and the contribution of WC particles to localised hardness. A line hardness analysis was conducted from the top surface of the FZ toward the BM. The hardness profile, as shown in Figure 4.33, revealed a maximum hardness of 925 HV at a depth of 1.5 mm within the FZ. Compared to the BM, this increase in hardness can be attributed to the dispersion of WC particles and the formation of a refined microstructure within the FZ. However, due to its indentation size and limited resolution at the microscale, the automated hardness testing machine did not fully capture the hardness contribution of the retained WC particles, which are significantly harder than the surrounding steel matrix. To overcome the limitations of automated testing, a manual testing machine was employed to measure hardness in localised regions, particularly on retained WC particles. The results demonstrated a maximum hardness of 1095 HV, substantially higher than the values obtained from the line analysis. This increase in localised hardness confirms the role of undissolved WC particles.

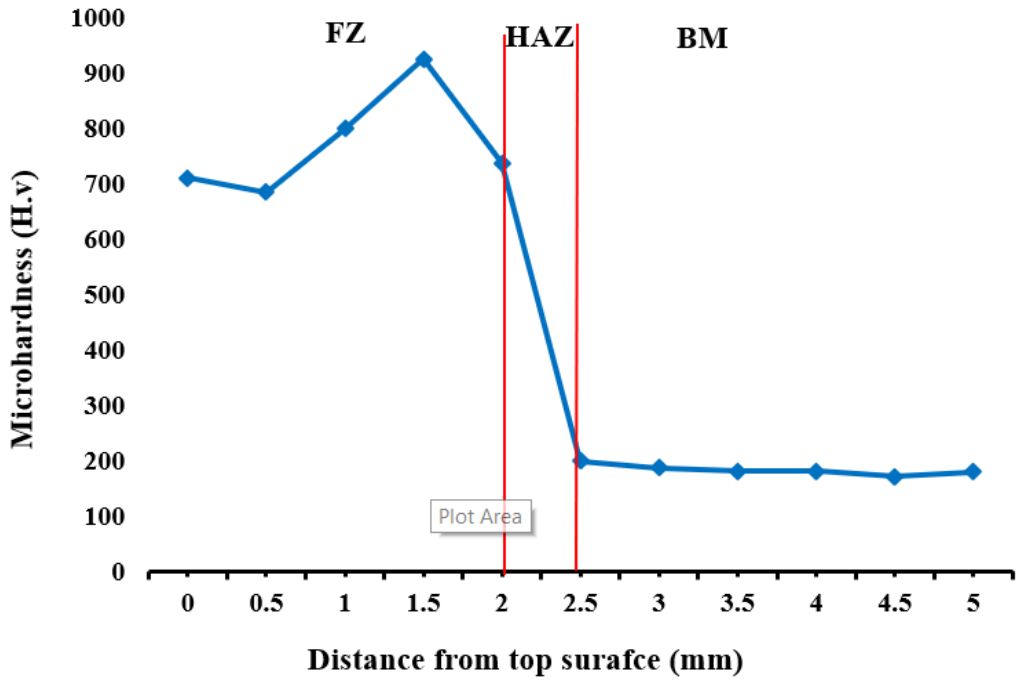

Figure 4.33. Line microhardness analysis

The high hardness observed in the FZ aligns with the presence of WC particles, which are well known for their exceptional hardness and wear resistance. Additionally, as confirmed by EDS analysis, the diffusion of W and Co into the steel matrix may also contribute to overall hardness enhancement. The maximum hardness of 1095 HV demonstrated the potential of this composite material for applications requiring high wear resistance and superior mechanical strength. This process's success was achieved through the optimisation of the tubular filler's composition and dimensions, as well as the TIG welding process parameters, ensuring uniform particle dispersion and strong particle-matrix bonding. These findings provide critical data for further dry sliding wear analysis, reinforcing this MMC's potential for high-performance applications requiring superior wear resistance compared to conventional base metals.

4.9 Evaluation of HF600 hard facing electrode deposited on LCS-BM

The deposition of MMC layers using tubular fillers offers several advantages, including enhanced bonding between the deposited layer and substrate, improved matrix-reinforcement

particle adhesion, controlled microstructure evolution, and superior mechanical properties. The novel 316LSS-T filler proposed in this study incorporates SiC and WC particles as reinforcements, leveraging the distinct properties of these ceramics to create a hard and wear-resistant surface.

As this approach is relatively new, the fabricated MMC will be systematically compared with a commercially available solid hard-facing filler material, HF600, to evaluate its performance and suitability for wear-resistant applications. A comprehensive investigation will be conducted to characterise the microstructure, chemical composition, and microhardness of the HF600 deposit. The findings will contribute to developing high-performance, wear-resistant coatings that offer extended service life for critical components in demanding industrial applications.

4.9.1 Experimental procedure

A LCS-BM was selected. A commercially available hard-facing electrode, HF600, was used as the filler material, and its chemical composition and characteristics are described in Chapter 3, (Section 3.1.5). The current ranged from 162 to 186 A during the welding process, while the voltage varied between 14.4 and 16.2 V.

4.9.2 Results and Discussion

4.9.2.1 Microstructure and Chemical Composition

Figure 4.34 presents the sample's microstructure processed with the HF600 electrode, highlighting the FZ and the BM interface. The FZ exhibits a refined microstructure, while the interface demonstrates a strong metallurgical bonding with a clear transition from the BM to the FZ. The chemical composition of the HF600 electrode includes 0.4 wt% C, 9.1 wt% Cr, 3 wt% Si, and 0.5 wt% Ni, with the balance being Fe. This specific alloy composition promotes the formation of a hard and wear-resistant microstructure upon deposition. The microstructural analysis of the FZ, as shown in Fig 4.35, revealed a martensitic matrix known for its high

hardness and wear-resistance properties, making it suitable for wear-resistant applications. Additionally, light-coloured segregated regions were observed, which are presumed to be

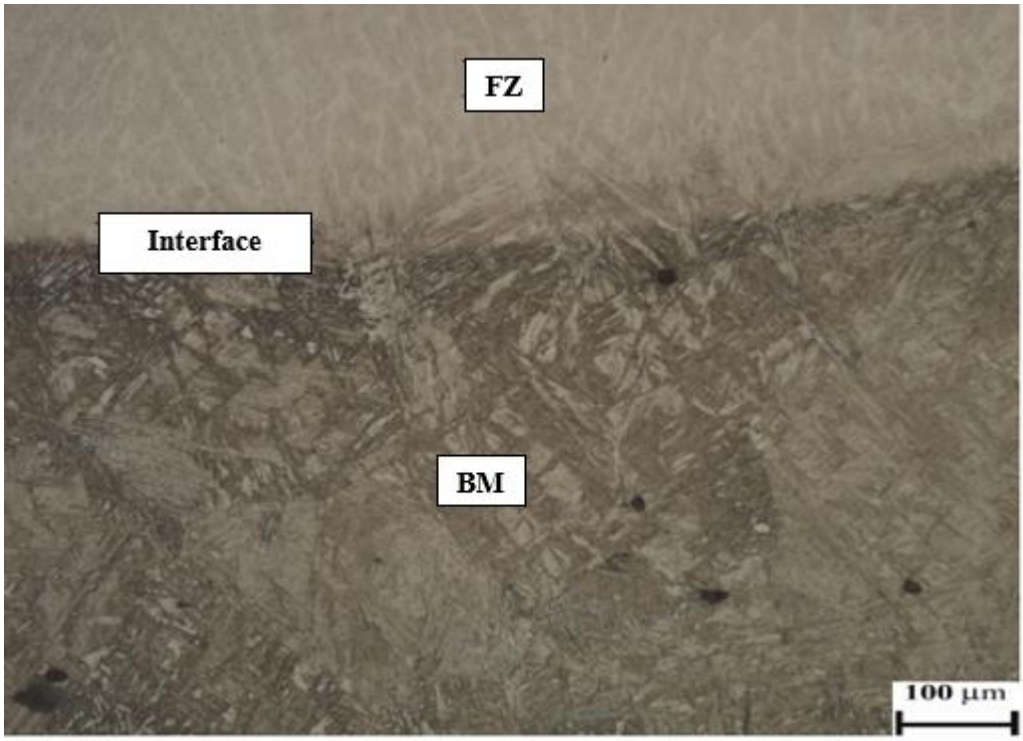

Figure 4.34. Microstructure of hard facing electrode HF600, showing distinct regions: FZ, IF, and BM

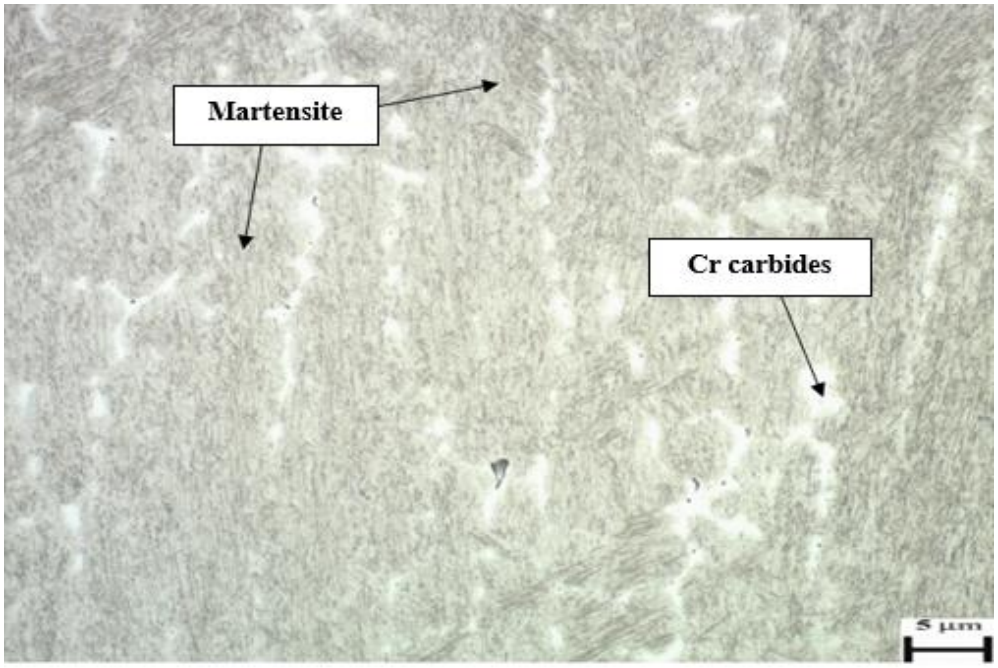

Figure 4.35. High magnification of the FZ

chromium carbides. The presence of Cr carbides is attributed to the high Cr content in the HF600 electrode, which reacts with carbon during solidification to form carbide phases. This combination of martensite and chromium carbides ensures that the HF600 electrode delivers superior hardness and wear resistance, making it a reliable option for applications requiring enhanced surface durability.

The chemical composition of the deposited HF600 layer was analysed using EDS to assess elemental distribution along vertical and horizontal line scans, as illustrated in Figure 4.36. The results, summarised in Table 4.8, provide insights into elemental diffusion and phase stability within the FZ and near the IF with BM. The analysis revealed that the FZ's C content was higher than that of the BM, aligning with the HF600 electrode composition and its intended role in enhancing hardness and wear resistance. Additionally, Si absent in the BM composition, was detected near the interface at V9 and V10, suggesting elemental diffusion or redistribution during the deposition process.

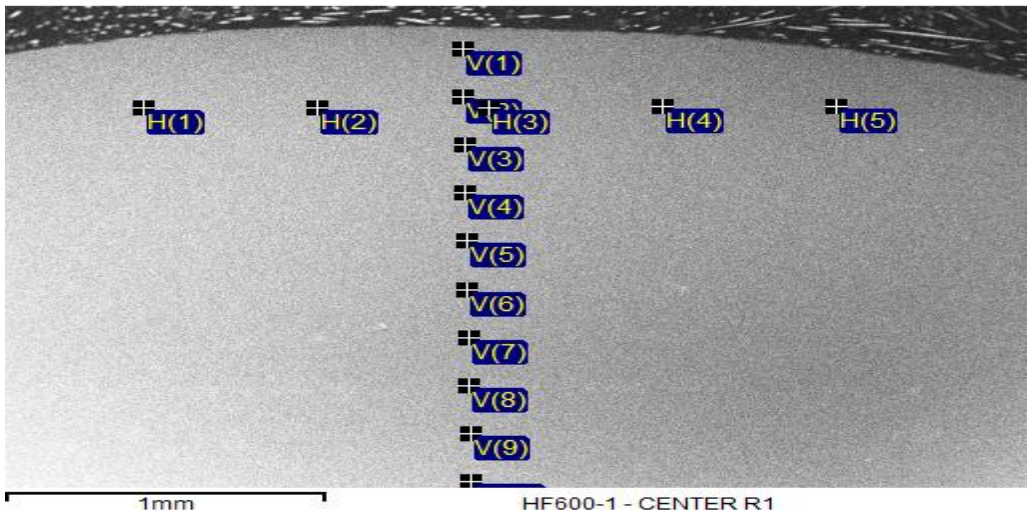

Figure 4.36. EDS line analysis on the sample of HF600 electrode

Fe concentration ranged between 85.4 wt% and 89.4 wt% in the vertical line analysis, with a uniform distribution observed in the horizontal line scan across the FZ. Cr exhibited a decreasing concentration along the vertical scan towards the BM and was recorded as 0% near the interface within the FZ. This behaviour suggests limited diffusion of Cr at the transition

zone between the FZ and BM, indicating that Cr remained primarily within the FZ and did not significantly diffuse into the BM. Overall, the FZ's chemical composition displayed a uniform elemental distribution, reinforcing the stability of the deposited layer and confirming the effective integration of alloying elements within it.

Table 4.6 EDS line results in wt% labelled in Fig. 4.36

Spectrum	C	Si	Cr	Fe
V (1)	5.53	1.88	5.42	85.47
V (2)	5.36	2.01	5.55	86.49
V (3)	5.73	2.06	6.02	85.20
V (4)	5.25	2.07	5.72	85.41
V (5)	4.89	1.88	5.14	87.44
V (6)	4.84	1.88	5.47	85.84
V (7)	4.33	1.41	3.54	89.44
V (8)	3.99	0.24	0.00	93.93
V (9)	4.25	0.37	0.00	94.16
V (10)	3.93	0.28	0.00	94.46
H (1)	5.53	2.07	5.67	86.07
H (2)	5.71	2.03	5.58	85.90
H (3)	5.29	2.13	5.95	85.74
H (4)	5.71	2.19	5.85	85.42
H (5)	5.44	2.01	5.70	86.19

4.9.2.2 Microhardness

The line graph in Figure 4.37 represents the microhardness variation as a function of distance from the top surface toward the BM. The data show a gradual decrease in hardness, with a maximum hardness of ~600 HV at the top surface, attributed to the martensitic microstructure and the dispersion of chromium carbides. As the distance from the top surface to the BM increases, the hardness progressively decreases, indicative of reduced carbide precipitation and a decrease in martensitic transformation.

The deposition of the HF600 hard-facing electrode on the LCS-BM significantly improved surface hardness, primarily due to the formation of martensite and chromium carbides. A gradual transition in microstructure was observed from the top surface of the deposit to the BM, reflecting effective metallurgical bonding.

The overlay achieved a peak microhardness of approximately 600 HV at the top surface, with a gradual reduction in hardness observed as depth increased. The metallurgical and hardness transition ensures strong bonding with the substrate, reinforcing the effectiveness of the HF600 electrode for surface hardening applications. Future investigations will focus on evaluating the wear-resistance performance of the HF600 deposited layer to further validate its suitability for wear-resistant applications.

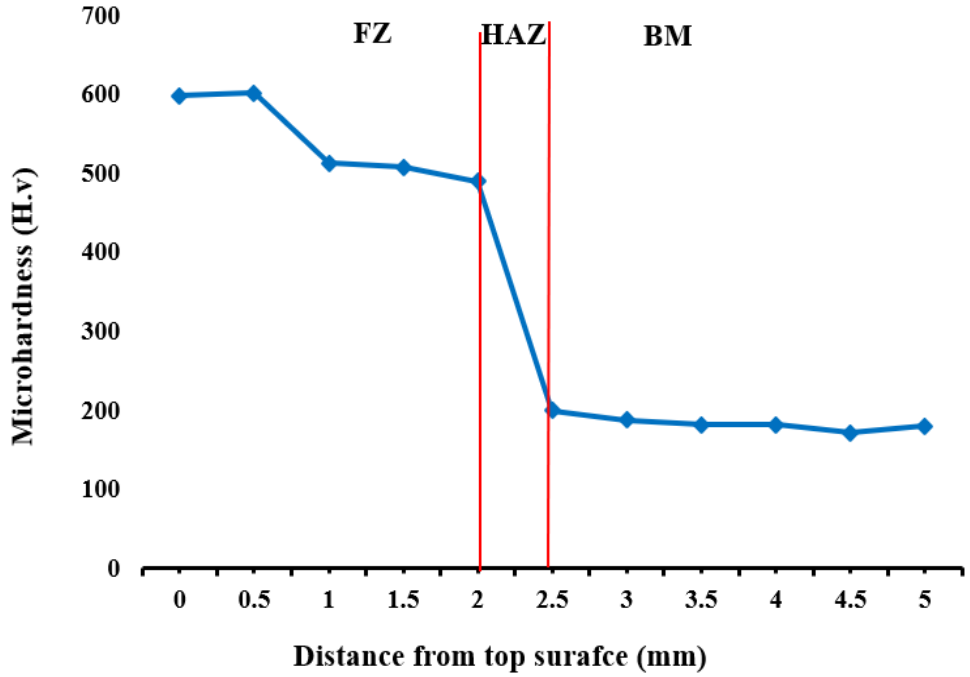

Figure 4.37 Line microhardness analysis

4.10 Conclusions

This chapter systematically evaluated tubular fillers, including LCS-T, 304LSS-T, and 316LSS-T, filled with SiC and WC particles, alongside a commercial HF600 hard-facing electrode. The MCS-T and LCS-T fillers partially or entirely dissolved SiC particles, leading to high-carbon regions that formed martensite and graphite structures. While improving stability, the 304LSS-T filler led to carbide precipitation and cracking, necessitating an alternative filler material. The 316LSS-T filler effectively retained SiC and WC particles, reducing dissolution and maintaining microstructural integrity. The SiC-reinforced 316LSS-T

filler resulted in Fe_3Si phase formation, while the WC-10%Co reinforced 316LSS-T filler promoted M_6C carbide formation, leading to a uniform dendritic microstructure with peak hardness values of 1125 HV and 1095 HV, respectively.

The HF600 electrode, despite achieving a martensitic matrix with chromium carbides and a peak hardness of 600 HV, exhibited lower hardness than the ceramic-filled tubular fillers. Thus, 316LSS-T fillers were selected as the optimal material for further evaluation. In the next chapter, 316LSS-T fillers will be used to replicate the repair process of LCS-BM and 316LSS-BM discs, and dry sliding wear tests will be conducted to assess their performance and durability. This investigation will provide further insights into the tribological behaviour of these deposits and their potential for industrial applications.

4.11 References

[4.1] Holmberg, K. and A. Mathews, Coatings tribology: a concept, critical aspects and future directions. Thin Solid Films, 1994. 253(1-2): p. 173-178.

[4.2] Mao, B., et al., Laser surface texturing and related techniques for enhancing tribological performance of engineering materials: A review. Journal of Manufacturing Processes, 2020. 53: p. 153-173.

[4.3] Priest, M. and C.M. Taylor, Automobile engine tribology—approaching the surface. Wear, 2000. 241(2): p. 193-203.

[4.4] Archard, J., Contact and rubbing of flat surfaces. Journal of applied physics, 1953. 24(8): p. 981-988.

[4.5] Archard, J.F. and W. Hirst, The wear of metals under unlubricated conditions. Proceedings of the Royal Society of London. Series A. Mathematical and Physical Sciences, 1956. 236(1206): p. 397-410.

[4.6] Al-Karawi, H. and M. Al-Emrani, The efficiency of HFMI treatment and TIG remelting for extending the fatigue life of existing welded structures. Steel Construction, 2021. 14(2): p. 95-106.

[4.7] Mridha, S. and T. Baker, Metal matrix composite layer formation with 3 μm SiCp powder on IMI318 titanium alloy surfaces through laser treatment. Journal of materials processing technology, 1997. 63(1-3): p. 432-437.

[4.8] Patel, P., S. Mridha, and T.N. Baker, Influence of shielding gases on preheat produced in surface coatings incorporating SiC particulates into microalloy steel using TIG technique. Materials Science and Technology, 2014. 30(12): p. 1506-1514.

[4.9] Muñoz-Escalona, P., S. Mridha, and T.N. Baker, Effect of shielding gas on the properties and microstructure of melted steel surface using a TIG torch. Advances in Materials and Processing Technologies, 2016. 1(3-4): p. 435-443.

[4.10] Muñoz-Escalona, P., S. Mridha, and T.N. Baker, Effect of silicon carbide particle size on microstructure and properties of a coating layer on steel produced by TIG technique. Advances in Materials and Processing Technologies, 2016. 2(4): p. 451-460.

[4.11] Muñoz-Escalona, P., et al., Silicon carbide particulates incorporated into microalloyed steel surface using TIG: microstructure and properties. Materials Science and Technology, 2019. 36(1): p. 17-32.

[4.12] Baker, T.N., et al., Role of preplaced silicon on a TIG processed SiC incorporated microalloyed steel. Materials Science and Technology, 2020. 36(12): p. 1349-1363.

[4.13] Munoz-Escalona, P., S. Mridha, and T. Baker, Advances in Surface Engineering Using TIG Processing to Incorporate Ceramic Particulates into Low Alloy and Microalloyed Steels – A Review. Advances in Science and Technology Research Journal, 2021. 15(3): p. 88-98.

[4.14] Mridha, S., et al., Intermetallic coatings produced by TIG surface melting. Journal of Materials Processing Technology, 2001. 113(1-3): p. 516-520.

[4.15] Buytoz, S., M. Ulutan, and M.M. Yildirim, Dry sliding wear behavior of TIG welding clad WC composite coatings. Applied Surface Science, 2005. 252(5): p. 1313-1323.

[4.16] Mridha, S., Titanium nitride layer formation by TIG surface melting in a reactive environment. Journal of Materials Processing Technology, 2005. 168(3): p. 471-477.

[4.17] Patel, N.S. and R.B. Patel, A review on parametric optimization of TIG welding. International Journal of Computational Engineering Research, 2014. 4(1): p. 27-31.

[4.18] Wang, Y., et al., Microhardness homogeneity analysis of thick amorphous composite coating prepared by TIG cladding. Materials Research Innovations, 2014. 18(sup4): p. S4-787-S4-792.

[4.19] Jasbir Singh, L.T., Surjit Angra, Effect of argon flow rate and standoff distance on the microstructure and wear behaviour of WCCoCr TIG cladding. Journal of Physics, 2019.

[4.20] Kumar, A., R. Kumar Ram, and A. Kumar Das, Mechanical characteristics of Ti-SiC metal matrix composite coating on AISI 304 steel by gas tungsten arc (GTA) coating process. Materials Today: Proceedings, 2019. 17: p. 111-117.

[4.21] Alam, M.S. and A.K. Das, Research Progress in Gas Tungsten Arc Cladding on Steel: A Critical Review, in Recent Advances in Manufacturing Processes and Systems. 2022. p. 859-867.

[4.22] Alam, M.S., Recent Trends in Surface Cladding on AISI 1045 Steel Substrate: A Review, in Functional Materials and Applied Physics. 2022. p. 94-101.

[4.23] Azwan, M., M.A. Maleque, and M.M. Rahman, TIG torch surfacing of metallic materials – a critical review. Transactions of the IMF, 2018. 97(1): p. 12-21.

[4.24] Fande, A.W., R.V. Taiwade, and L. Raut, Development of activated tungsten inert gas welding and its current status: A review. Materials and Manufacturing Processes, 2022. 37(8): p. 841-876.

[4.25] Kumar, A. and A.K. Das, Evolution of microstructure and mechanical properties of Co-SiC tungsten inert gas cladded coating on 304 stainless steel. Engineering Science and Technology, an International Journal, 2021. 24(3): p. 591-604.

[4.26] Juang, S. and Y. Tarng, Process parameter selection for optimizing the weld pool geometry in the tungsten inert gas welding of stainless steel. Journal of materials processing technology, 2002. 122(1): p. 33-37.

[4.27] Jeffus, L., Welding and metal fabrication. 2011: Cengage Learning.

[4.28] Karrar, G., et al., Microstructural characterisation and mechanical properties of dissimilar AA5083-copper joints produced by friction stir welding. Journal of Materials Research and Technology, 2020. 9(5): p. 11968-11979.

[4.29] Sekhar , R., D. Sharma , and P. Shah Intelligent Classification of Tungsten Inert Gas Welding Defects: A Transfer Learning Approach. Frontiers in Mechanical Engineering, 2022. 8.

[4.30] Jiang, S., et al., Study on the Microstructure and Mechanical Properties of Martensitic Wear-Resistant Steel. Crystals, 2023. 13(8).

[4.31] Lacaze, J. and B. Sundman, An assessment of the Fe-C-Si system. Metallurgical Transactions A, 1991. 22: p. 2211-2223.

[4.32] Dutta Majumdar, J., et al., Studies on compositionally graded silicon carbide dispersed composite surface on mild steel developed by laser surface cladding. Journal of Materials Processing Technology, 2008. 203(1-3): p. 505-512.

[4.33] Zhang, C., et al., Fabrication of Ni60–SiC coating on carbon steel for improving friction, corrosion properties. Materials Science and Technology, 2017. 33(4): p. 446-453.

[4.34] Laghavan, V., The carbon-iron-silicon system. J. Alloy Phase Diagrams, India, 1986. 2: p. 97-107.

[4.35] Miettinen, J., Reassessed thermodynamic solution phase data for ternary Fe-Si-C system. Calphad, 1998. 22(2): p. 231-256.

[4.36] Tang, W., et al., The interfacial stability of the coated-SiC/Fe couple. Materials chemistry and physics, 2003. 77(1): p. 236-241.

[4.37] Shin, J.P. and Y.E. Lee, Assessment of Mn-Fe-Si-C Melt in Unified Interaction Parameter Formalism. Metallurgical and Materials Transactions B, 2015. 47(1): p. 216-227.

[4.38] Terry, B. and O. Chinyamakobvu, Assessment of the reaction of SiC powders with iron-based alloys. Journal of materials science, 1993. 28: p. 6779-6784.

[4.39] Srijampan, W., et al., Effects of silicon carbide contents on the microstructure of sintered steels. ScienceAsia, 2021. 47S(1).

[4.40] Zajac, S., V. Schwinn, and K. Tacke. Characterisation and quantification of complex bainitic microstructures in high and ultra-high strength linepipe steels. in Materials Science Forum. 2005. Trans Tech Publ.

[4.41] Caballero, F.G., et al. The microstructure of continuously cooled tough bainitic steels. in 2nd International Conference of Super-High Strength Steels. 2010.

[4.42] Müller, M., et al., Classification of bainitic structures using textural parameters and machine learning techniques. Metals, 2020. 10(5): p. 630.

[4.43] Buytoz, S., Microstructural properties of SiC based hardfacing on low alloy steel. Surface and Coatings Technology, 2006. 200(12-13): p. 3734-3742.

[4.44] Azevedo, S.C. and A.A. de Resende, Effect of angle, distance between electrodes and TIG current on the weld bead geometry in TIG-MIG/MAG welding process. The International Journal of Advanced Manufacturing Technology, 2021. 114(5-6): p. 1505-1515.

[4.45] Shan, Q., et al., Effect of Ni Addition on Microstructure of Matrix in Casting Tungsten Carbide Particle Reinforced Composite. Journal of Materials Science & Technology, 2013. 29(8): p. 720-724.

[4.46] Weng, Z., et al., Wear resistance of diode laser-clad Ni/WC composite coatings at different temperatures. Surface and Coatings Technology, 2016. 304: p. 283-292.

[4.47] Pelleg, J., Reactions in the matrix and interface of the Fe–SiC metal matrix composite system. Materials science and engineering: A, 1999. 269(1-2): p. 225-241.

[4.48] Tang, W., et al., A study of the solid state reaction between silicon carbide and iron. Materials chemistry and physics, 2002. 74(3): p. 258-264.

[4.49] Yuan, J., et al., Effect of the dissolution characteristic of tungsten carbide particles on microstructure and properties of Ni-WC/W2C reinforcement coating manufactured by TIG cladding. International Journal of Refractory Metals and Hard Materials, 2023. 110.

[4.50] Zhang, M., et al., Microstructure and Properties of WC-Reinforced Inconel 718 Alloy Cladding Layer by TIG on Low Carbon Steel Surface. Transactions of the Indian Institute of Metals, 2023. 77(1): p. 219-227.

[4.51] Yuan, Y. and Z. Li, Microstructure and tribology behaviors of in-situ WC/Fe carbide coating fabricated by plasma transferred arc metallurgic reaction. Applied Surface Science, 2017. 423: p. 13-24.

[4.52] Sabzi, M., S.M. Dezfuli, and S.M. Far, Deposition of Ni-tungsten carbide nanocomposite coating by TIG welding: Characterization and control of microstructure and wear/corrosion responses. Ceramics International, 2018. 44(18): p. 22816-22829.

[4.53] Xu, P., D. Zhou, and L. Li, Fiber laser welding of WC-Co and carbon steel dissimilar materials. Weld. J, 2017. 96(1): p. 1-10.

[4.54] Lin, M.J., et al., Rapid crystal growth kinetics of tungsten dendrites under electrostatic levitation state. Chemical Physics Letters, 2022. 803.

[4.55] Quyen, H.T.N., P.M. Khanh, and N.H. Hai, Effect of Cobalt Addition on the Evolution of Austenite and ε-Martensitic Transformation during Loading of 201 Stainless Steel. Journal of Materials Engineering and Performance, 2023. 33(17): p. 8972-8982.

[4.56] Wang, Z., et al., Effect of molybdenum addition on the precipitation of carbides in the austenite matrix of titanium micro-alloyed steels. Journal of Materials Science, 2016. 51(10): p. 4996-5007.

[4.57] Sarmah, P. and K. Gupta, Recent Advancements in Fabrication of Metal Matrix Composites: A Systematic Review. Materials (Basel), 2024. 17(18).

[4.58] Dossett, J. and G.E. Totten, ASM handbook. volume 4A, Steel Heat Treating Fundamentals and Processes, ASM, 2013.

[4.59] Yang, J., et al., Microstructure and magnetic properties of NiCrMoAl/WC coatings by laser cladding: Effect of WC metallurgical behaviors. Surface and Coatings Technology, 2018. 350: p. 110-118.

[4.60] Yang, J., et al., Influence of Mn additions on the microstructure and magnetic properties of FeNiCr/60% WC composite coating produced by laser cladding. International Journal of Refractory Metals and Hard Materials, 2014. 46: p. 58-64.

[4.61] Wang, Y., et al., Microstructure and property of tungsten carbide particulate reinforced wear resistant coating by TIG cladding. International Journal of Refractory Metals and Hard Materials, 2021. 100.

[4.62] Bartkowski, D., et al., Microstructure, microhardness and corrosion resistance of Stellite-6 coatings reinforced with WC particles using laser cladding. Optics & Laser Technology, 2015. 68: p. 191-201.

[4.63] Li, J., et al., A comparative study on microstructure evolution and wear resistance of different-sized tungsten carbide modified Fe-based laser cladding coatings. Optics & Laser Technology, 2022. 147.

Chapter 5. Sliding wear behaviour of MMC overlays deposited using tubular filler

5.1 Introduction

As established in Chapter 4, the 316LSS-T tubular filler was selected for embedding ceramic reinforcements such as SiC and WC10%Co based on its proven ability to retain ceramic reinforcements with minimal dissolution during deposition and ensuring metallurgical bonding. Optimal filler dimensions were identified as 4 mm OD and 3 mm ID (1 mm wall thickness), and the welding parameters were manually optimised for uniform deposition.

In this chapter, LCS-BM and 316LSS-BM discs with 1 mm deep grooves described in chapter 3 (section 3.2.1.1) Figure 3.1, were produced to simulate localised wear. These grooves were refilled by depositing 316LSS-T fillers separately containing SiC and WC10%Co particles. A commercial hard-facing electrode HF600 was also evaluated as a comparison. The post deposition surfaces were ground smooth and wear tested using a pin-on-disc setup under varying loading conditions. [5.1-5.3].

5.2 Experimental procedure

To accurately evaluate the enhancement in wear resistance achieved through the MMC weld deposit, it was essential first to establish the baseline wear performance of the unmodified base metals. Therefore, the sliding wear behaviour of LCS-BM and 316LSS-BM against CI pin was systematically examined. This provided a critical reference point for assessing the MMC deposits' effectiveness and suitability for wear-intensive applications. All the combinations of materials, testing conditions and parameters are reported in chapter 3 (section3.2.1.2).

All specimen discs were fabricated with dimensions described in chapter 3 (section 3.2.2.2), Figure 3.1. The CI pin material characteristics and chemical composition described in chapter 3 (section 3.2.1.2.1). For each load condition, three samples were fabricated using the

parameters listed in Table 3.5 to ensure repeatability, and the average of the measurements was used for analysis. In ambient laboratory conditions, all the tests were performed, and the sample material loss was measured by an analytical balance accurate to 0.0001g. The wear performance was examined following the procedure of ASTM G99 using the dry pin-on-disc sliding wear method [5.4]. Steps of the standard procedure are described in chapter 3, (section 3.2,1,2). SEM and EDS were used to analyse the wear scars and characterise the damage on the worn surface.

5.3 Results and discussion

5.3.1 Sliding wear performance of 316LSS-BM disc

5.3.1.1 Material loss

For the 316LSS-BM discs as shown in Figure 5.1, the material loss began at approximately 0.026 g at 2 Kg, increased to 0.032 g at 4 Kg, and exhibited a significant rise to nearly 0.085 g at 6 Kg. As expected, this trend showed that as the load increases, the wear mechanism intensifies, due to increased surface interactions and material deformation, which has been similarly observed in previous studies on wear behaviour in stainless steel alloys [5.6]. Under moderate loading conditions 316LSS-BM exhibited nearly stable behaviour, but its response

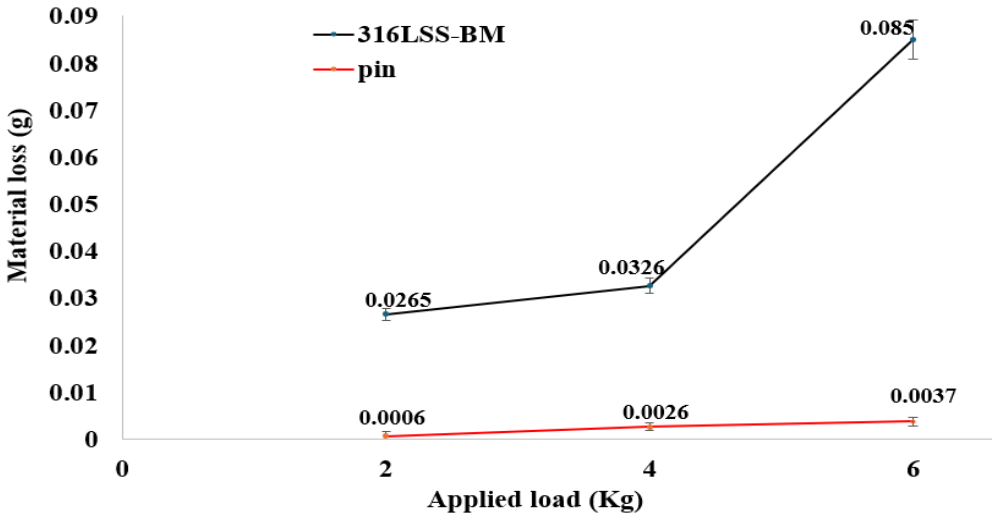

Figure 5.1. Material loss of unreinforced 316LSS-BM and CI pin

changed sharply at 6 Kg load due to microstructural alterations and phase transformation induced by intense sliding [5.7-5.9].

5.3.1.2 Surface wear morphology at 2 Kg load

Figure 5.2 presents the surface morphology of the 316LSS-BM disc subjected to a 2 Kg load during sliding wear testing. The image distinctly highlights the unworn surface and the worn surface separated by a dashed line boundary. The unworn region is a relevant given that the CI pin did not make contact in this region. In contrast, the worn region exhibits significant surface damage, including rough textures, and smearing. Severe plastic deformation (SPD) occurs during sliding contact, and the material has been stretched, compressed, or smeared beyond its elastic limit without fracturing. Such deformation confirms that the wear process involved plastic yielding rather than brittle fracture. The deformation pattern in the SEM image also supports previous findings that sliding wear in ductile materials is influenced by load intensity and surface hardness of the counter face [5.10-5.16]. The transition to more aggressive wear

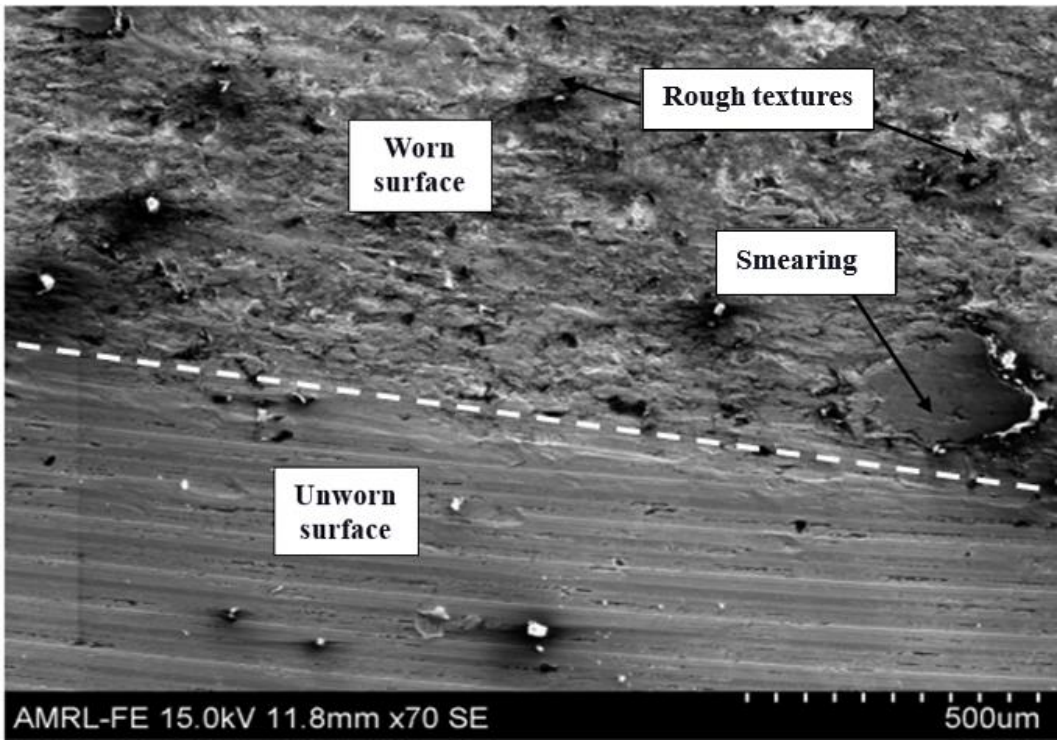

Figure 5.2 – SEM micrograph of unreinforced 316lSS-BM disc at 2 Kg load

modes occurs at higher loads correlating with the sharp increase in material loss observed in weight loss measurements.

5.3.1.3 Surface wear morphology at 4 Kg load

Figure 5.3 displays the worn surface morphology of the 316LSS-BM tested under a 4 kg load. The surface reveals SPD, with extensive flow lines, grooves, and depressions indicating material displacement and removal. Several flattened regions can be observed, suggesting zones of intense adhesive interaction where the material has undergone repeated plastic shearing. These flattened zones, formed under high contact pressure, indicate localised work hardening due to continuous sliding. Additionally, the visible surface features suggest the possibility of friction-induced microstructural changes, such as strain-induced martensite formation, which may increase local hardness but could also contribute to surface embrittlement under prolonged loading [5.6, 5.17].

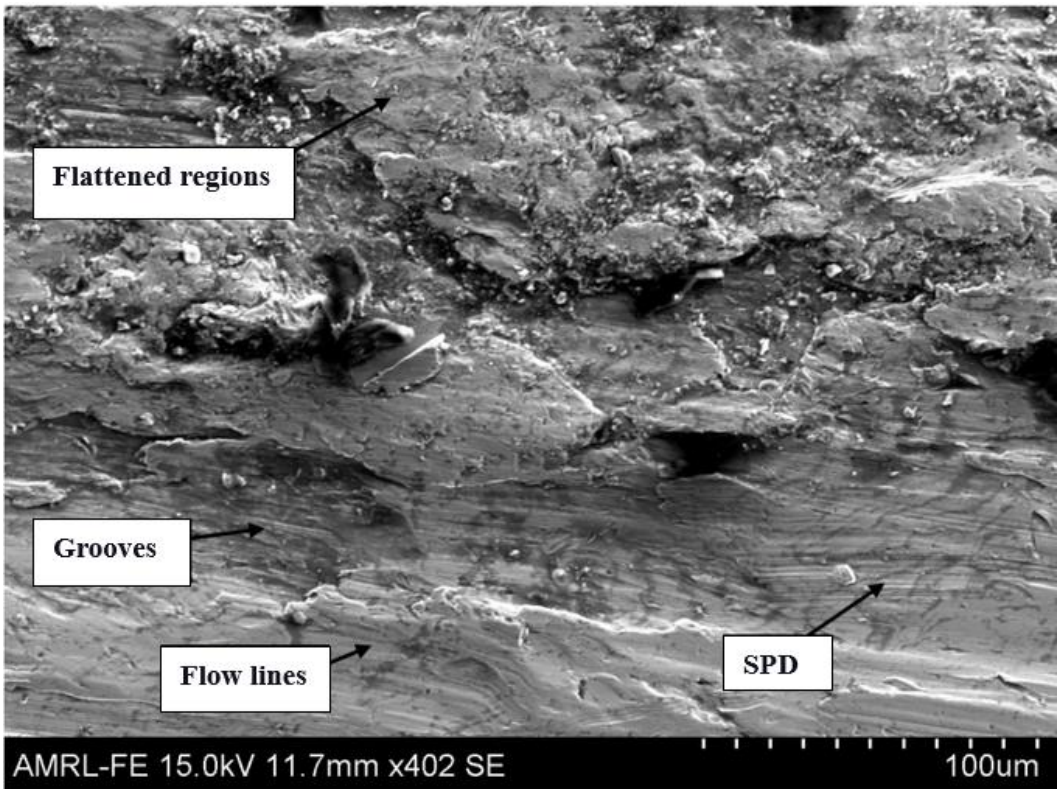

Figure 5.3 - SEM micrograph of unreinforced 316LSS-BM disc at 4 Kg load

5.3.1.4 Surface wear morphology at 6 Kg load

Figure 5.4 shows the worn surface morphology at high magnification, revealing a network of interconnected surface cracks and flake-like regions indicative of surface embrittlement. The fragmented appearance suggests fatigue-driven delamination, likely resulting from repeated sliding and subsurface crack propagation. Fine debris and adhered particles further support a combination of oxidative wear and brittle fracture, possibly linked to strain-induced hardening or phase transformation during sliding [5.18].

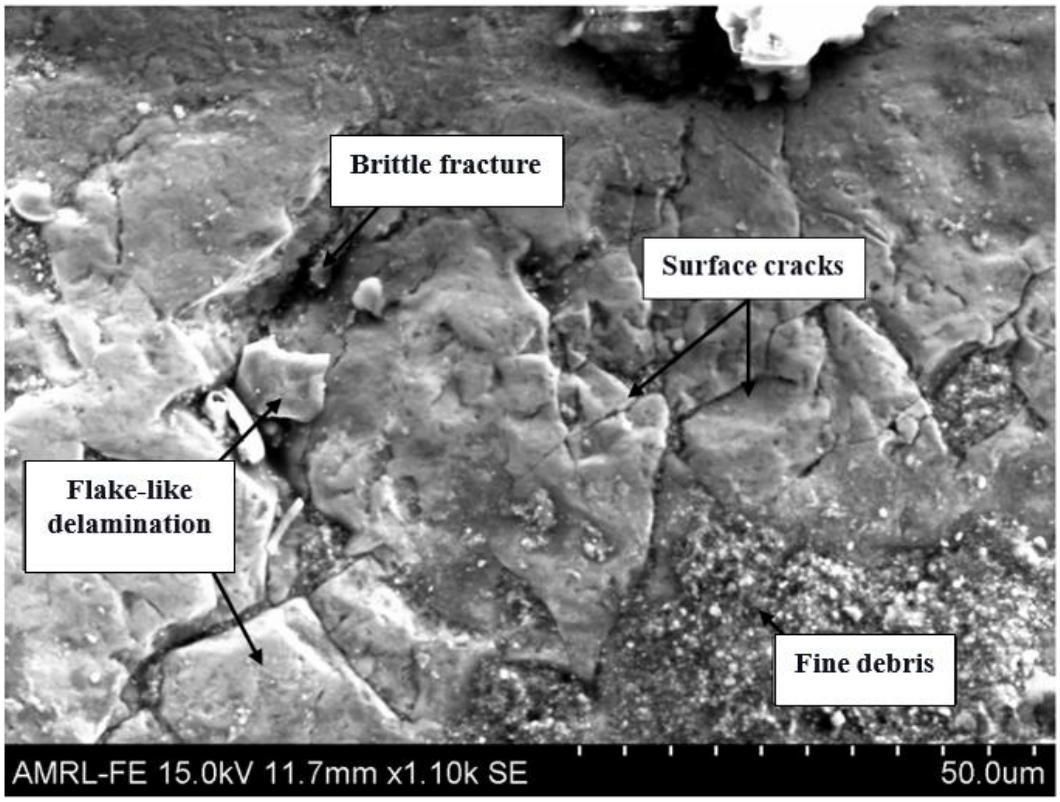

Figure 5.4 – SEM micrograph of unreinforced 316LSS-BM at 6 Kg load

5.3.2 Sliding wear performance of 316LSS-BM disc reinforced with HF600 hard-facing electrode.

5.3.2.1 Material loss

The line graph in Figure. 5.5 illustrates the material loss as a function of applied load for the worn pair consisting of a 316LSS-BM disc reinforced with the HF600 hard-facing electrode and a CI pin. The wear behaviour of these materials is distinct, emphasising the superior performance of the HF600 hard-faced surface compared to CI. As detailed in Chapter 4, the HF600 hard-facing electrode consists of a complex carbide-reinforced microstructure, primarily composed of Cr-rich carbides Cr_7C_3 and $Cr_{23}C_6$ embedded within a martensitic matrix. These hard carbides act as wear-resistant phases, effectively countering abrasive and adhesive wear mechanisms during sliding contact.

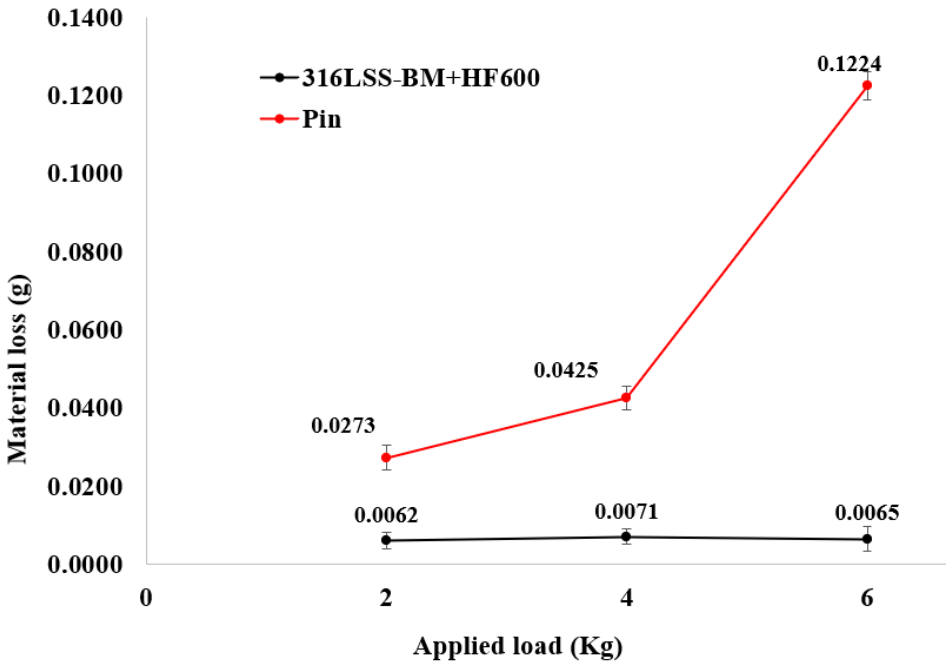

Figure 5.5 Material loss of 316LSS-BM disc reinforced with HF600 and CI pin

5.3.2.2 Surface wear morphology at 2 Kg load

At 2 kg load, Figure 5.6 reveals distinct regions of worn and unworn surfaces. The worn surface, with a thin brown layer, exhibits minimal deformation. This oxide layer has been partially removed in certain areas, revealing the bright underlying metallic surface. The limited material loss at this stage, as observed in the material loss study, suggests that the HF600- effectively resists wear, preventing severe plastic deformation. This observation aligns with findings in the literature [5.14, 5.15] indicating that oxide layers form during sliding wear due to localised temperature rise and material transfer processes. They act as a protective tribo-film that mitigates wear progression. The presence of this layer helps reduce direct metal-to-metal contact, thereby reducing material loss.

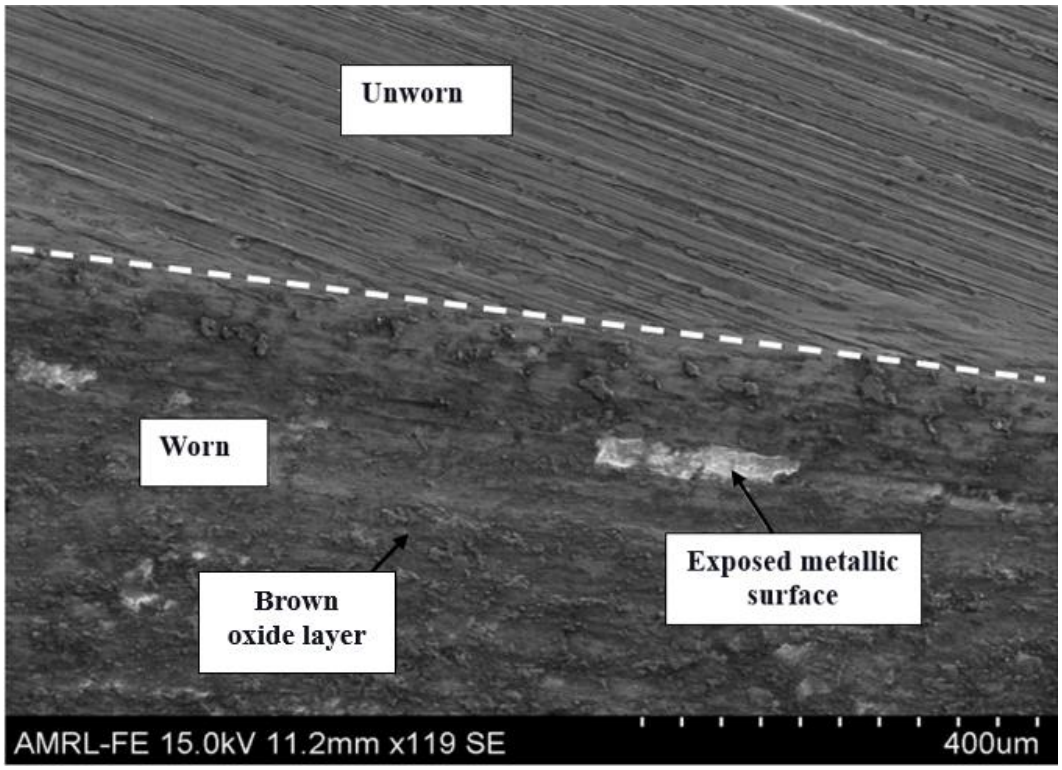

Figure 5.6 – SEM micrograph of 316LSS-BM disc reinforced with HF600 at 2 Kg load

5.3.2.3 Surface wear morphology at 4 Kg load

At an increased load of 4 kg, Figure 5.7 reveals a more pronounced oxide layer, with adherence of islands filling surface voids. These oxide formations result from progressive material transfer from the CI onto the HF600-treated disc during sliding. The material transfer and subsequent compaction lead to the formation a composite structure consisting of oxides, and wear debris [5.16]. Despite the higher load, the material loss remains negligible, indicating that the HF600 overlay provides adequate wear protection. This aligns with the low wear rates observed in material loss at this stage.

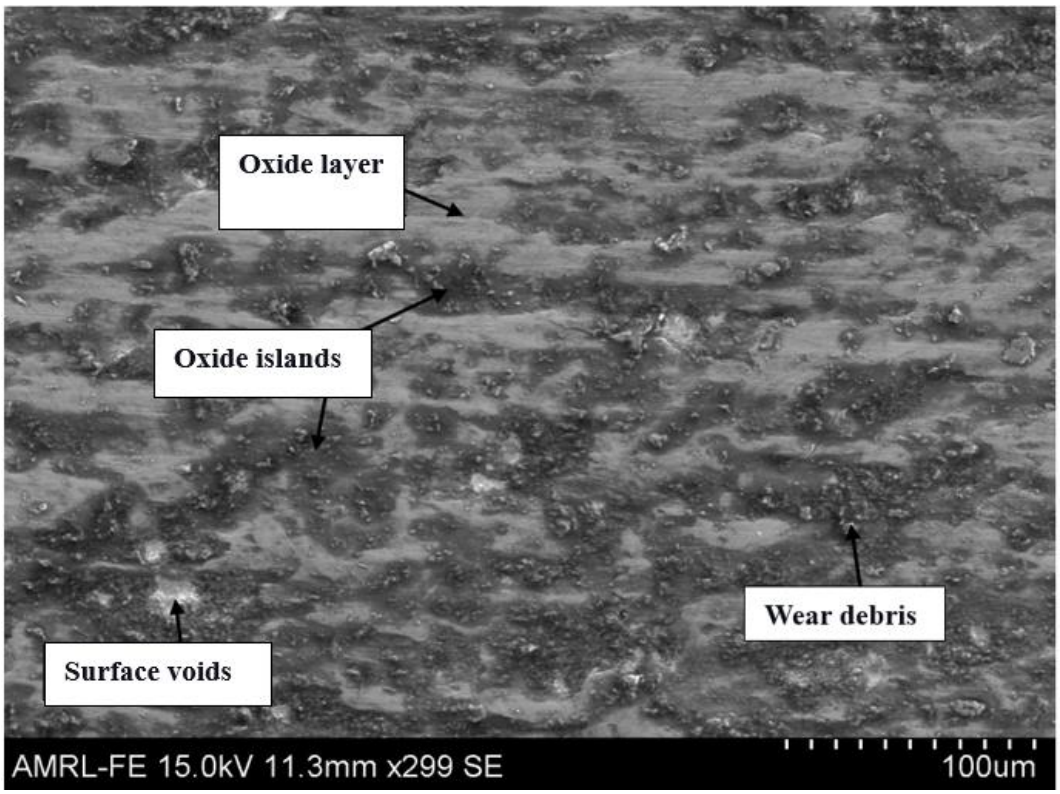

Figure 5.7- SEM micrograph of 316LSS-BM disc reinforced with HF600 disc at 4 Kg load

5.3.2.4 Surface wear morphology at 6 Kg load

The image shows a relatively smoother worn surface compared to the base metal, with parallel abrasion marks, oxidised debris, and localised surface deposits. The linear wear grooves indicate dominant abrasive wear, formed by hard asperities or particles sliding across the surface. The darkened patches suggest the presence of oxidation layers or tribolayers, formed

due to high-temperature frictional conditions. Scattered fine debris particles across the surface point to material loss and transfer, partially retained by the surface film.

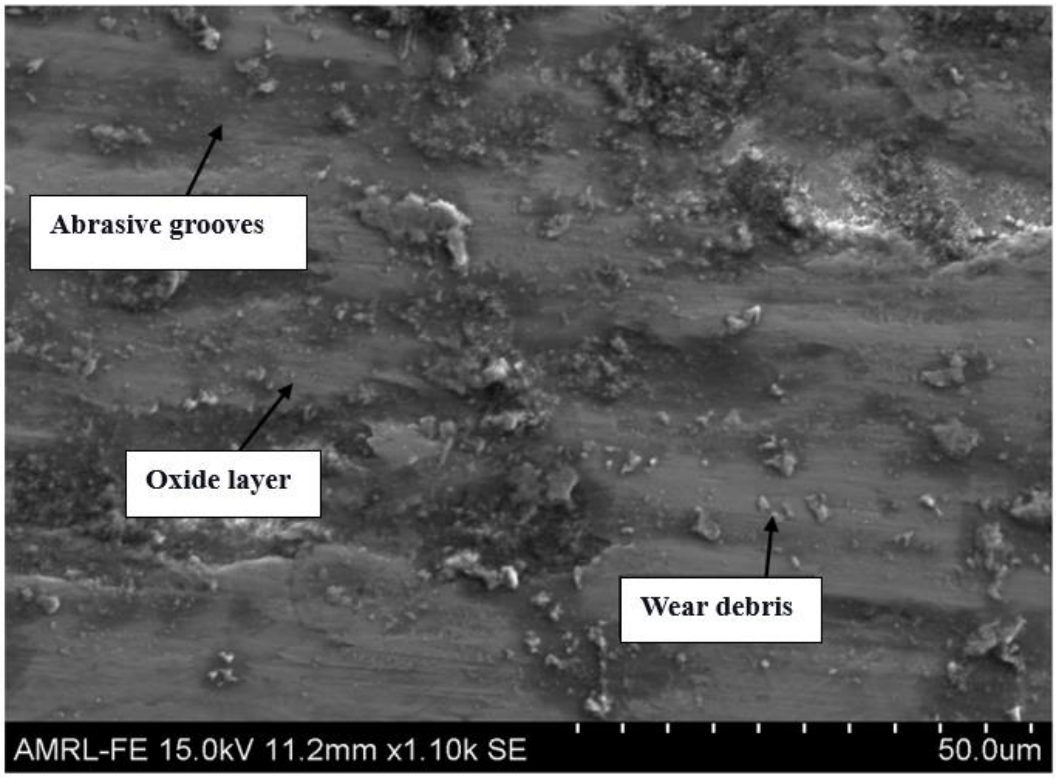

Figure 5.8 - SEM micrograph of 316LSS-BM disc reinforced with HF600 at 6 Kg load

5.3.3 Sliding wear performance of 316LSS-BM disc reinforced with SiC

5.3.3.1 Material loss

The results in Figure 5.9 indicate that the 316LSS-BM disc reinforced with SiC particles exhibited significantly improved wear resistance compared to the CI across the applied load range (2–6 kg). The material loss of the SiC-reinforced composite remained consistently lower, highlighting the effectiveness of SiC as a reinforcement phase in reducing wear. The steel matrix provides toughness, while the embedded SiC particles, provide exceptional hardness and wear resistance, enhancing the overall tribological performance of the composite. However, at higher loads 6 kg, the CI pin experienced a sharp increase in material loss.

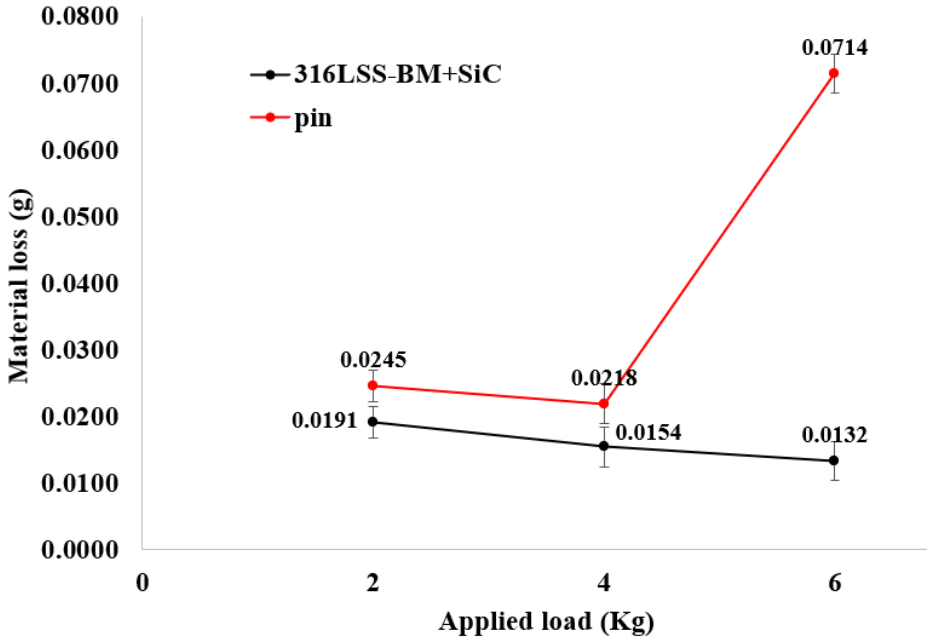

Figure 5.9 material loss of 316LSS-BM disc reinforced with SiC and CI pin

5.3.3.2 Surface wear morphology at 2 Kg load

Figure 5.10 reveals a wear characterised by shallow micro-scratches and minimal penetration, indicating the protective effect of the SiC particles within the ductile steel matrix. The valleys of the machined surface appear flattened and plastically deformed in the sliding direction. This suggests that the SiC reinforcements effectively resisted abrasive forces, distributing the applied load across the surface and minimising severe material removal. Studies have reported similar observations where ceramic reinforcements improve the wear resistance of MMC by reducing penetration depth and hindering abrasive wear mechanisms [5.14, 5.17]. The presence of SiC particles limits direct contact between the steel matrix and the counter-face, thereby preventing excessive plastic deformation.

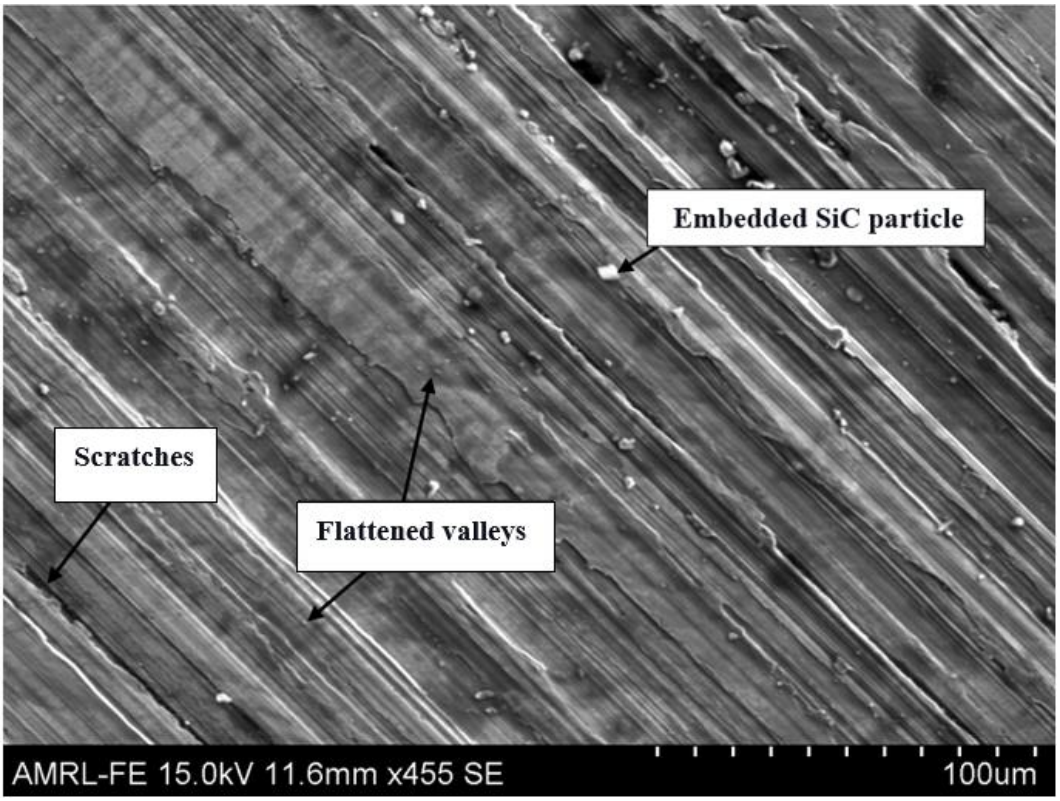

Figure 5.10 - SEM micrograph of 316LSS-BM disc reinforced with SiC at 2 Kg load

5.3.3.3 Surface wear morphology at 4 Kg load

At 4 kg load, the SEM image Figure 5.11 reveals a more pronounced wear, with deeper scratches and increased wear debris formation. This transition indicates a shift toward more aggressive wear mechanisms, due to higher contact pressures and the accumulation of detached wear debris from the CI pin. The increased debris formation suggests that third body wear interactions have become more dominant. The presence of wear debris trapped between the sliding interfaces might have led to micro-cutting and additional grooving, but the SiC reinforcement effectively delayed severe material loss.

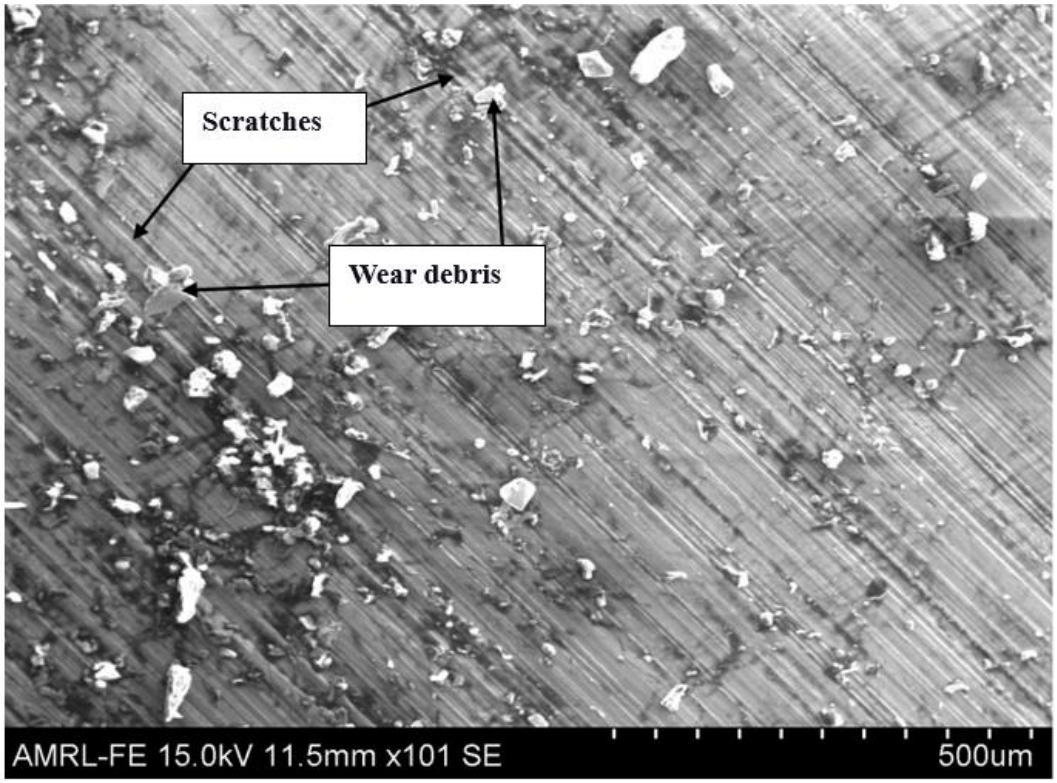

Figure 5.11 – SEM micrograph of 316LSS-BM disc reinforced with SiC at 4 Kg load

5.3.3.4 Surface wear morphology at 6 Kg load

At a 6 kg load, the SEM image Figure 5.12 shows significant surface damage, with deeper grooves, scratches, and extensive wear debris formation. The hard SiC particles within the matrix continued to provide localised reinforcement. However, the steel matrix exhibited more pronounced damage, suggesting that the protective effect of SiC becomes less effective under extreme loading conditions. This behaviour is consistent with findings in wear studies of MMC, where increased loads lead to more severe abrasive and adhesive wear mechanisms due to the accumulation of wear debris, and increased contact pressure [5.18].

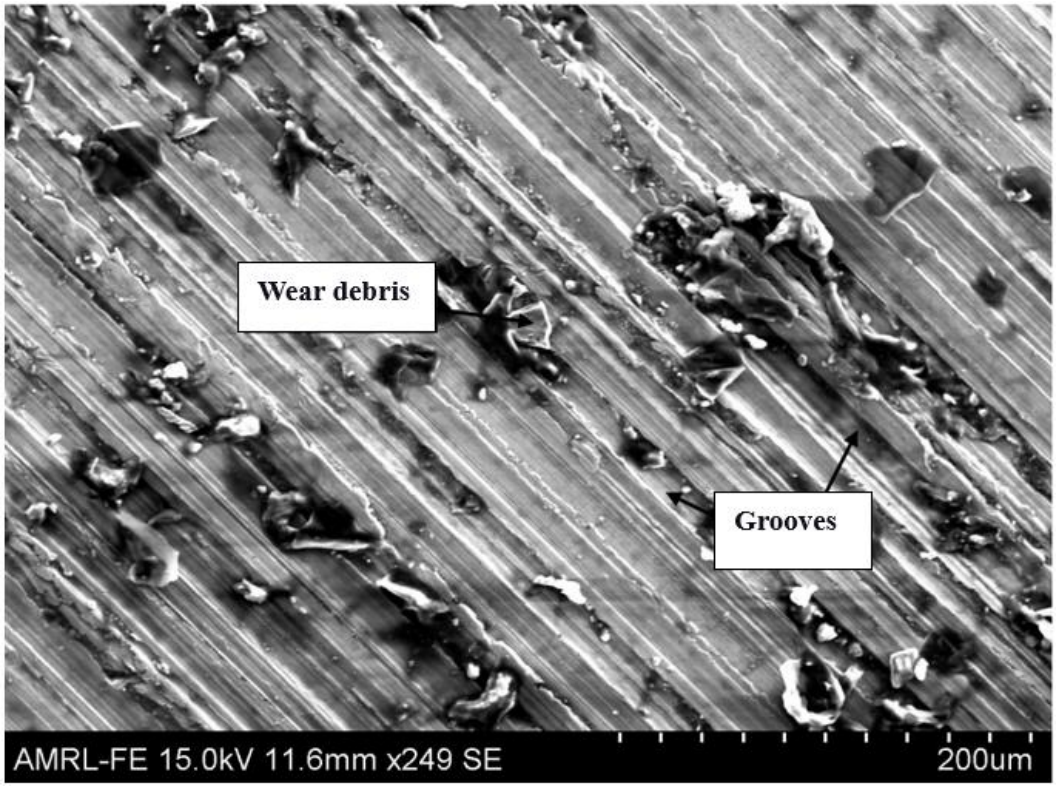

Figure 5.12 - SEM micrograph of 316LSS-BM disc reinforced with SiC at 6 Kg load

5.3.4 Sliding wear performance of 316LSS-BM disc reinforced with WC10%Co

5.3.4.1 Material loss

The results in Figure 5.13 demonstrate that the 316LSS-BM disc reinforced with WC-10%Co exhibited exceptional wear resistance compared to the CI pin. While the material loss of the composite remained consistently low across all applied loads, an interesting trend was observed at 6 kg, where the material loss of the disc decreased compared to the 4 kg load. This reduction in wear may be attributed to the formation and stabilisation of a protective layer on the disc surface under higher loads, which reduced further material removal. Additionally, the Co binder in the WC-10%Co composite contributed to the enhanced toughness and load capacity of the matrix, maintaining the structural integrity of the treated disc even under severe sliding wear conditions [5.19]. This highlights the superior performance of WC-10%Co

reinforcements in mitigating wear while preserving mechanical stability under elevated contact stresses.

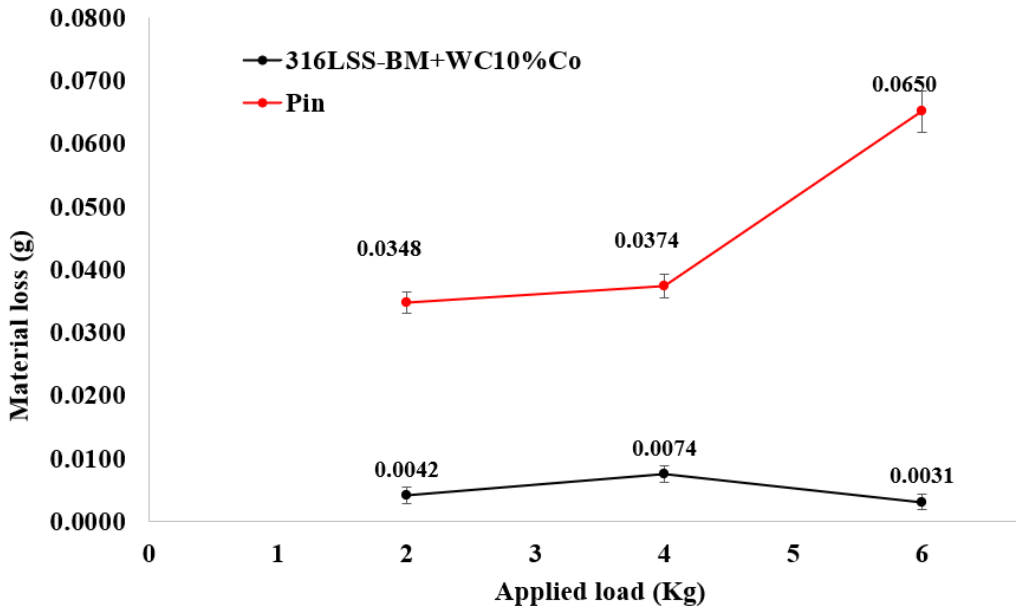

Figure 5.13 Material loss of 316LSS-BM disc reinforced with WC10%Co and CI pin

5.3.4.2 Surface wear morphology at 2 Kg load

At 2 kg load, Figure 5.14 reveals a worn surface that remained largely unaffected, with only minor micro-scratches and a formation of scattered brown islands. This indicates limited material removal, as the high hardness of WC particles effectively resisted penetration and abrasive wear. The minimal wear at this stage supports the low material loss values observed in the material loss measurements. It confirms the superior hardness and wear resistance of the WC reinforcement phase.

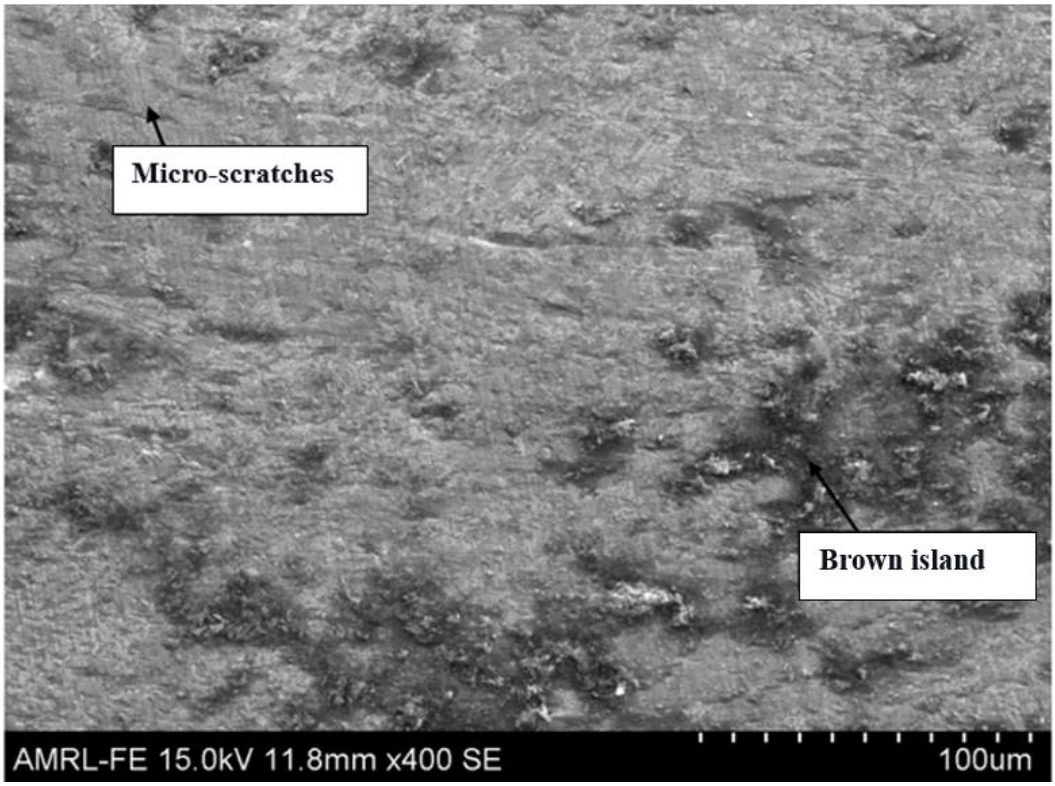

Figure 5.14 - SEM micrograph of 316LSS-BM disc reinforced with WC10%Co at 2 Kg load

5.3.4.3 Surface wear morphology at 4 Kg load

At 4 kg load, the worn surface morphology as shown in Figure 5.15 changes, with increased formation of a brown layer covering the surface. While the MMC surface remained largely unaffected, localised detachment of the brown oxide layer exposed the bright underlying metal, indicating a dynamic process of formation and removal due to increased load.

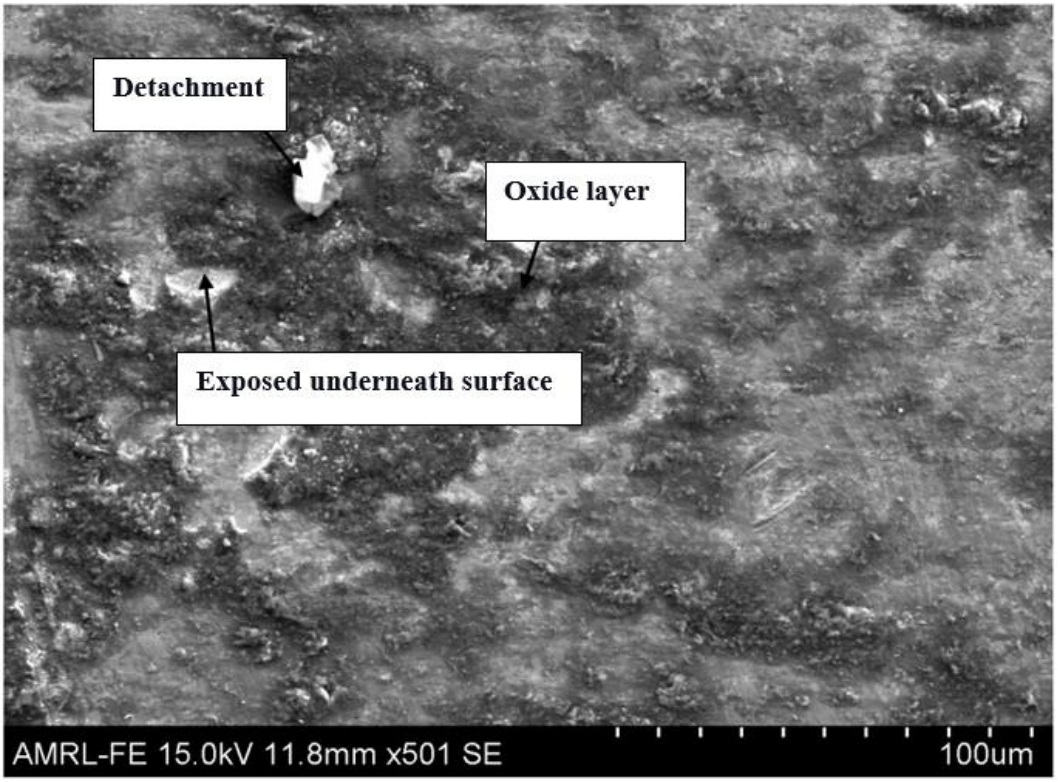

Figure 5.15 - SEM micrograph of 316LSS-BM disc reinforced with WC10%Co at 4 Kg load

5.3.4.4 Surface wear morphology at 6 Kg load

At a 6 kg load, Figure 5.16 shows no significant differences in surface morphology compared to the 4 kg condition. However, the reduction in material loss at 6 kg, could be contributed to the formation of friction layer [5.18], which indicate that oxide layers formed during sliding wear can serve as protective films, reducing wear rates by acting as lubricating and load-bearing layers. The embedded WC particles and the Co binder also contribute to this enhanced wear resistance, ensuring that the substrate surface maintains superior performance even under severe loading conditions.

Figure 5.16 - SEM micrograph of 316LSS-BM disc reinforced with WC10%Co at 6 Kg load

5.3.5 Sliding wear performance of LCS-BM disc

5.3.5.1 Material loss

The wear response of the LCS-BM disc in figure 5.17 demonstrates a notable load-dependent behaviour. At an applied load of 2 kg, the material experienced significant mass loss, exceeding 0.23 g, indicating severe wear dominated by adhesive and micro-cutting mechanisms, as the applied load increased to 4 kg, material loss sharply dropped to approximately 0.05 g, suggesting a transition in the wear mechanism. This reduction may be attributed to forming a compacted friction layer or strain-induced surface hardening that stabilised the contact surface and resisted further wear. At 6 kg, the material loss further decreased to below 0.02g. These observations indicate that, under increased loading, the LCS-BM surface undergoes beneficial microstructural or mechanical changes that enhance its resistance to material removal.

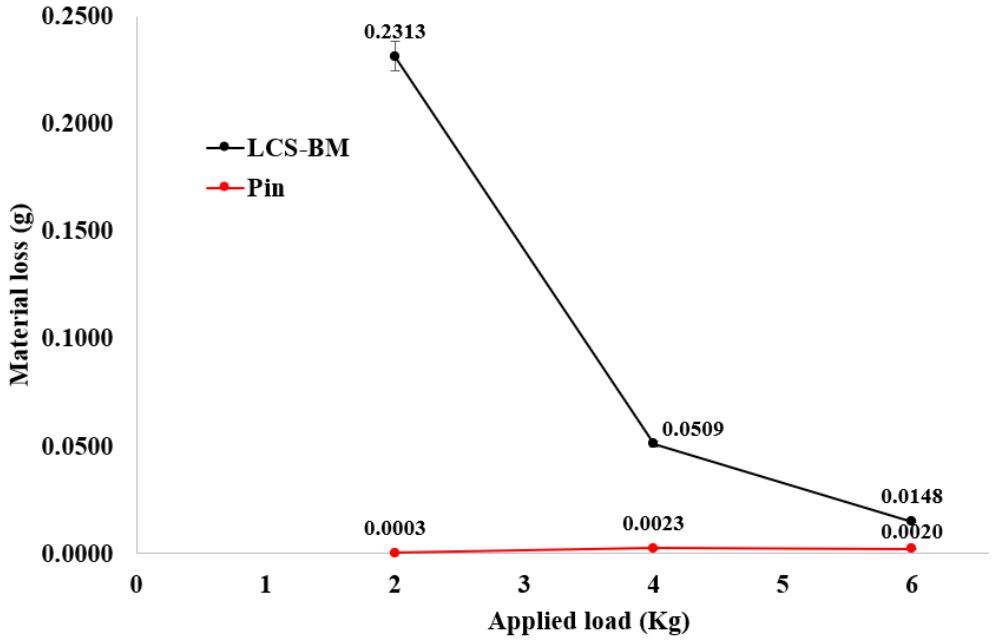

Figure 5.17 Material loss of unreinforced LCS-BM disc and CI pin

5.3.5.2 Surface wear morphology at 2 Kg load

At a 2 kg load, the LCS-BM disc exhibited significant material loss, whereas the CI pin experienced minimal wear. This outcome can be attributed to the abrasive action of hard asperities of CI pin, which ploughed into the softer LCS material, causing substantial material removal as shown in Figure 5.18. The detached material from the LCS surface escaped from the mating surface, intensifying wear on the disc while leaving the pin relatively unaffected. This mechanism aligns with previous studies on tribological behaviour, where the harder counter-face initiates higher material removal rates in the softer material under low-load conditions [5.6, 5.19-5.21].

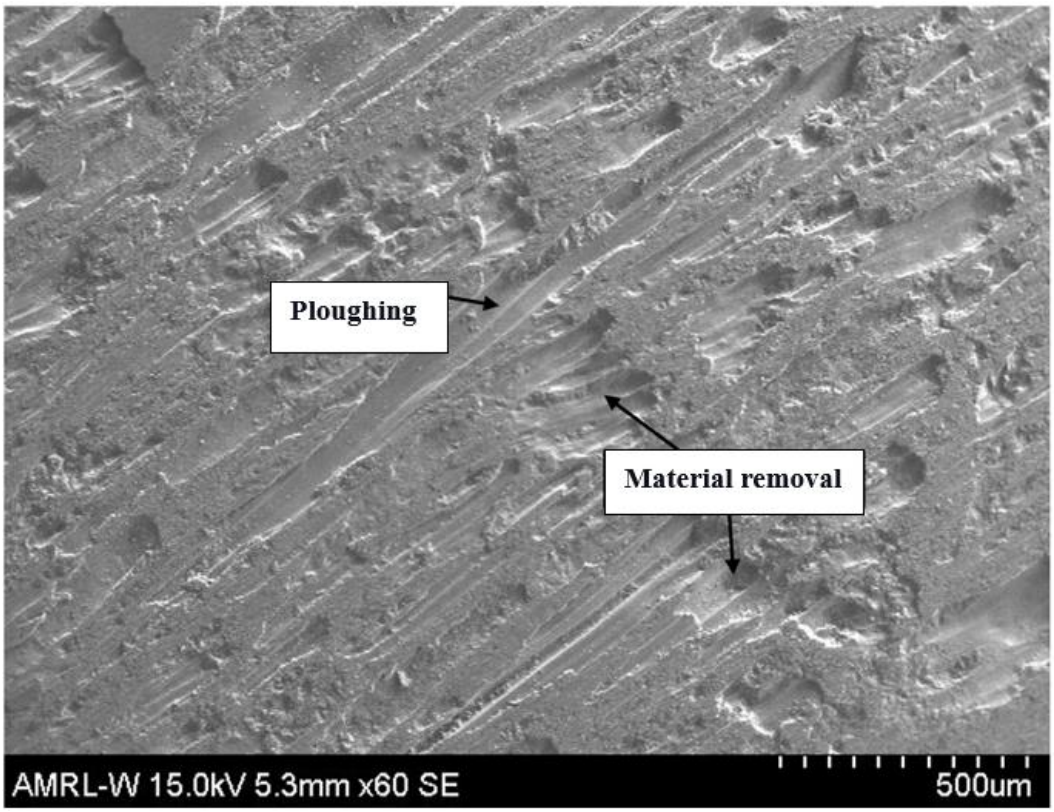

Figure 5.18 – SEM micrograph of unreinforced LCS-BM disc at 2 Kg load

5.3.5.3 Surface wear morphology at 4 Kg load

At a 4 kg load, the material loss of the LCS-BM disc as shown in Figure 5.19 decreased. The following processes contributed to the reduced wear rate of the LCS-BM disc. Although wear was still present, a solid-state work hardening induced by friction and increased loading [5.9] slowed the material removal rate from the LCS-BM disc. However, this change in wear behaviour also impacted the counter-face, leading to increased material loss from the CI pin.

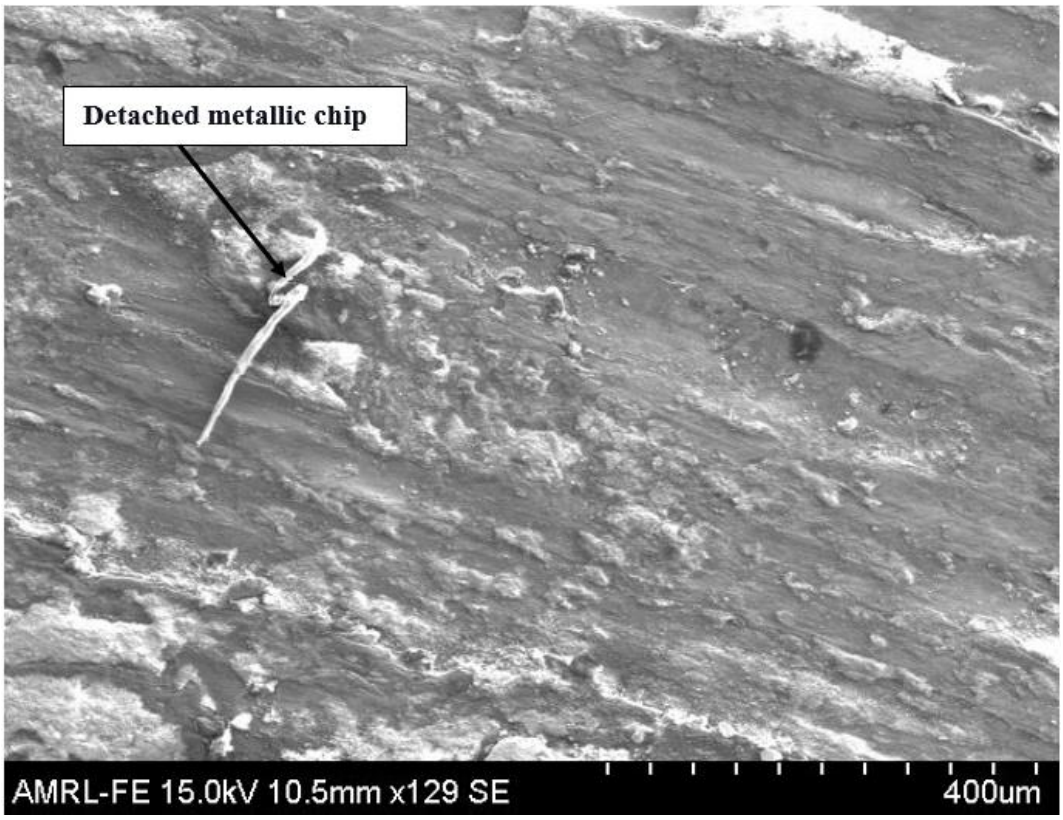

Figure 5.19 – SEM micrograph of unreinforced LCS-BM disc at 4 Kg load

5.3.5.4 Surface wear morphology at 6 Kg load

At a 6 kg load, the wear rate of the LCS-BM disc continued to decrease while the material loss of the CI pin increased sharply. The results highlight the dynamic nature of wear transformations in LCS-BM under increasing loads. Initially, established material loss occurs at lower loads, but with increasing load, strain hardening, oxidation, debris compaction and adhesion, and friction layer formation lead to improved wear resistance.

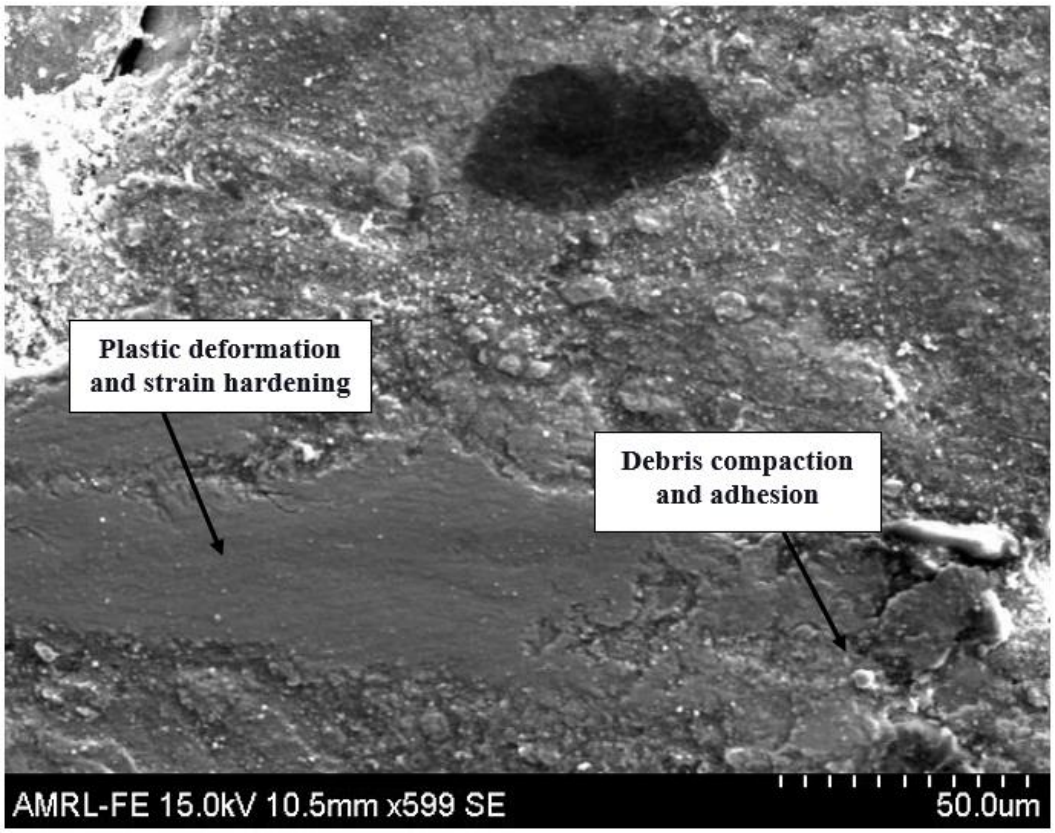

Figure 5.20 – SEM micrograph of unreinforced LCS-BM disc at 6 Kg load

5.3.6 Sliding wear performance of LCS-BM disc reinforced with HF600 electrode

5.3.6.1 Material loss

The wear behaviour of the LCS-BM+HF600 in Figure 5.21 reveals remarkable stability across the tested load range. At 2 kg, the material exhibits minimal wear, 0.0046 g, increasing to 0.0075 g at 4 kg. Interestingly, at 6 kg, the material loss slightly declines 0.0049 g, indicating the deposit's consistent performance even under elevated mechanical stress. The relatively flat wear profile across increasing loads indicates that the hard surfacing resists transitions into more severe wear regimes due to hard carbide phases such as chromium carbides.

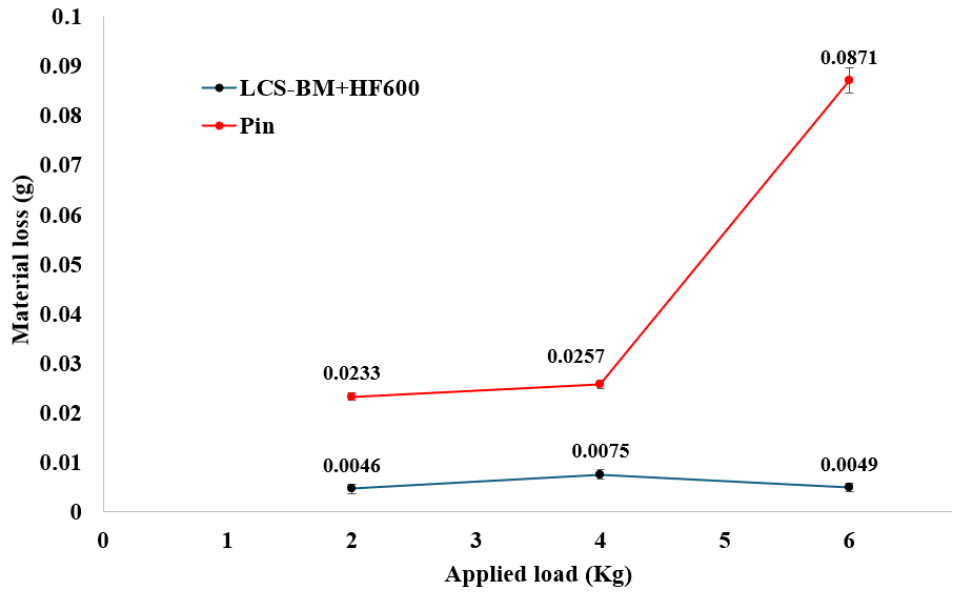

Figure 5.21 Material loss of LCS-BM disc reinforced with HF600 disc and CI pin

5.3.6.2 Surface wear morphology at 2 Kg load

At 2 kg load, the Figure 5.22 reveals characteristic wear patterns, including:

- Visible scratches indicate abrasive interactions with the opposing surface.
- Ploughing behaviour is a sign of localised material displacement and accumulation.
- Brittle wear mechanisms, suggesting fracturing-induced material removal.

The formation of scratches suggests that hard asperities or debris were dragged across the surface, leading to abrasive wear. The presence of detached debris on the surface highlights the continuous detachment of wear particles, which may further intensify material removal through third-body abrasion mechanisms. These findings align with previous studies on abrasive and adhesive wear mechanisms observed in hard-facing coatings under low-load conditions [5.17, 5.20].

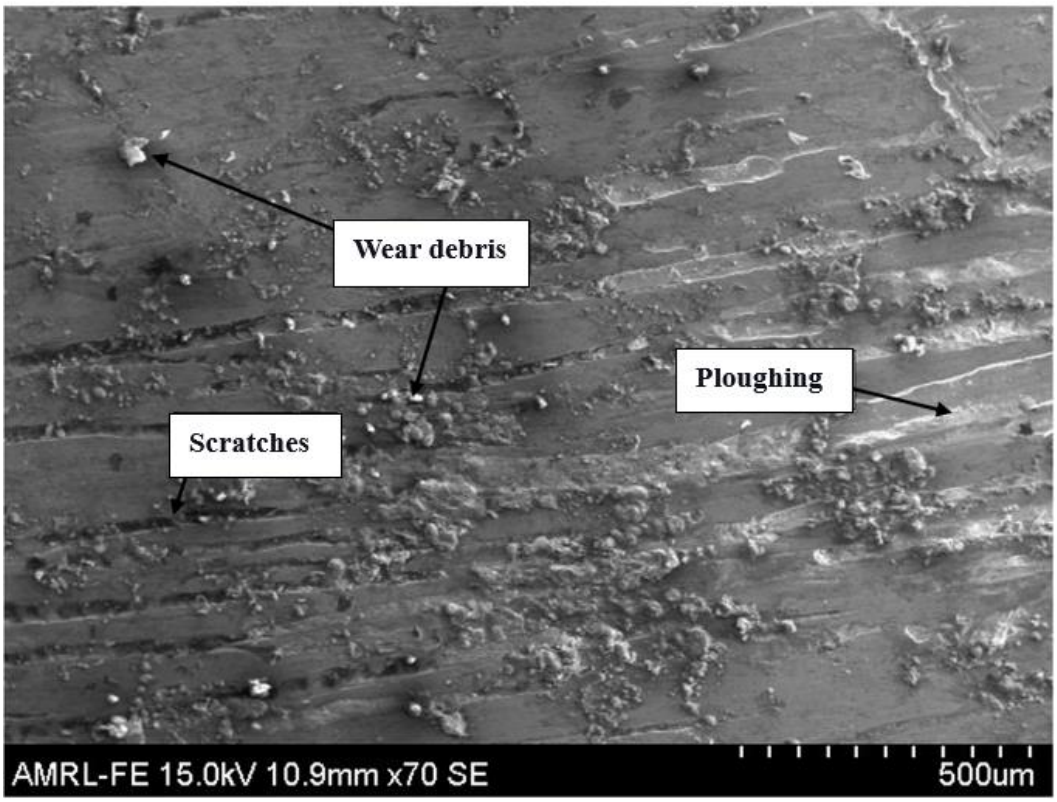

Figure 5.22 - SEM micrograph of LCS-BM disc reinforced with HF600 at 2 Kg load

5.3.6.3 Surface wear morphology at 4 Kg load

At 4 kg load, Figure 5.23 shows significant wear progression, characterised by ploughing, Spallation, and Formation of third-body particles. intensifying wear severity. These third-body effects increase wear rates by accelerating mechanical interactions between the opposing surfaces. Despite these wear mechanisms, the HF600-treated surface still exhibited significantly lower material loss than the CI, demonstrating the superior wear resistance given by its martensitic microstructure. These findings align with other research indicating that martensitic microstructures enhance wear resistance under abrasive and adhesive conditions [5.21, 5.22].

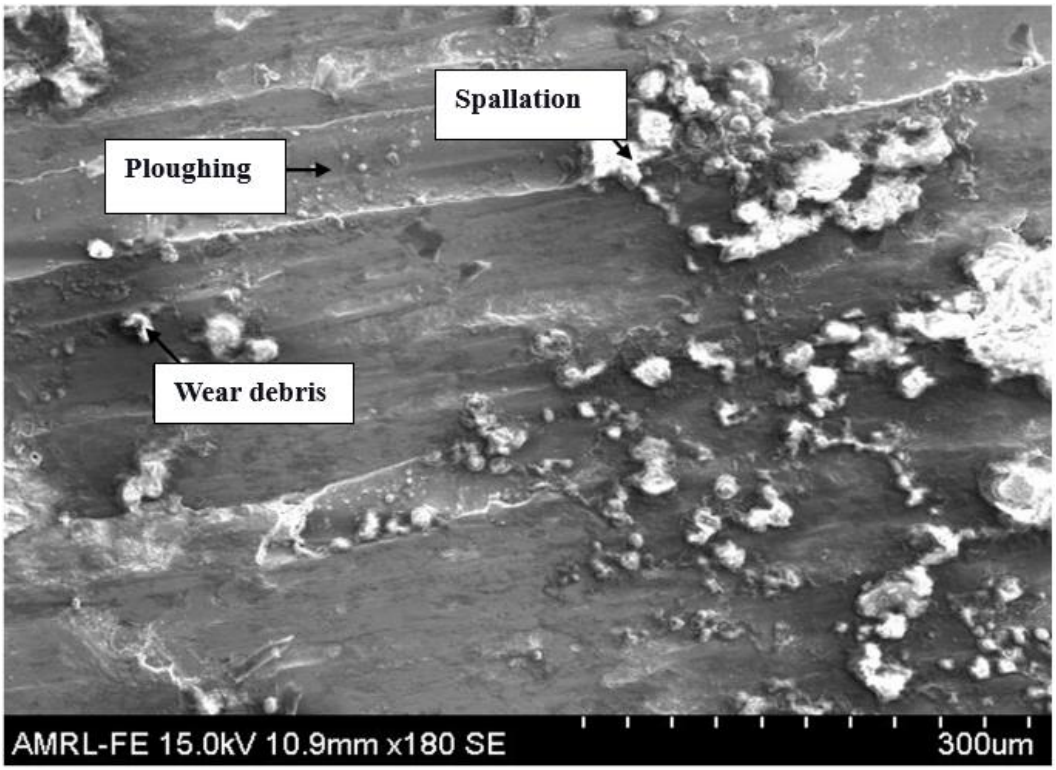

Figure 5.23 - SEM micrograph of LCS-BM disc reinforced with HF600 at 4 Kg load

5.3.6.4 Surface wear morphology at 6 Kg load

At 6 kg load, Figure 5.24 reveals a pronounced tribological response characterised by formation of wear debris, brittle ploughing behaviour, micro-cracks and fractures. Micro-cracks and fractures suggest excessive stress accumulation, leading to debris detachment and the generation of third-body abrasive particles. These particles become trapped between the rubbing surfaces, further accelerating material removal through micro-fracturing and abrasive ploughing. The deposited material exhibits high wear resistance. However, the evolution of stress-induced fractures and third-body interactions at extreme loads suggests that further modifications may be necessary to enhance its long-term performance in high-load applications.

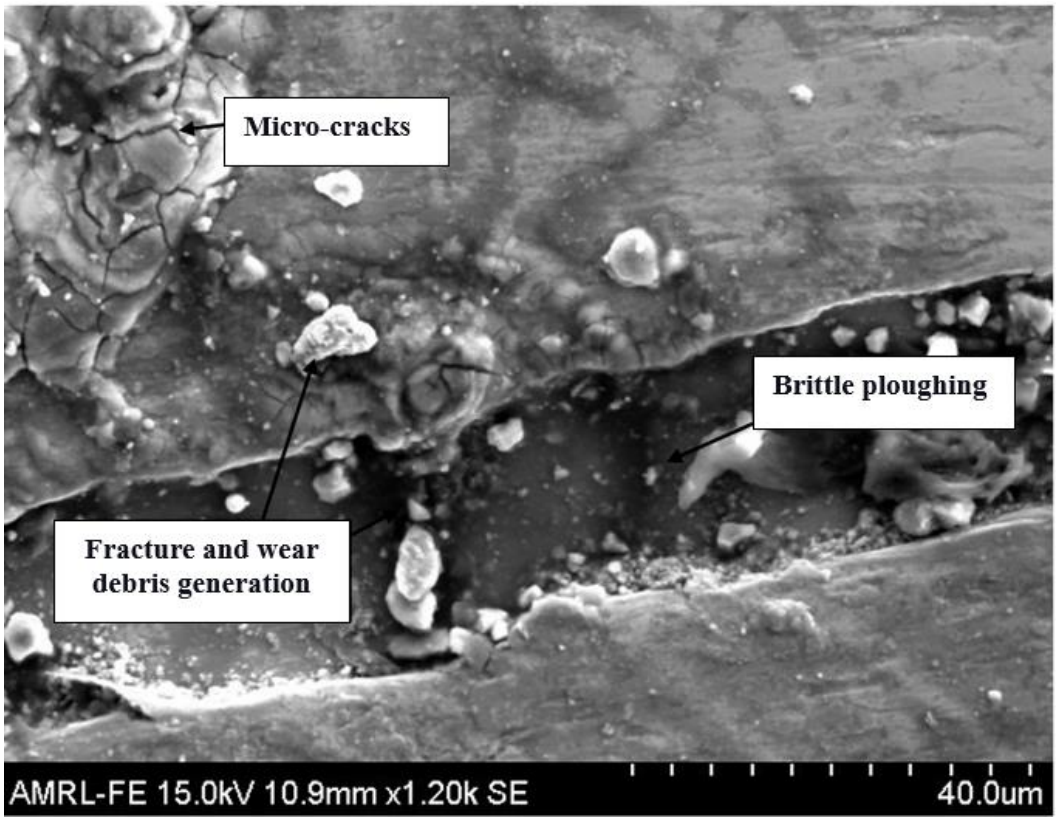

Figure 5.24 - SEM micrograph of LCS-BM disc reinforced with HF600 at 6 Kg load

5.3.7 Sliding wear performance of LCS-BM disc reinforced with SiC

5.3.7.1 Material loss

The LCS-BM+SiC composite demonstrates excellent wear resistance across all tested loads as shown in Figure 5.25. At 2 kg, the material loss is extremely low, 0.0025 g, and even as the applied load increases to 4 kg and 6 kg, the wear remains relatively stable, peaking just under ~0.005 g. Due to their high hardness, SiC particles act as barriers to plastic deformation and micro-cutting by the counter surface. Their uniform dispersion within the matrix contributed to a consistent tribological behaviour, with only minor increases in wear at higher loads.

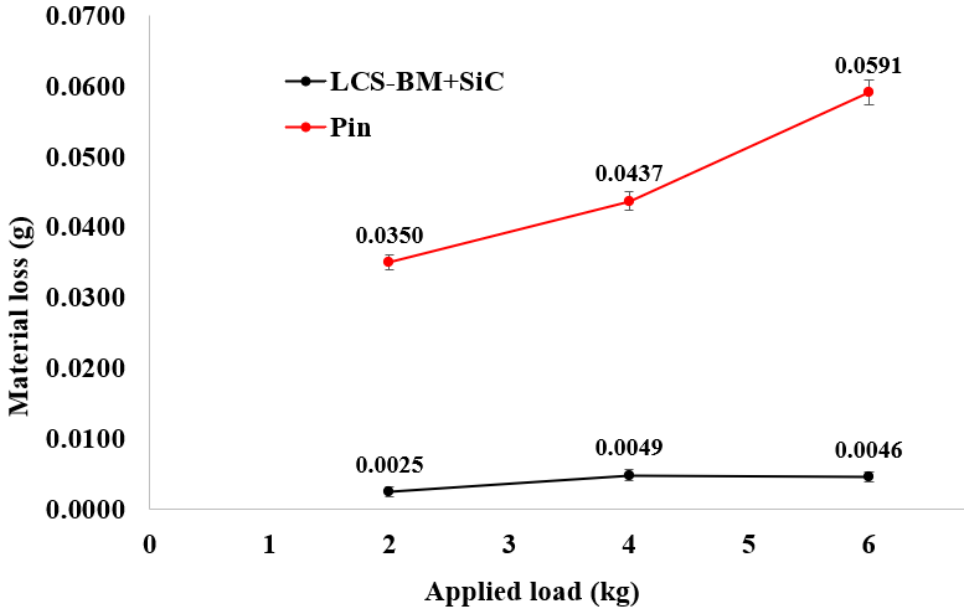

Figure 5.25 Material loss of LCS-BM disc reinforced with SiC and CI pin

5.3.7.2 Surface wear morphology at 2 Kg load

At a 2 kg load, SEM analysis in Figure 5.26 revealed a practically unaffected surface with minimal and micro-scratches with no visible surface indentation. The nominally hard surface

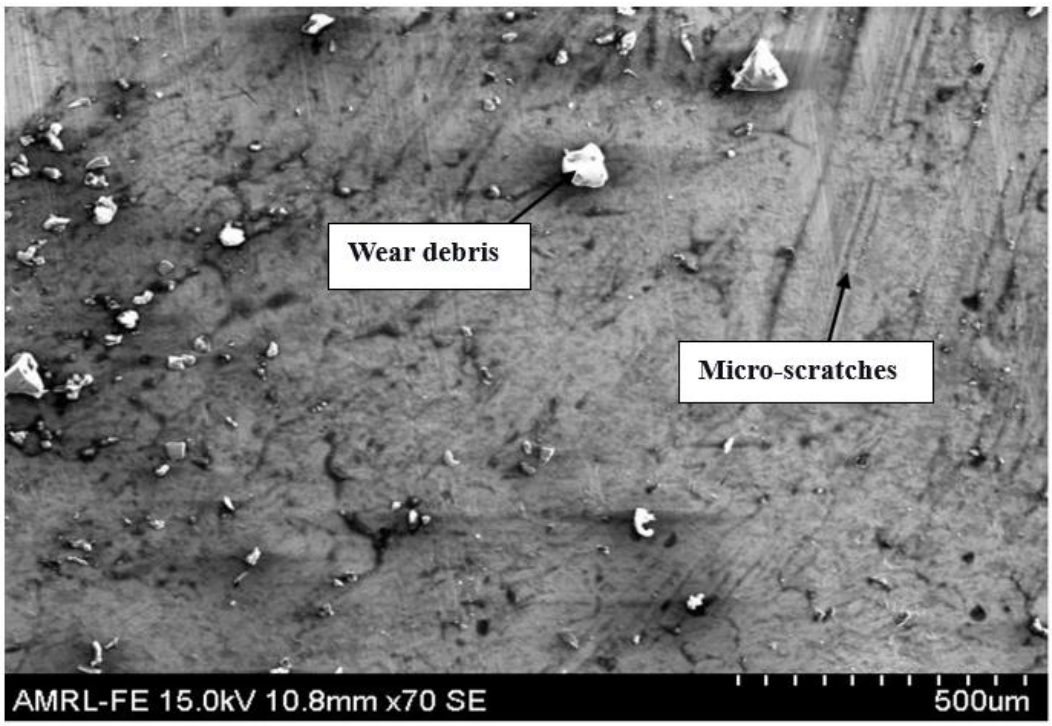

Figure 5.26 – SEM micrograph of LCS-BM disc reinforced with SiC at 2 Kg load

of the CI pin could not penetrate the deposited SiC composite, demonstrating the composite deposit's superior hardness and wear resistance. This observation is consistent with prior studies that highlighted the effectiveness of carbide-reinforced metallic matrices in resisting wear under low loads [5.22-5.25].

5.3.7.3 Surface wear morphology at 4 Kg load

At 4 kg load, Figure 2.27 showed that the surface was partially covered by a thin brown film, forming due to increased load pressure and temperature, promoting oxidation, and material detachment from the CI pin. Oxidative wear is commonly observed in metal-on-metal sliding contact under moderate loads, where temperature rise facilitates the formation of oxide films

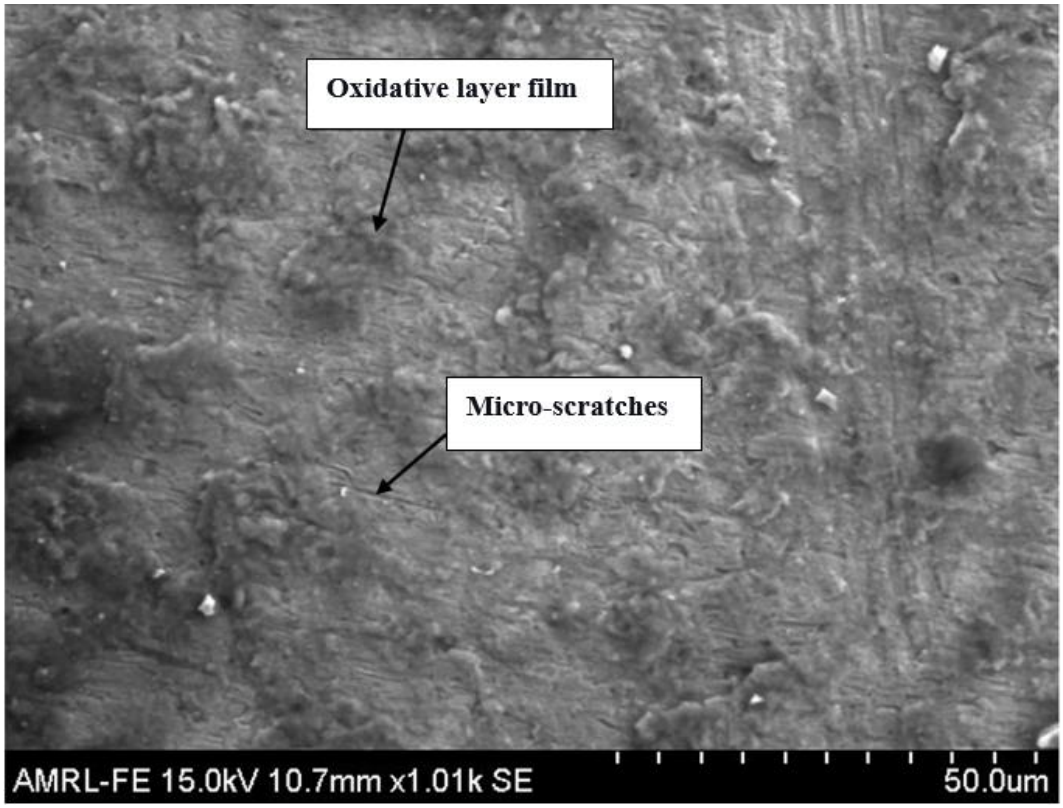

Figure 5.27 – SEM micrograph of LCS-BM disc reinforced with SiC at 4 Kg load

on interacting surfaces [5.21, 5.26-5.30]. The oxide film exhibited micro-scratches, likely caused by the detachment of SiC particles. Previous research suggests that localised particle pull-out in SiC-reinforced surfaces is common under increasing load conditions [5.31-5.34].

5.3.7.4 Surface wear morphology at 6 Kg load

At a 6 kg load as shown in Figure 5.28, the oxide layer was partially removed, exposing the underlying metallic matrix to direct contact with the CI pin. This transition marked the shift to severe wear conditions. No evidence of ductile wear mechanisms (e.g., plugging or plastic deformation) was observed. The absence of plastic deformation indicates that the SiC-infused deposit exhibited brittle fracture characteristics consistent with ceramic-reinforced microstructures. The direct contact between the underlying deposit matrix and the CI pin led to increased material removal from the pin, indicating the high wear resistance of the deposit.

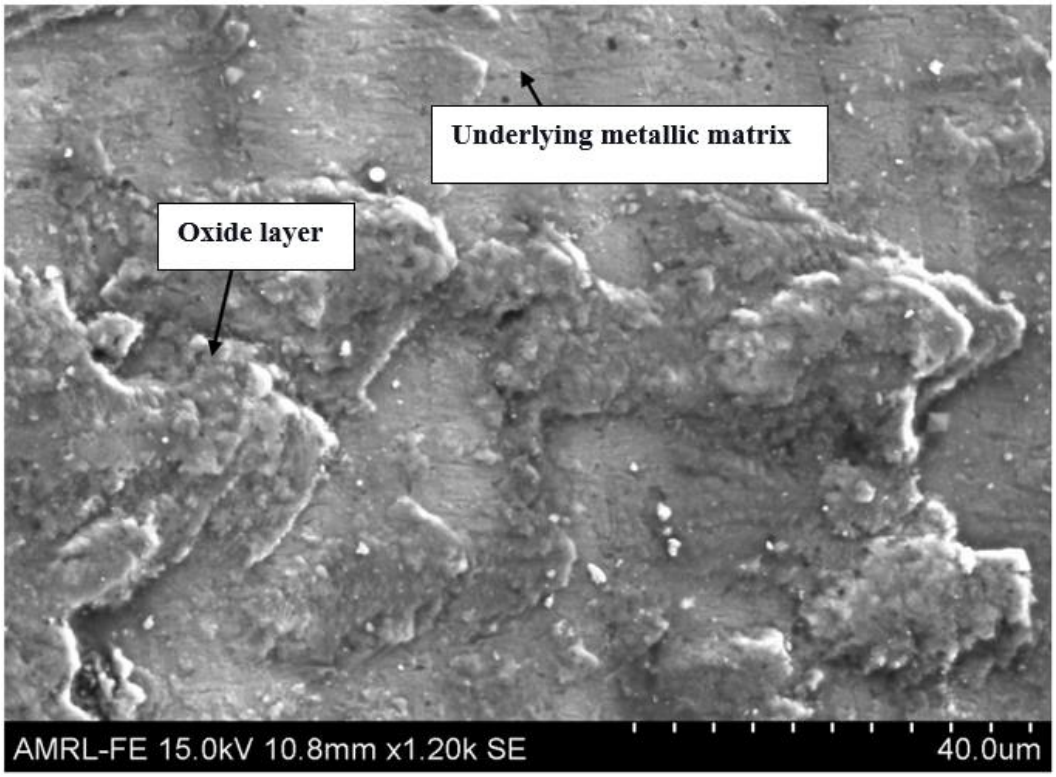

Figure 5.28. – SEM micrograph of LCS-BM disc reinforced with SiC at 6 Kg load

5.3.8 Sliding wear performance of LCS-BM disc reinforced with WC10%Co

5.3.8.1 Material loss

The LCS-BM+WC10%Co composite exhibits exceptional wear resistance across all applied loads, maintaining consistently low material loss as shown in Figure 5.29. At 2 kg, the wear is

negligible at 0.0017 g, rising slightly to 0.0066 g at 4 kg and stabilising at 0.0053 g at 6 kg. Even under increasing load, this nearly flat wear profile demonstrates the outstanding tribological performance of the WC-10%Co reinforcement within the steel matrix. The enhanced wear resistance can be attributed to the high hardness of tungsten carbide particles. The Co binder in WC-10%Co may also improve toughness and adhesion between particles and matrix.

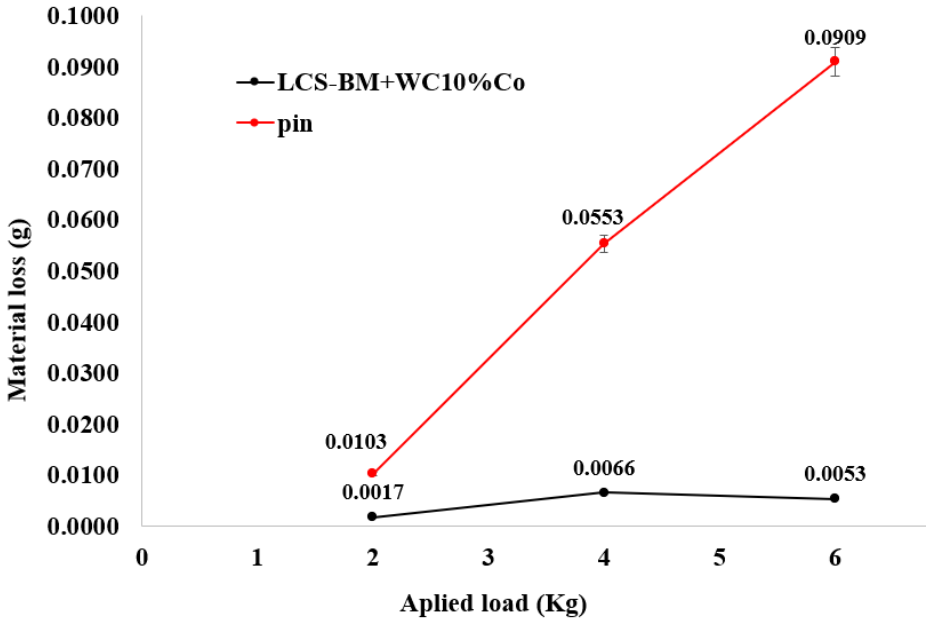

Figure 5.29 Material loss of LCS-BM disc reinforced with WC10%Co and CI pin

5.3.8.2 Surface wear morphology at a 2Kg load

Figure 5.30 represents the interface between the MMC layer and the base metal disc. The unworn surface retained its nominal circular impressions. The worn surface, which underwent sliding contact with the CI pin, displayed interaction marks, demonstrating the influence of contact pressure and friction at a 2 kg load. The worn surface showed significant flattening caused by the counter-face during sliding, yet no evidence of scratches, material deformation, or severe wear. These findings confirm that the WC-Co reinforcement effectively protected

the steel matrix from abrasion and penetration by the CI pin, ensuring excellent surface stability under low-load conditions.

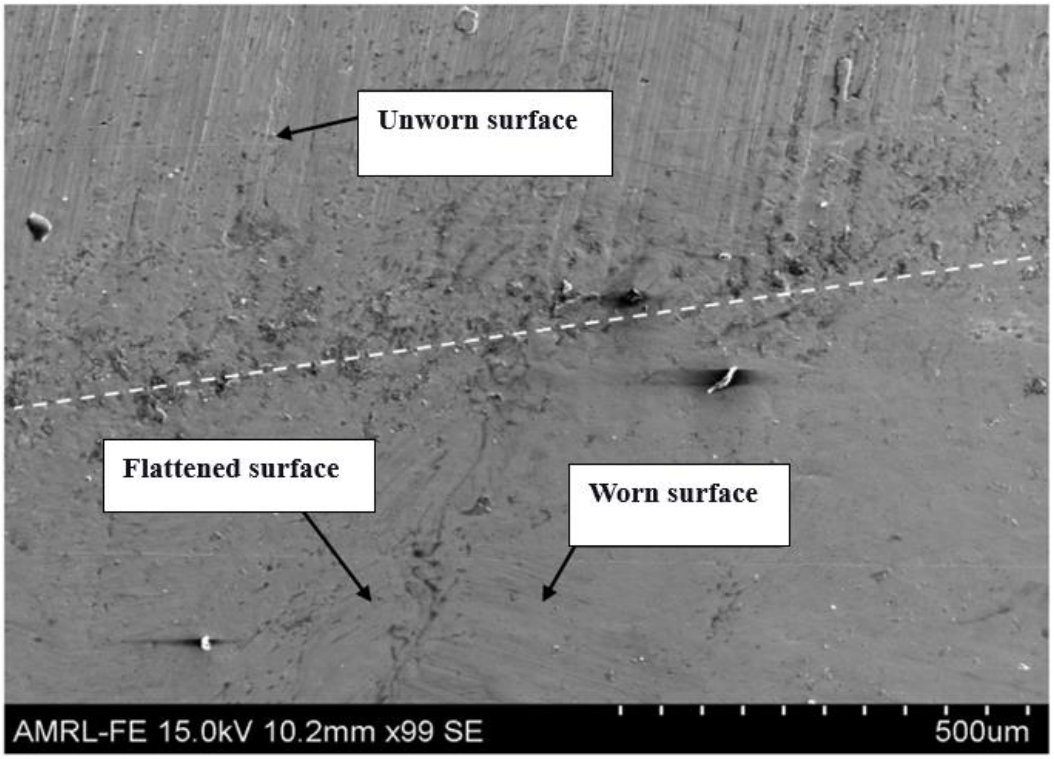

Figure 5.30 – SEM micrograph of LCS-BM disc reinforced with WC10%Co at 2 Kg load

5.3.8.3 Surface wear morphology at a 4 Kg load

Figure 5. 31 revealed the formation of a tribo-layer, commonly called the Beliy layer [5.23]. This layer likely was formed from detached material from the CI pin, which fractured into acceptable powder-like debris and was compacted onto the disc surface by frictional forces, and it can refer to as friction layer. The friction later acted as a protective shield, reducing direct contact between the CI pin and the deposited layer.

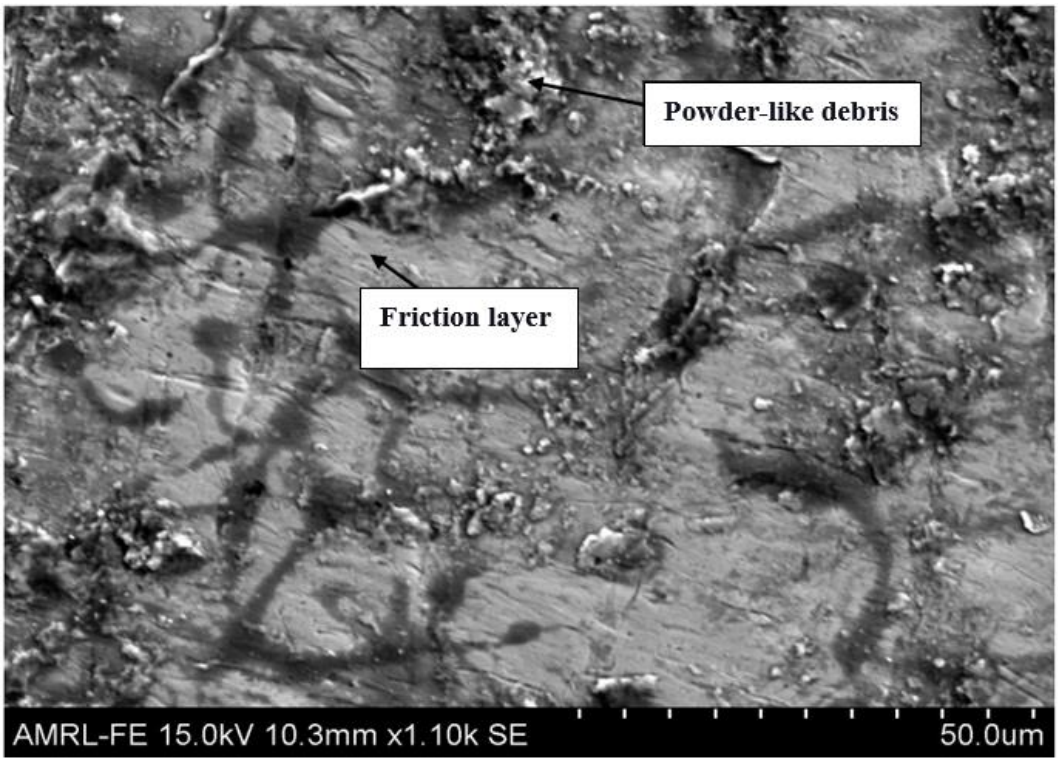

Figure 5.31- SEM micrograph of LCS-BM disc reinforced with WC10%Co at 4 Kg load

5.3.8.4 Surface wear morphology at a 6 Kg load

At 6 kg load, a specific region was selected for detailed analysis and represented in Figure 5.32. A small patch of the friction layer was removed, exposing the underlying MMC surface. This region illustrates the dynamic nature of the wear process, where the continuous formation and removal of the friction layer influences wear performance. Additionally, evidence of brittle fracture damage was observed within the friction layer. The higher applied load (6 kg) intensified material loss from the CI pin, which in turn accelerated tribo-layer formation. This led to a higher regrowth rate of the friction layer, which outpaced its removal, resulting in more extensive and protective coverage of the deposited surface. Thus, the increased load contributed to reduced material loss from the WC-Co reinforced disc, as the friction layer effectively shielded the underlying MMC surface from wear.

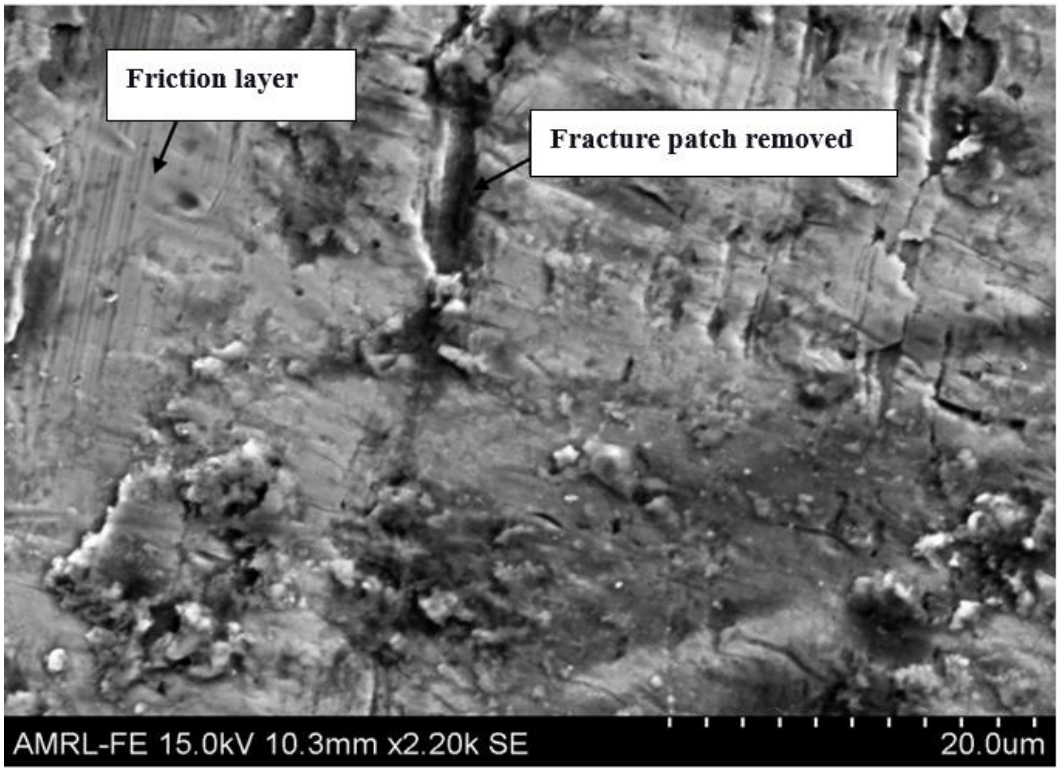

Figure 5.32 - SEM micrograph of LCS-BM disc reinforced with WC10%Co at 6 Kg load

5.3.9 Comparative assessment of material loss across all disc samples under varying loads

Comparing the performance of substrate materials with the deposit materials is essential to understanding their potential applications in tribological systems. The findings contribute to understanding the tribological benefits of advanced surface treatments and provide a benchmark for the performance of novel and commercially available solutions in reducing wear.

5.3.9.1 Material loss for all disc samples at 2 Kg load

Figure 5.33 illustrates the material loss exhibited by all disc specimens subjected to a 2 kg applied load over a continuous wear duration of three hours. Among all the tested configurations, the LCS-BM recorded the highest material loss at 0.2313 grams, highlighting its limited inherent wear resistance under low loading conditions. In contrast, applying surface reinforcements led to a remarkable reduction in wear across all samples. Incorporating

WC10%Co into the LCS matrix yielded the most significant improvement, reducing material loss to 0.0026 grams, corresponding to a 98.9% reduction relative to LCS-BM. Similarly, the SiC-reinforced LCS sample exhibited a material loss of 0.0036 grams, achieving a 98.4% reduction. The commercial HF600 hard-facing electrode also contributed to enhanced performance, albeit to a lesser extent, with a material loss of 0.0080 grams, amounting to a 96.5% reduction compared to LCS-BM.

For 316LSS-BM experienced a material loss of 0.0265 grams. The WC10%Co again demonstrated superior performance among the reinforced samples with a loss of only 0.0059 grams, representing a 77.7% reduction. The HF600-coated 316LSS sample followed, with a wear loss of 0.0090 grams (66.0% reduction). Notably, the SiC-reinforced sample recorded a material loss of 0.0285 grams, which marginally exceeded that of the 316LSS-BM. These results confirm that ceramic-filled MMCs, particularly WC10%Co, offer significant wear protection under low-load conditions, with the most pronounced enhancements observed on LCS substrates.

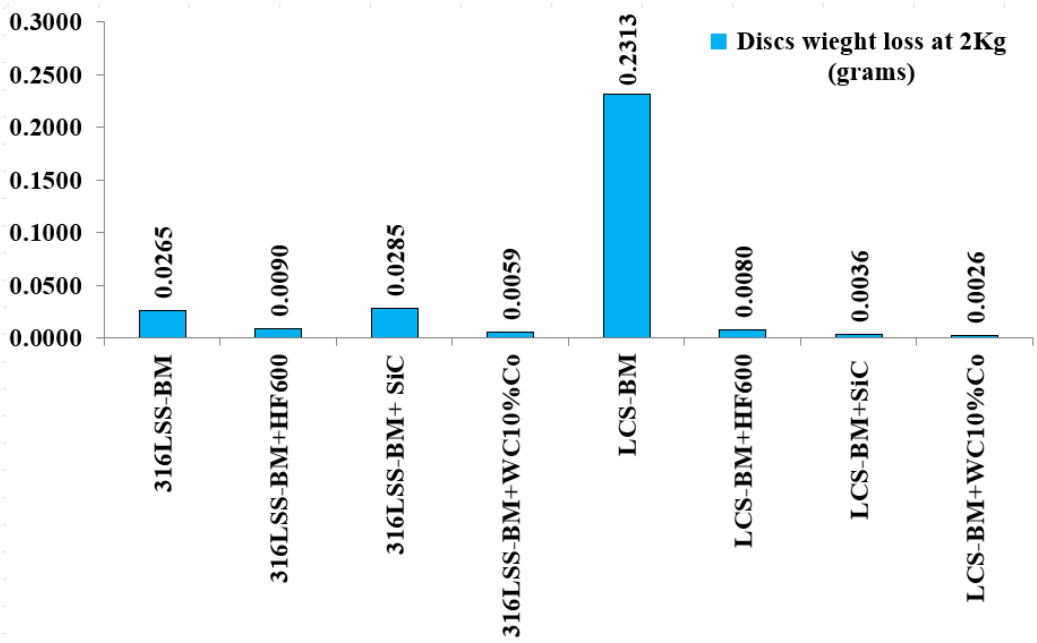

Figure 5.33 - All disc's weight loss at 2 Kg load for 3 hours

5.3.9.2 Material loss for all disc samples at 4 Kg load

Figure 5.34 presents the comparative wear performance of all disc samples subjected to a 4 kg applied load over a 3-hour wear test. As with the lower load condition, the LCS-BM exhibited the highest material loss, recording 0.0509 grams, reaffirming its susceptibility to wear under moderate loading. The application of composite deposition led to substantial improvements in wear resistance, with all reinforced samples showing markedly lower weight loss values.

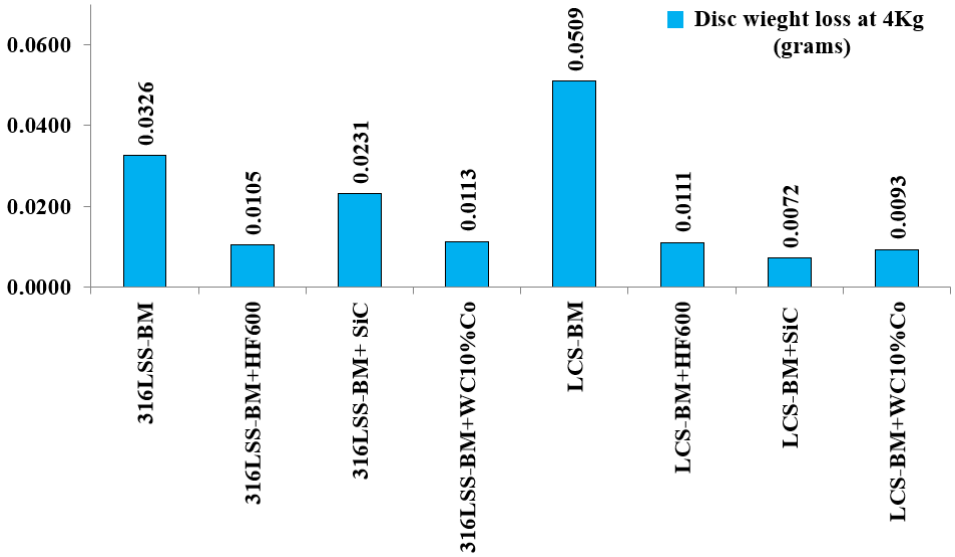

Figure 5.34. All disc's weight loss at 4 Kg load for 3 hours

Among the LCS-based samples, the Sic-reinforced sample demonstrated the most favourable performance with a material loss of 0.0072 grams, translating to an 85.9% reduction in wear relative to LCS-BM. The WC-10%Co-reinforced followed closely with a wear loss of 0.0093 grams, reflecting an 81.7% reduction. The HF600 also performed well, exhibiting a loss of 0.0111 grams, corresponding to a 78.2% improvement over the LCS-BM.

For the stainless-steel specimens, the 316LSS-BM recorded a wear loss of 0.0326 grams. Again, the most effective reinforcement in this category was WC-10%Co, reducing wear to 0.0113 grams (65.3% reduction). The HF600 coating also enhanced significantly, with a material loss of 0.0105 grams (67.8% reduction), marginally outperforming WC-10%Co in

this specific load case. The SiC-reinforced showed improved performance compared to the 316LSS-BM, with a loss of 0.0231 grams, corresponding to a 29.1% reduction.

These results reinforce the earlier trend observed under lower load: ceramic particle-reinforced MMC deposits considerably enhance the wear resistance of both LCS and stainless-steel substrates. Notably, SiC and WC-10%Co remains highly effective on LCS, while HF600 exhibits relatively stronger performance on 316LSS at this load.

5.3.9.3 Material loss for all disc samples at 6 Kg load

Figure 5.35 presents the wear performance of all disc specimens tested under an applied load of 6 kg over three hours. This high-load condition offers critical insight into the durability of each deposit's system under intensified tribological stress. The 316LSS-BM exhibited the greatest material loss at 0.0850 grams, confirming its susceptibility to adhesive and abrasive wear mechanisms in severe sliding conditions.

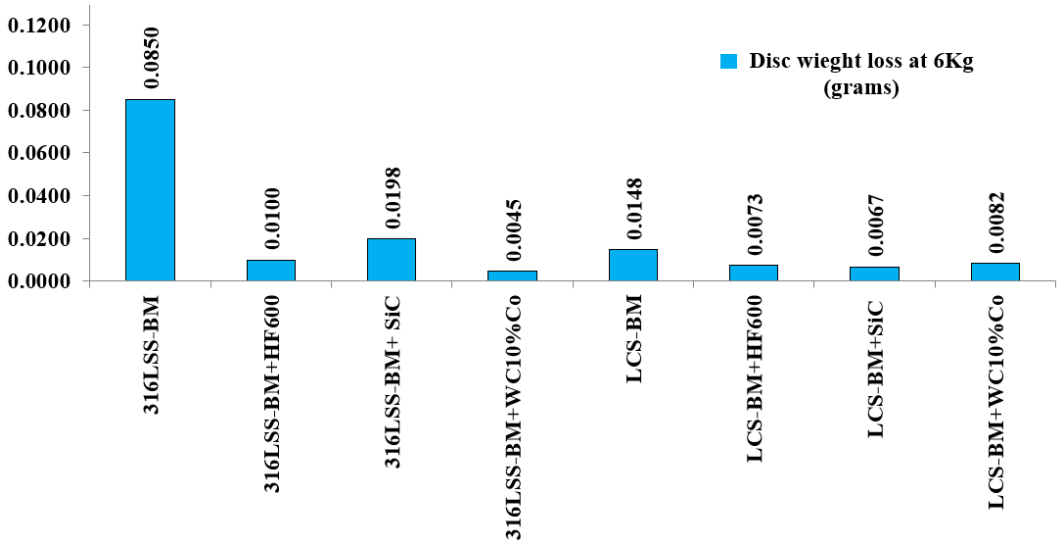

Figure 5.35. All disc's weight loss at 6 Kg load for 3 hours

Among the 316LSS-based coatings, the WC-10%Co demonstrated the most effective wear resistance, with a significantly reduced material loss of 0.0045 grams, reflecting a 94.7% reduction relative to the 316LSS-BM. The HF600 also performed well, with a loss of 0.0100

grams (88.2% reduction). In contrast, the SiC-recorded a wear loss of 0.0198 grams, corresponding to a 76.7% reduction.

For LCS substrates, the LCS-BM exhibited a material loss of 0.0148 grams. All reinforced samples surpassed this performance, but the SiC achieved the most outstanding result, with the lowest material loss across all samples at 0.0067 grams, amounting to a 54.7% reduction. The HF600 and WC-10%Co deposits followed, with wear losses of 0.0073 grams and 0.0082 grams, reflecting 50.7% and 44.6% reductions, respectively. Overall, these results highlight the exceptional wear resistance of SiC on LCS under high-load conditions, outperforming even WC-10%Co and HF600. On 316LSS substrates, however, WC-10%Co remains the superior reinforcement, suggesting that the interaction between reinforcement and matrix plays a decisive role in determining performance under severe operating conditions.

5.3.9.4 Wear performance at varying loads

5.3.9.4.1 LCS-BM comparison

Results in Table 5.1 demonstrated that all reinforced deposits substantially reduced material loss compared to the base metal, confirming their effectiveness in enhancing surface wear resistance. The SiC-reinforced composite yielded the highest average reduction of 93.5%, particularly excelling under low and medium load conditions. WC10%Co closely followed, providing consistent and balanced performance across all loads, and exhibited slightly better retention than HF600 at higher loads. Although HF600 also significantly improved wear resistance, it showed the least average reduction among the three deposit systems.

Table 5.1 Material loss and average wear reduction of deposits sample compared to LCS-BM

Sample	Material loss			Avg. Reduction vs LCS-BM (%)
	2 Kg	4 Kg	6 Kg	
LCS-BM	0.2313	0.0509	0.0148	-
+SiC	0.0025	0.0049	0.0046	93.5%
+WC10%Co	0.0017	0.0066	0.0053	92.6%
+HF600	0.0046	0.0075	0.0049	91.7%

5.3.9.4.2 316LSS-BM comparison

Results in Table 5.2 revealed that the WC-10%Co-reinforced composite provided the most effective wear resistance, achieving an average reduction of 90.9% and maintaining consistently low material loss across all loading conditions. HF600 also performed well, offering an average improvement of 86.4%, and exceeded SiC in this context. The SiC coating, while effective, displayed a comparatively lower average reduction of 69.2%, which may be attributed to less favourable bonding characteristics.

Table 5.2 Material loss and average wear reduction of deposits sample compared to 316LSS-BM

Sample	Material loss at			Avg. Reduction vs 316LSS-BM (%)
	2 Kg	4 Kg	6 Kg	
316LSS-BM	0.0265	0.0326	0.0850	-
+SiC	0.0191	0.0154	0.0132	69.2%
+WC10%Co	0.0042	0.0074	0.0031	90.9%
+HF600	0.0062	0.0071	0.0065	86.4%

5.4 Conclusions

This chapter comprehensively investigated the wear performance of 316LSS-T fillers filled with ceramic reinforcements SiC and WC-10%Co and their comparative effectiveness against HF600 hard-facing electrodes. The findings provide valuable insights into the tribological behaviour of MMC deposits and their suitability for wear resistant applications. The results demonstrated that surface modifications significantly improve wear resistance, with the effectiveness of each treatment being dependent on the base material, reinforcement type, and applied load. The 316LSS-BM and LCS-BM exhibited substantially higher material loss, confirming their susceptibility to wear under sliding conditions. SEM analysis revealed distinct differences in wear behaviour between the base metals and the surface-treated samples when sliding against a cast iron pin.

316LSS and LCS are ductile materials that undergo smearing, plastic deformation, and transfer under sliding contact. Wear features such as surface smearing, mild ploughing, and micro-plugging were observed at lower loads. As the applied load increased, these surfaces exhibited more severe wear mechanisms, including spallation, delamination, and deeper grooves, indicating increased subsurface damage. The MMC deposit significantly altered this behaviour. Hard particles such as SiC and WC10%Co effectively prevented deep penetration and plastic deformation. These reinforcements helped resist ploughing and scratching, enhancing wear resistance under moderate and high loads. Compacted friction layers were observed at higher loads, particularly in the SiC and WC-10%Co deposits. These layers are likely formed from degraded material originating from the cast iron pin. They act as protective barriers that minimise direct metal-to-metal contact and help stabilise the wear process. In contrast, HF600-treated surfaces exhibited micro-fracturing and localised delamination, contributing to slightly higher wear rates than ceramic-reinforced MMC coatings.

Strong metallurgical bonding at the deposit–substrate interface and between the ceramic particles and the surrounding steel matrix was achieved through localised melting and solidification during welding, promoting cohesive integration and contributing to the MMC deposits' enhanced wear performance. Overall, the MMC reinforcements transformed the surface response under sliding from ductile wear mechanisms to controlled, resistant behaviour, demonstrating their effectiveness.

5.5 References

[5.1] Li, Y., et al., Elimination of voids by laser remelting during laser cladding Ni based alloy on gray cast iron. Optics & Laser Technology, 2019. 112: p. 30-38.

[5.2] Wei, S. and L. Xu, Review on research progress of steel and iron wear-resistant materials. Acta Metall Sin, 2019. 56(4): p. 523-538.

[5.3] Berns, H., Comparison of wear resistant MMC and white cast iron. Wear, 2003. 254(1-2): p. 47-54.

[5.4] da Silva Simioni, G.C., et al., Engineering design process in developing a pin-on-disk apparatus to perform dry or lubricated sliding wear test. IEEE Transactions on Instrumentation and Measurement, 2023. 72: p. 1-9.

[5.5] Farias, M.C.M., et al., The influence of applied load, sliding velocity and martensitic transformation on the unlubricated sliding wear of austenitic stainless steels. Wear, 2007. 263(1-6): p. 773-781.

[5.6] Hsu, K.-L., T. Ahn, and D. Rigney, Friction, wear and microstructure of unlubricated austenitic stainless steels. Wear, 1980. 60(1): p. 13-37.

[5.7] Schneider, C., et al., Optimizing the Parameters of TIG-MIG/MAG Hybrid Welding on the Geometry of Bead Welding Using the Taguchi Method. Journal of Manufacturing and Materials Processing, 2017. 1(2).

[5.8] Straffelini, G., A. Molinari, and D. Trabucco, Sliding wear of austenitic and austenitic-ferritic stainless steels. Metallurgical and Materials Transactions A, 2002. 33: p. 613-624.

[5.9] Alemani, M., et al., Dry sliding of a low steel friction material against cast iron at different loads: Characterization of the friction layer and wear debris. Wear, 2017. 376-377: p. 1450-1459.

[5.10] Bolelli, G., L. Lusvarghi, and M. Barletta, HVOF-sprayed WC–CoCr coatings on Al alloy: effect of the coating thickness on the tribological properties. Wear, 2009. 267(5-8): p. 944-953.

[5.11] Islam, M.A., et al., Effect of microstructure on the erosion behavior of carbon steel. Wear, 2015. 332: p. 1080-1089.

[5.12] Rainforth, W., Microstructural evolution at the worn surface: a comparison of metals and ceramics. Wear, 2000. 245(1-2): p. 162-177.

[5.13] Scherge, M., D. Shakhvorostov, and K. Pöhlmann, Fundamental wear mechanism of metals. Wear, 2003. 255(1-6): p. 395-400.

[5.14] So, H., H.M. Chen, and L.W. Chen, Extrusion wear and transition of wear mechanisms of steel. Wear, 2008. 265(7-8): p. 1142-1148.

[5.15] Eyre, T.S., Wear Mechanisms. Powder Metallurgy, 2013. 24(2): p. 57-63.

[5.16] Weng, Z., et al., Wear resistance of diode laser-clad Ni/WC composite coatings at different temperatures. Surface and Coatings Technology, 2016. 304: p. 283-292.

[5.17] Yang, Z., M. Naylor, and D. Rigney, Sliding wear of 304 and 310 stainless steels. Wear, 1985. 105(1): p. 73-86.

[5.18] Smith, A., The friction and sliding wear of unlubricated 316 stainless steel at room temperature in air. Wear, 1984. 96(3): p. 301-318.

[5.19] Garbar, I. and J. Skorinin, Metal surface layer structure formation under sliding friction. Wear, 1978. 51(2): p. 327-336.

[5.20] Kumar, S., et al., Dry sliding wear behaviour of medium carbon steel against an alumina disk. Wear, 2011. 270(5-6): p. 413-421.

[5.21] Woodward, R.G., A. Toumpis, and A. Galloway, The influence of tempering and annealing on the microstructure and sliding wear response of G350 grey cast iron. Wear, 2022. 496-497.

[5.22] Dutta Majumdar, J., A. Kumar, and L. Li, Direct laser cladding of SiC dispersed AISI 316L stainless steel. Tribology International, 2009. 42(5): p. 750-753.

[5.23] Dutta Majumdar, J., et al., Studies on compositionally graded silicon carbide dispersed composite surface on mild steel developed by laser surface cladding. Journal of Materials Processing Technology, 2008. 203(1-3): p. 505-512.

[5.24] Majumdar, J.D., Development of in-situ composite surface on mild steel by laser surface alloying with silicon and its remelting. Surface and Coatings Technology, 2010. 205(7): p. 1820-1825.

[5.25] Majumdar, J.D., et al., Laser composite surfacing of stainless steel with SiC. physica status solidi (a), 2006. 203(9): p. 2260-2265.

[5.26] Stott, F., J. Glascott, and G. Wood, Factors affecting the progressive development of wear-protective oxides on iron-base alloys during sliding at elevated temperatures. Wear, 1984. 97(1): p. 93-106.

[5.27] Wilson, J., F. Stott, and G.C. Wood, The development of wear-protective oxides and their influence on sliding friction. Proceedings of the Royal Society of London. A. Mathematical and Physical Sciences, 1980. 369(1739): p. 557-574.

[5.28] Woodward, R.G., A. Toumpis, and A. Galloway, The influence of cementite spheroidizing duration on the microstructure and sliding wear response of grey cast iron against AISI 4330. Wear, 2022. 488-489.

[5.29] Woodward, R.G., et al., The Influence of Load on Dry and Tribocorrosive Sliding of AISI 4330 and 15-5PH against Cast Iron. Tribology Transactions, 2021. 64(5): p. 956-967.

[5.30] Guo, Q., et al., Effect of passive film on mechanical properties of martensitic stainless steel 15-5PH in a neutral NaCl solution. Applied Surface Science, 2015. 327: p. 313-320.

[5.31] Azwan, M., M.A. Maleque, and M.M. Rahman, TIG torch surfacing of metallic materials – a critical review. Transactions of the IMF, 2018. 97(1): p. 12-21.

[5.32] Lailatul, P. and M. Abd Maleque, Tribological properties of surface coated duplex stainless steel containing SiC ceramic particles. Jurnal Tribologi, 2018. 18: p. 136-148.

[5.33] Maleque, M., et al. Optimization of tribological performance of SiC embedded composite coating via Taguchi analysis approach. in IOP Conference Series: Materials Science and Engineering. 2017. IOP Publishing.

[5.34] Paijan, L.H., et al., Influence of ceramic particles size on the incorporation of SiC into stainless steel material using 480 J/mm heat input for tribological applications. Jurnal Tribologi, 2023. 37: p. 14-27.

Chapter 6 Conclusions and future work

6.1 Conclusions

This research successfully developed and demonstrated a novel deposition strategy for MMCs using ceramic-filled tubular filler rods in the TIG welding process. The approach involved designing and fabricating tubular filler electrodes pre-packed with reinforcement particles such as SiC and WC-10%Co, enabling controlled, in-situ delivery of ceramics into the molten pool. This method offers a scalable and cost-effective alternative to traditional MMC fabrication routes, addressing long-standing challenges related to ceramic dispersion, retention, and bonding within metallic matrices. The findings establish this technique as a promising surface engineering solution for enhancing wear resistance in steels, especially under severe operating conditions.

This thesis comprehensively investigates the wear performance of metal matrix composite (MMC) surface deposits fabricated using (316LSS) tubular fillers infused with ceramic reinforcements silicon carbide (SiC) and tungsten carbide with 10% cobalt (WC-10%Co). The study evaluates the effectiveness of these novel surface treatments in enhancing wear resistance, benchmarking their performance against conventional HF600 commercial hard-facing electrodes on low-carbon steel and stainless-steel substrates. The research successfully integrates welding process optimisation, microstructural characterisation, and tribological analysis to establish a reliable, performance framework for developing high efficiency wear resistant coatings.

A systematic approach was employed to optimise the TIG welding parameters, ensuring uniform deposition, minimal porosity, strong metallurgical bonding, and reduced dissolution of ceramic reinforcements. An optimised tubular filler geometry (4 mm outer diameter, 3 mm inner diameter, 1 mm wall thickness) was selected through iterative experimental refinement. This configuration facilitated the effective embedding of ceramic particles within steel matrix,

maintaining their structural integrity and wear-resistant functionality. The reinforced deposits were evaluated through dry sliding pin-on-disc wear tests under increasing loads (2 kg, 4 kg, and 6 kg). Detailed microstructural and surface analyses using scanning electron microscopy (SEM) and energy-dispersive spectroscopy (EDS) revealed distinct wear mechanisms, material degradation pathways, and tribo-layer formations across different surface treatments and base metals.

Quantitatively, the reinforced MMC coatings demonstrated a 4-to-6-fold reduction in material loss compared to untreated base metals, indicating significant improvements in wear resistance. Among the tested systems, (WC-10%Co) reinforced coatings exhibited the lowest wear rates and highest surface stability, particularly on stainless steel substrates. (SiC) reinforced deposits were the most effective on low-carbon steel, forming protective tribo-layers that minimised oxidation and abrasive wear. The study identified the dominant wear mechanisms for each sample condition:

- Untreated stainless steel (316LSS-BM) showed severe plastic deformation, adhesion, and brittle fracture under high loads.
- Untreated low-carbon steel (LCSB-M) suffered from continuous abrasive wear and oxidation.
- HF600 coatings improved wear resistance but exhibited brittle fracture and delamination at elevated loads due to their martensitic structure.
- SiC-reinforced 316LSS deposits developed oxidised tribo-layers that enhanced wear resistance but were prone to localised carbide pull-out.
- WC-10%Co-reinforced 316LSS deposits delivered the best overall performance, with high hardness preventing ploughing and a cobalt binder improving fracture toughness and oxidation resistance.

- SiC-reinforced LCS delayed wear progression through tribo-layer formation, though brittle fracture was noted under maximum loading.
- WC-10%Co-reinforced LCS effectively reduced plastic deformation and stabilised wear progression by forming a protective friction layer.

Mechanistically, the embedded ceramic particles played a dual role in delaying the transition from mild to severe wear regimes. Their high hardness acted as a barrier to abrasive ploughing and plastic deformation, protecting the matrix, while the surrounding ductile steel matrix absorbed stresses and shielded the hard particles from cracking and dislodgement. This mutual reinforcement resulted in a stable surface structure under load, mitigating adhesion, abrasive damage, and third-body wear.

This thesis confirms that ceramic-reinforced MMC coatings fabricated using custom-designed tubular fillers represent a robust and versatile surface engineering solution for wear-critical applications. The research establishes clear superiority over conventional hard-facing electrodes in performance and durability. It also bridges the critical gap between process optimisation and material performance, offering a comprehensive, scalable, and industrially relevant approach for next-generation wear-resistant coatings.

6.2 Future Work

Building upon the findings of this study, several avenues for future research are proposed:

- Advanced Characterisation: Incorporating transmission electron microscopy (TEM), X-ray diffraction (XRD), and nanoindentation could provide deeper insight into phase transformations, interfacial bonding, and localised hardness variations within the MMC deposits.
- Thermal and Fatigue Performance: Investigating the thermal stability and fatigue resistance of the ceramic-reinforced deposit under cyclic loading and elevated

temperatures would enhance their suitability for real-world applications in high-stress environments.

- Alternative Ceramic Reinforcements: Future work could explore other reinforcements such as TiC, or nano-scale ceramics, individually or in hybrid combinations, to further tailor the microstructure and wear resistance of the deposited layers.
- Process Scalability and Automation: Developing automated TIG deposition systems and evaluating the scalability of the tubular filler method for more significant components and industrial applications would bridge the gap between laboratory research and manufacturing deployment.
- Corrosion-Wear Synergy Studies: Since many service environments involve mechanical wear and corrosive exposure, assessing the MMC coatings' combined corrosion-wear resistance would provide more holistic performance data.
- Numerical Modelling and Simulation: Incorporating finite element modelling (FEM) to simulate heat transfer, stress distribution, and wear evolution during deposition and service could support predictive optimisation of process parameters and coating design.

The proposed ceramic-filled tubular filler technique can be further refined, validated, and transitioned into industrially viable solutions for wear-critical applications by pursuing these directions.